Lateral spin injection and detection via electrodeposited Fe/GaAs contacts

by

Sarmita Majumder

M.Tech. (Cryogenics), Indian Institute of Technology (I.I.T. Kharagpur), 1999
M.Sc. (Physics), Kalyani University, 1994
B.Sc., Vidyasagar University, 1990

Thesis Submitted in Partial Fulfillment
of the Requirements for the Degree of
Doctor of Philosophy

In The
DEPARTMENT OF PHYSICS
FACULTY OF SCIENCE

SIMON FRASER UNIVERSITY

Fall 2013

Approval

Name: Sarmita Majumder

Degree: Doctor of Philosophy (Physics)

Title of Thesis: Lateral spin injection and detection via electrodeposited Fe/GaAs contacts

Examining Committee:

Chair: J. Steven Dodge
Associate Professor, Department of Physics

Karen L. Kavanagh
Senior Supervisor
Professor, Department of Physics

George Kirczenow
Supervisor
Professor, Department of Physics

Patricia M. Mooney
Supervisor
Professor, Department of Physics

Mike Thewalt
Internal Examiner
Professor, Department of Physics

Berend T. Jonker
External Examiner
Senior Scientist, Naval Research Laboratory

Date Defended: September 6, 2013

Partial Copyright License

Abstract

Experimental studies of lateral spin injection and detection through electrodeposited Fe/GaAs tunnel contacts are reported in this thesis. An enhanced spin valve voltage is demonstrated via non-local lateral spin transport measurements compared to their vacuum-deposited counterparts. We have proposed a simple theoretical model to explain this result. Combined with experimental evidence for interfacial oxygen from atom probe tomography, we speculate that the enhancements occur due to a magnetic iron oxide layer forming at the Fe/GaAs interface during the electrodeposition. This layer acts as a tunnel barrier with a spin-dependent height. This discovery of greatly enhanced spin injection into GaAs via electrodeposited contacts introduces a promising new direction for the development of practical semiconductor spintronic devices.

This thesis addresses three major challenges: i) The electrodeposition of Fe onto an epitaxial *n*-GaAs layer on a semi-insulating substrate to fabricate the tunnel contacts and lower-doped channel required for lateral spin injection. ii) Demonstration of spin accumulation and transport using patterned contacts in lateral configurations. iii) Understanding magnetic in-homogeneities and defects in the thin Fe film and correlating these to the observed enhanced spin injection.

Continuous Fe film coverage was achieved over a desired area of the epitaxial GaAs by creating a uniform potential at the back of the sample. Nucleation and growth of Fe was observed within a range of applied current densities from 0.05 to 0.20 mA/mm^2, with the best Fe epitaxy occurring at 0.15 mA/mm^2. Modelling via a micromagnetic simulator showed that magnetic hysteresis curves from the electrodeposited Fe did not follow the standard behavior of a thin Fe film (single or polycrystalline). Instead, these Fe films demonstrated inhomogeneous magnetization controlled by strong local uniaxial anisotropies along both the ⟨100⟩ and ⟨110⟩ crystallographic directions. The presence of defects and coalescence boundaries responsible for these in-homogeneities were detected by transmission electron microscopy. Spin valve and Hanle measurements showed evidence of a local magnetostatic field, possibly originating from magnetic impurities at the electrodeposited Fe/epitaxial GaAs interface. We suggest that these magnetic impurities enhanced the

tunneling probability and the spin accumulation within the GaAs channel while reducing the spin lifetime.

Keywords: spintronics, GaAs, Fe, electrodeposition, magnetic interfacial layer

Dedicated to my husband and my son

Acknowledgements

I would like to express my heartiest gratitude and respect for my supervisor Dr. Karen Kavanagh for her invaluable guidance towards my thesis work. She helped me in all aspects of my life during these years. She was always with me whenever I needed her. I could not have finished my degree without her help.

Dr. Anthony Arrott and Dr. Bret Heinrich taught me to learn all about the magnetic properties of my sample. They helped me to understand the theory as well as the measurements. Dr. Anthony Arrott also contributed the micromagnetic simulation for my experimental results of the hysteresis loops.

My sincere gratitude goes to Dr. George Kirczenow. He taught me the basic concepts of the spin transport. He also contributed quantum modelling of the spin transport to explain my results on NLSV measurements.

Dr. Simon Watkins taught me how to use a cryostat at liquid He temperature. I would like to thank him for letting me use the He cryostat and the Hall probe system for spin measurements in his lab.

I would like to thank Dr. Patricia Mooney for helping me learn HRXRD techniques and concepts.

I would like to thank all of my colleagues and lab mates, and staff in our Physics Department and 4-D lab for their cooperation during my thesis work. Special thanks go to Bryan Gormann for making the sample holder for my spin measurements. Also I should mention Donna Hohertz, James McNeil and Eric Montoya for their valuable contributions towards proof reading and suggestions. Donna also constructed a special holder for extra permanent magnets required during spin measurements. I would like to thank Dr. Bartek Kardasz for helping me with the FMR and MOKE measurements.

I would like to express my heartiest gratitude to my husband and my son for their contribution throughout my thesis work and writing and moral support. I would not have

completed my thesis work without their help. My husband took care of everything that I needed including cooking and taking care of our son and picking me up in the late at the night from SFU. He also gave me some invaluable suggestions during thesis work especially for fabrication and spin measurements. And my son helped me to organize the thesis. I am grateful to him for not asking me for extra time for his school work or anything else. I want to thank my parents, my sister, mother in-law and sister in-law for their moral support all along.

Table of Contents

List of Tables

List of Figures

List of Symbols

Ω	Tilt between the substrate and the film
ψ	Tilt in the *hkl* plane with respect to the substrate
δ	Phase angle
φ_0	Magnetic flux
μ	Micron
h	Planck's constant
M	Magnetic moment
ε_r	Relative dielectric permittivity
ε_o	Permittivity in the vacuum
θ_B	Bragg angle
χ	Azimuthal angle
φ	In-plane rotational angle
λ	Wavelength
γ	Poisson ratio
L	Grain size
D	Ion diffusion coefficient
D_w	Density of the material
E_C	Conduction band energy
E_F	Fermi energy
$\varepsilon_{//}$	In-plane X-ray strain
$\varepsilon_{\perp}$	Out-of-plane X-ray strain
$a_{//}$	In-plane lattice constant
$a_{\perp}$	Out-of-plane lattice constant
a_f	Relaxed film lattice constant
A^{**}	Richardson constant
F	Faraday constant
z	Ionic charge
Å	Angstrom
J	Current density
I	Current
V	Voltage
T	Temperature
n	10^{16} cm^{-3} doped
n^+	10^{18} cm^{-3} doped or higher
N_A	Avogadro's no
M_W	Molecular weight
φ_B	Barrier height

φ_m Work function of the metal
W_D Depletion width
A_C Contact area
R_C Contact resistance

List of Acronyms or Glossary

APT	Atom Probe Tomography
BF	Bright Field
DF	Dark Field
DIP	Dual in Package
ED	Electrodeposited
EDS	Energy Dispersive X-Ray Spectra
epi	Epitaxial
FIB	Focussed Ion Beam
FM	Ferromagnet
FMR	Ferromagnetic Resonance
FEG	Field Emission Gun
FWHM	full Width Half Maxima
GPIB	General Purpose Interface Bus
LL	Landau Lifshitz
LN	Liquid Nitrogen
LSV	Local Spin Valve
MBE	Molecular Beam Epitaxy
MOCVD	Metal Organic Chemical Vapour Deposition
MR	Magneto Resistance
NLSV	Non-Local Spin Valve
PID	Proportional Integral Derivative
QW	Quantum Well
RT	Room Temperature
RA	Resistance Area
RSM	Reciprocal Space Map
SQUID	Superconducting Quantum Interference Device
SEM	Scanning Electron Microscopy
SAD	Selected Area Diffraction
SM	Semiconductor
S.I.	Semi Insulating
TEM	Transmission Electron Microscopy
XTEM	Cross-section TEM
UHV	Ultra High Vacuum
XRD	X-ray Diffraction
HRXRD	High Resolution X-ray Diffraction

1. Introduction

Achieving efficient spin transport into and through a semiconductor or metal channel is one of the key objectives of the field of spintronics. Semiconductors have many advantages over metals including much longer spin lifetimes and spin diffusion lengths [1]. The spin field-effect transistor, first proposed by Datta and Das [2], exploits this idea and has been pursued by many other researchers [3-17]. One of the first challenges was to produce efficient methods of spin injection and detection.

The interface resistance of the ferromagnetic/semiconductor (FM/SM) contact was found to be the crucial parameter for efficient spin injection [18, 19]. A Schottky barrier provided by a magnetic metal contact to the thin depletion region of a heavily doped n^+-semiconductor surface resulted in the desired contact resistance [4-6, 20]. Such magnetic metals including Fe, Fe-Ni, Co and Fe-Co have demonstrated efficient spin injection and detection into GaAs, Si and Ge [10-16]. In most cases, molecular beam epitaxy (MBE) was used to grow both the semiconductor and the metal film, at room or near room temperature, in ultra-high-vacuum (UHV) [10-12, 14-16].

In the case of GaAs in particular, the MBE FM films were typically ultrathin (5 nm -10 nm) grown onto optimized epitaxially grown (epi) doped-GaAs tunnel structures [10-12, 14]. Annealing was found to increase the spin polarization which was correlated with interfacial reactions of the FM and SM [21, 22]. The lattice mismatch between Fe (bcc) and GaAs (Zincblend) is 1.4%, assuming 2 Fe unit cells per unit cell of GaAs. Therefore epitaxial growth has been feasible and the orientation of Fe was determined by the substrate orientation. But it was unknown whether the crystallinity of the Fe was important to spin injection. The design of the GaAs tunnel barrier structure was found to be very important for efficient injection since too low or too high a contact resistance reduced the resulting spin transport [20].

There exist two major spin-transport test mechanisms, “vertical” based on optical emission, and “lateral” based on spin valve theory. Spin light-emitting diodes measure

spin transport in the vertical direction and consist of a surface FM metal-semiconductor spin injector with a buried quantum well (QW). Injected spin-polarized electrons reaching the QW recombine with un-polarized holes. The resulting polarized light emission is proportional to the degree of electron spin polarization [3-6]. In lateral spin transport measurements, polarized electrons are injected and detected through at least two FM metal contacts (Fe, FeCo, Ni, or Co) [10-16] or magnetic semiconductor hetero-structures [16], positioned laterally across the semiconductor substrate. The degree of spin polarization is detected in the simplest case as the change in voltage that develops as a function of the magnetic alignment of the two contacts. Spin accumulation at individual FM contacts is also commonly detected using techniques based on the Hanle effect where the magnetic field is applied perpendicular to the spin alignment.

The electrodeposition process developed by Bob Bao [23] is simpler and less expensive than UHV methods for the preparation of epitaxial metal layers on GaAs, including Fe, NiFe, Co, Bi, and Cu. In particular, Bob's work demonstrated that the electrodeposited (ED) Fe contacts on bulk GaAs substrate displayed comparable electrical barrier heights to those reported using MBE. Since the growth rates were much higher, at least a 100 times greater, there was a larger island nucleation and coalescence process that resulted in thicker continuous films. Nevertheless, growth was epitaxial and structural analysis showed a quasi-single-crystalline microstructure with low angle grain boundaries and little residual stress [24].

Meanwhile, several groups had grown FM films on semiconductor substrates using UHV growth methods for FM/SM spin contacts [10-16]. These groups showed successful spin transport at low temperatures via optical and lateral electrical spin transport measurements. The first optical spin transport measurements for Fe/GaAs showed 2% spin injection efficiency at room temperature [3]. More recently, many groups have reported higher spin injection efficiencies up to 32% and also showed that post growth annealing enhanced this further to up to 50%. They speculated that this increased spin accumulation was due to interfacial states and/or from reactions between Fe and GaAs [21, 22, 25]. Meanwhile, lateral spin measurements between MBE Fe/GaAs tunnel contacts report spin voltages, ΔV, of 12 to 16.8 ± 0.2 μV at temperatures of 10 to 50 K with an applied bias of 1 mA [11, 12, 15]. The spin life times (τ_s) ranged between 4 ns and 24 ns for temperatures of 70 K to 10 K [11], values that were smaller

than expected. For a 10^{16} cm^{-3} doped GaAs channel previous measurements via optical spin pumping reported values from 7 ns to 80 ns for the same temperature range [26, 27]. These groups also reported changes in spin polarization due to the coupling of the applied magnetic field and nuclear hyperfine interactions. A higher spin voltage signal by a factor of 40 has been reported for Co-Fe /GaAs when a thin MgO insulating oxide layer was present between the FM and SM lateral non-local spin contacts [28].

Other techniques, besides MBE, included sputter-deposited $Co_{50}Fe_{50}$/GaAs) [14] contacts, where a spin voltage signal as large as 1 μV was reported for an applied bias of 30 μA, detectable up to 290 K. The bias dependence of the spin signal, similar to observations on MBE grown contacts, was proposed to be possibly due to localized states in the semiconductor arising from inhomogeneous doping [11]. There is also one example of ED Ni/GaAs (110) measured at 10 K that showed a magneto-resistance (MR) of 0.3 % but no spin diffusion times were reported [29].

Many groups have experimented with using FM/oxide/SM, for example, Fe, Co, Fe-Co and Ni-Fe/MgO, SiO_2 and Al_2O_3/Si, GaAs and Ge tunnel contacts. They have also observed enhanced spin accumulation in the semiconductor underneath individual FM contacts [30-35]. The resistance-area product (*RA*) extracted from Hanle measurements ranged from 1500 kΩ μm^2 to 6 kΩ μm^2, two or three orders of magnitude larger compared to their corresponding theoretically predicted values. Trans *et.al*. has invoked an idea of spin accumulation in the interfacial defect states with long spin life time at the interface [32]. Broadening of the Hanle signal due to surface roughness of the ferromagnetic contact was also thought to occur [33, 35].

Since we could obtain apparently similar interfaces at comparable growth temperatures to those used by UHV methods, we proposed to demonstrate spin transport using our electrochemically grown Fe/GaAs. Optical measurements require ultra-thin Fe films (5 nm) if the light detected must exit through the surface contacts. ED of continuous Fe films less than 50 nm has not been observed by our group despite many experiments in which the applied current and electrolyte concentration were varied. Therefore, we decided to pursue electrical lateral spin measurements with thicker continuous films. We chose to work on Fe since it is a very good FM metal

having a spin magnetic moment of 2.22 μ_B, higher than bcc Co 1.59 μ_B or fcc Ni 0.6 μ_B [36].

We knew that there are many differences between ED and MBE Fe/GaAs contacts. First, as mentioned, continuous Fe films made by ED are 100 nm to 150 nm thick, much thicker than MBE grown ultrathin Fe films of 5 nm, and only quasi-single crystalline. Therefore, the magnetic properties would likely have a greater degree of complexity compared to MBE Fe films. Also, magnetic in-plane uniaxial anisotropies for ultrathin Fe films, which originate from symmetry breaking at the interface due to the substrate's surface reconstruction, are missing in the case of ED Fe films [37, 38]. Compared to their MBE counterparts ED Fe film were completely strain relaxed.

1.1. Interesting Questions

There were many basic questions regarding spin transport and its relation to the magnetic behavior of Fe/GaAs contacts that are still relevant. For example: Is uniaxial anisotropy in the FM film really necessary for magnetic switching of the contacts? Do domain boundaries influence spin transport at the interface at the spin injection point? How do magnetic impurities influence spin transport? Does the strain in the FM film affect spin transport? Is the thickness of the FM film important? Do the inherent magnetic impurities in the ED Fe film influence spin transport? In this thesis, lateral spin transport from strain-relaxed ED Fe/GaAs contacts will be shown.

1.2. Summary of the research

This thesis investigates the ED of Fe on epi-GaAs samples and the correlation of structural and magnetic properties with the spin transport through these interfaces. A major accomplishment was the ED of Fe films on GaAs epilayers grown on semi-insulating GaAs substrates. Using patterned Fe contact structures, larger lateral spin valve voltages than for MBE-grown Fe/GaAs [11] have been shown. It is proposed that this enhancement may be due to a magnetic iron oxide layer, which forms at the Fe/GaAs interface during ED, acting as a tunnel barrier with a spin-dependent height.

To support this speculation a simple qualitative model using quantum spin transport calculations is presented for such systems [39]. However, the spin trapping at the interface states is not ruled out [32]. In addition, evidence of a local magnetostatic field at the ED Fe/GaAs interface is presented.

1.3. Thesis Organization

The thesis is arranged as follows. Chapter 2 describes the detailed procedures of electrodeposition and of the fabrication process of the contacts. Chapter 3 describes the structural properties of Fe/GaAs investigated by X-ray diffractometry, transmission electron microscopy (TEM), and atom probe tomography. Chapter 4 describes the magnetic properties measured by superconducting quantum interference device (SQUID) magnetometry, ferromagnetic resonance (FMR), and magneto optical Kerr effect (MOKE) imaging. Chapter 5 describes the electrical and spin transport measurement techniques, and results. A comparison of the experimental findings of the spin transport measurements with predictions from existing theory is described and a new theoretical explanation is proposed. Finally, Chapter 6 presents the conclusions and Chapter 7 offers some suggestions for future work.

2. Electrodeposition and Fabrication

2.1. Growth Process

In the galvanostatic electrodeposition process a constant current is applied through two electrodes immersed in an electrolyte. The electrolyte consists of positive metal ions in our case Fe^{+2} obtained through the dissociation of an Fe salt ($FeSO_4$). The negative electrode is the semiconductor, GaAs, where the Fe^{+2} ions are eventually reduced to Fe metal adatoms via the reaction with two electrons, e^-, equation (2.1).

$$Fe^{+2} + 2e^- \leftrightarrow Fe \ . \tag{2.1}$$

During nucleation, the Fe adatoms will collect into Fe metal nuclei that once large enough will subsequently grow into an island on the semiconductor sample [40-42]. These processes depend on the over-potential (η) developed at the sample surface (potential difference between the sample surface and the double layer formed by the adatoms), which can be related to the applied current density, *J*, for a galvanostatic ED process as [41],

$$\eta = \frac{RT}{nF} \ln\left(1 - \frac{J}{J_L}\right), \tag{2.2}$$

where J_L is the limiting current density to grow isolated nuclei, *R* is the gas constant, *n* is the number of electrons per metal ion reduced, and *F* is the Faraday constant. The growth is limited by both the electrical force and the rate of diffusion of the adatoms towards the sample surface. The nucleation rate, N_u is given by [41]

$$N_u = A\, e^{\frac{-B}{\eta^2}}, \tag{2.3}$$

where *A* and *B* are constants independent of the over-potential.

The subsequent growth is limited eventually by diffusion of Fe ions to the sample adding to existing nuclei. The time (t_S) required to reach this steady state is given by the Sands relationship [43]:

$$t_s = \frac{\pi D z^2 F^2 c_0^2}{4J^2}, \tag{2.4}$$

where D is the ion diffusion coefficient, z is the ionic charge, and c_0 is the bulk electrolyte concentration. For our cell conditions, Fe^{+2} diffusion is estimated to occur with a D of 10^{-5} cm^2/s [44].

The growth rate should be directly proportional to the applied current (I), provided all charge transport is via the metal ions and metal deposition is the only process. Therefore, if only Fe^{+2} ions transport charge in the electrolyte the total number of Fe atoms, N, deposited is equal to half of the total charge, $Q = \int Idt$, that flowed through the electrolyte in time, t [45]. This can be related to the total mass of the deposited Fe atoms (M) as follows:

$$M = N\frac{M_W}{N_A}, \tag{2.5}$$

where N_A is Avogadro's number and M_W is the molecular weight of Fe. Therefore, the expected thickness S, in terms of an applied constant current, I, and time, t, can be expressed as,

$$S = \frac{ItM_W}{2eN_A D_w A}, \tag{2.6}$$

where D_w is the density of the material, A is the area of deposition, and e is the electronic charge,

2.2. Experimental Technique

The electrodeposition apparatus consisted of two electrodes in an electrolyte, through which a DC current was passed. A schematic diagram of our apparatus is shown in Fig. 2.1. A n-GaAs sample (specifications for the samples used for this thesis are given in Table 2.1) was used as the cathode, (negative electrode) and a small

platinum (Pt) rod (1 mm in diameter and 20 mm in length) formed the anode (positive electrode). Electrodes were submersed vertically into an aqueous buffered solution of ferrous sulphate ($FeSO_4$, 0.1 M) and ammonium sulphate ($(NH_4)_2SO_4$, 0.3 M) (pH of 4.2) in a beaker (20 ml) with a separation of 1 cm. Ferrous sulphate dissociates into Fe^{2+} and $(SO_4)^{2-}$ ions in the electrolyte. When current is driven through the electrolyte, positive Fe ions drift towards the cathode, adsorb onto its surface, and are eventually reduced to neutral atoms.

Electrodeposition was performed at room temperature (RT) 22°C (average) or at 50°C via a heated bath controlled by a thermostat (accurate to 0.1° C). The experimental arrangement and electrodeposition process was designed and optimized by Bob Bao (former student in our lab) [23]. Constant current was supplied by a Keithley 220 power supply (0.1 mA/mm^2 for Fe on bulk GaAs samples in Table 2.1) and automated through a desktop computer running a Labview program.

The electrodeposition process can be performed either using constant current (galvanostatic) or constant voltage (potentiostatic) sources. We adopted the galvanostatic configuration for primarily one reason: The average ion flux (current density) at the GaAs surface could be maintained constant independent of any variations in the resistance of other components of the cell, such as the sample resistance, and ohmic contact resistance. In this approach the voltage drop between the GaAs and the electrolyte varies with Fe deposition area.

The most important factor that was necessary to reproduce quasi single crystalline Fe on bulk GaAs sample was careful cleaning of the sample and apparatus. Cleaning of glassware included an acid rinse (concentrated sulfuric, 2 min.) followed by multiple rinsing and sonication in doubly-deionized (DI) water and isopropanol, ending with DI water. The area of the sample to be deposited onto was defined using photoresist (type AZ 704) painted to cover the sample edges and back side, as shown in Fig. 2.2, applied at least two hours prior to Fe deposition. The maximum area was typically 60 mm^2. The sample was then rinsed in running DI water for 20 min.

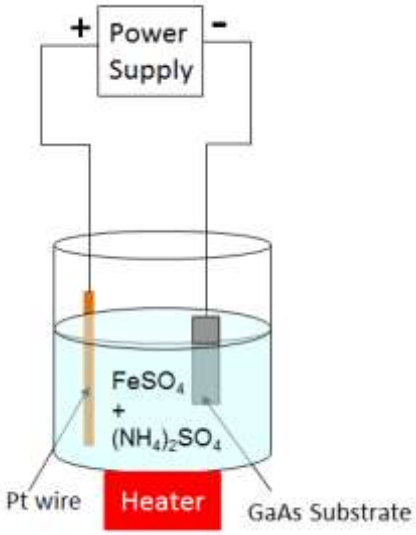

Fig. 2.1. Schematic diagram of the electrodeposition apparatus.

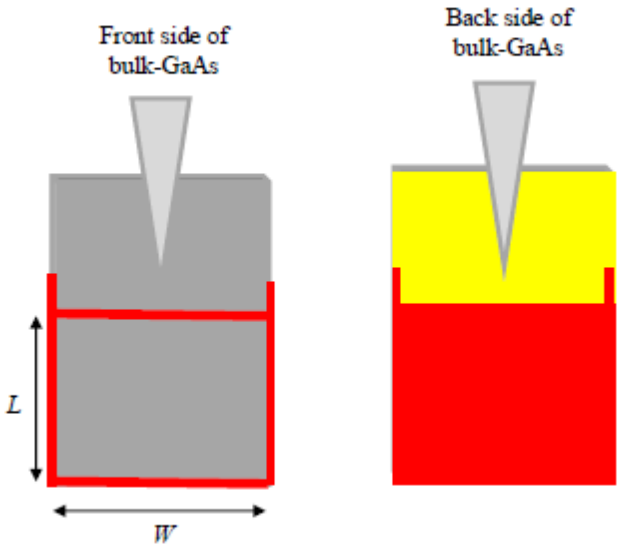

Fig. 2.2. Schematic diagrams of the front and back sides of a bulk GaAs sample (grey) prior to deposition, where photoresist paint (red) coats the edges and backsides exposed to the electrolyte, an InGa eutectic alloy forms the ohmic contact (yellow) and tweezers are used as the top electrical lead and clamp (light grey).

The In-Ga eutectic alloy was applied uniformly onto the back of the bulk GaAs samples or onto the front of the epi-GaAs sample to ensure good ohmic contact. The native oxide was etched in ammonium hydroxide solution (10%, 10 – 12 s). This process was found to optimize the degree of epitaxial growth using electrodeposition, compared to other chemical approaches to native oxide etching, including HCl, and HF [23]. The GaAs sample was connected to the power supply (pre-polarized to 15V) before dipping it into the electrolyte. The deposition time was typically a few seconds to 1 minute depending on thickness requirements.

Table 2.1 lists the GaAs samples used to produce Fe/GaAs contacts. Samples of type B are bulk GaAs wafers with a miscut of 0.5° supplied by AXT. Samples of type E are made of epi-GaAs layers grown on semi-insulating (S.I.) un-doped GaAs substrate. The samples E1 and E2 were provided by two collaborators with specialized compound semiconductor growth systems, metal-organic chemical vapour deposition (MOCVD) and molecular beam epitaxy (MBE) respectively [46, 47].

Table 2.1. Specifications for the GaAs samples used for this thesis.

Type of sample	Name	Si dopant concentration (cm^{-3})			Orientation
n-doped bulk GaAs substrate	B1	3×10^{17}			110
	B2	3×10^{17}			100
	B3	3×10^{18}			100
Epitaxial GaAs layers on S.I. un-doped GaAs substrate	E1	2×10^{18}	2×10^{18} to 4×10^{16}	4×10^{16}	100
	E2	5×10^{18}	"	"	100

For spin structures, we required Fe deposition onto epi-GaAs layers grown on S.I. un-doped GaAs substrates (listed in Table 2.1). The particular choice of the test structures followed optimized designs from previous work [48]. The total thickness of conducting *n*-type epi-GaAs layers were 2.53 μm, much thinner than bulk GaAs samples (375 μm). The conducting layers consisted of the channel, *n*-GaAs, (3.9×10^{16} cm^{-3}, 2.5 μm) followed by a linearly-graded doped transition layer (15 nm) to the heavily-doped surface layer, n^+ -GaAs (15 nm, 2 or 5×10^{18} cm^{-3}). Diagrams showing the dimensions of (a) bulk GaAs sample and (b) epi-GaAs layers are shown in Fig. 2.3. Given that the resistance of the GaAs, $R_s = \left(\frac{L}{W}\right)\left(\frac{\rho}{s}\right)$ varies inversely with the thickness, *s*, and with width, *W,* and increases linearly with distance *L* from a top ohmic contact, there is a resistance gradient along the length of the sample. Due to the much thinner epi-GaAs, extra preparation and optimization for the applied current was required to accommodate a higher resistance than that of the bulk GaAs sample. For example, bulk GaAs samples B1 or B2 (3×10^{17} cm^{-3}) have a resistivity of 4.4 mΩ.cm (Table 2.2) and thickness 375 μm, giving a resistance of 0.1 Ω, if *L* = *W*. In comparison, the resistivity of each layer of the epi-GaAs sample for a current direction parallel to the surface, given the thicknesses of each layer above, are 1.5, 2.2, and 38.9 mΩ.cm, respectively. This corresponds to a resultant resistance of 121Ω, (*L* = *W*). Thus, the resistance gradient along the length of a cm square deposited area will be 0.01 Ω/mm for bulk GaAs sample and 12 Ω/mm for the epi-GaAs sample, about 1200 times higher. These numbers represent the difference given current flows from top to bottom. In the actual cell, current flows from the top out the side of the sample which means that the current will be greater towards the ohmic contact compared to the bottom of the deposit. This gradient will be more important for the higher resistance epi-GaAs sample.

A simple circuit diagram of the process is shown in Fig. 2.3 (c). In this diagram $R_{contact}$ and R_o are the resistances at the ohmic contact to the sample, and the resistance of the sample outside the electrolyte, respectively. R_1, R_2, and R_3, etc. are the resistances along the length of the sample ($R_1 < R_2 < R_3$) inside the electrolyte. R_{elect} and R_{Pt} are the resistances of the electrolyte and the platinum electrode, respectively. Measurement of the electrolyte resistance was carried out using two Pt electrodes. This resulted in a resistivity of 1.0 kΩ.mm. For our typical setup with an electrode spacing of

1 cm and sample area 40 mm^2 (exposed to the electrolyte), the resistance of the electrolyte is 250 Ω. So, the resistance of the electrolyte is higher than bulk GaAs samples but comparable to the epi-GaAs samples. The nucleation rate (Equation 2.3) of metal on the semiconductor electrode depends primarily on the over-potential of the sample. This over-potential depends on the applied current density (Equation 2.2). The uniformity of the deposited film on the epi-GaAs sample then depends on any gradient of the over-potential along the length of the sample which varies due to its resistance gradient [40-42].

Table 2.2. Parameters used for the calculation of the resistance of the GaAs samples.

Type of sample	Doping n cm^{-3}	Thickness s μm	Mobility μ $cm^2V^{-1}s^{-1}$	Resistivity $\rho = \frac{1}{nq\mu}$ mΩ cm	Resistance (L = W) $R = \frac{\rho}{s}$ Ω
B	3.0×10^{17}	375	4700	4.4	0.1
Epi-GaAs layers	5.0×10^{18}	0.015	1316	0.9	600
	2.0×10^{18}	0.015	2051	1.5	1000
	1.0×10^{18}	0.015	2834	2.2	1466
	4.0×10^{16}	2.5	8244	38.9	152

During electrodeposition, the initial nucleation at a particular position of the sample is influenced by the over-potential at that point (which depends on the sample resistance at that position). For the thicker bulk GaAs sample, the resistance gradient

along the length of the sample is smaller than for the thin epi-GaAs sample. It was feasible to electrodeposit uniformly on bulk GaAs sample over an area of 6 mm × 8 mm, whereas for epi-GaAs sample Fe deposition occurred only within 1 mm from the top ohmic contact. Thinner patches located further from the ohmic contacts indicated that these regions did not see the sufficient over-potential required for a uniform initial nucleation of Fe.

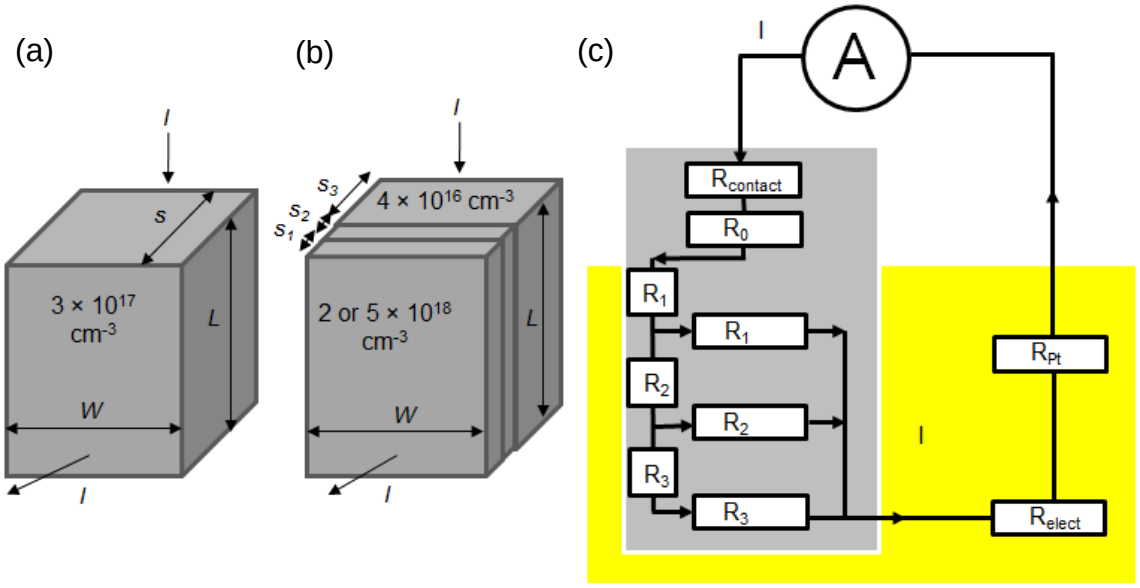

Fig. 2.3. Diagrams showing the dimensions of (a) bulk GaAs sample and (b) epi-GaAs layers with (c) a drawing of a circuit diagram, sample (grey region), electrolyte (yellow), and resistances R_x where x, is *elect,* for electrolyte*; Pt,* for the Pt anode*; contact,* for the sample ohmic contact*; "o"* for sample outside the electrolyte*; 1, 2, and 3* for the sample resistance within the electrolyte. The current enters the samples from an ohmic contact at the top side through the cross-sectional area, width × thickness, W × s, and flows along the length, L, exiting to the electrolyte perpendicular to the top surface. There is a gradient in the resistance along L, depicted as R_1 … R_3 etc., due to varying path lengths inside the sample to the surface exposed to the electrolyte.

To improve the uniformity of Fe nucleation and growth, ohmic contacts to the surface layer of epi-GaAs samples were made on both ends of the sample by placing a Cu foil from the top to bottom end of the front surface at the back of the sample as shown in the diagram in Fig. 2.4 (orange regions). To avoid current and water leakage,

the Cu foil and the edges of the sample was sealed using epoxy (green region on orange, and only green in Fig. 2.4). Fig. 2.4 also shows the deposited area outlined by photoresist paint (red), and its position with respect to the ohmic contact made to the epi- GaAs sample via an In-Ga eutectic alloy (yellow) and tweezers (grey).

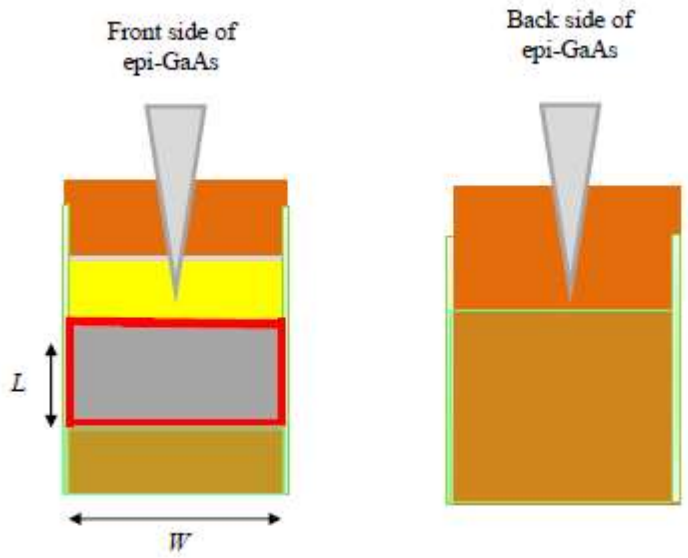

Fig. 2.4. Schematic diagram of the front and the back sides of an epi-GaAs sample ready for electrodeposition. Cu foil (orange) was wrapped from top to the bottom of the sample around the back. Tweezers (grey) made the electrical connection via an ohmic contact using the eutectic In-Ga alloy (yellow) on the front side of the sample. Photoresist paint (red) defined the deposition area and epoxy on top of the Cu (green and orange) was used to isolate the Cu from the electrolyte. Epoxy (green) was also applied at both edges of the sample to prevent deposition and any leakage of the electrolyte to the Cu and the sample. The applied current was calculated based on the exposed area of sample and desired constant current density.

2.2.1. Results

A typical example of a plot of electrochemical cell voltage, *V*, versus time, *t*, for a constant current of 2.4 mA, for Fe deposition onto a sample B1 (24 mm^2) is shown in Fig. 2.5. The initial open circuit voltage is limited primarily by the compliance voltage of the power supply, 12 V in this case. When the pre-polarized sample is placed into the

electrolyte (shown by arrow), *V* abruptly drops completing the circuit. The decrease occurs within 0.25 s, as shown in inset (a) of Fig. 2.5. With increasing *t*, *V* then increases, shown in inset (b) of Fig. 2.5, typical of a diffusion-limited process. The development of a concentration gradient occurs through the depletion of Fe ions near the GaAs electrode depositing as a film. This process leads to an increase in the cell resistivity and thus its voltage.

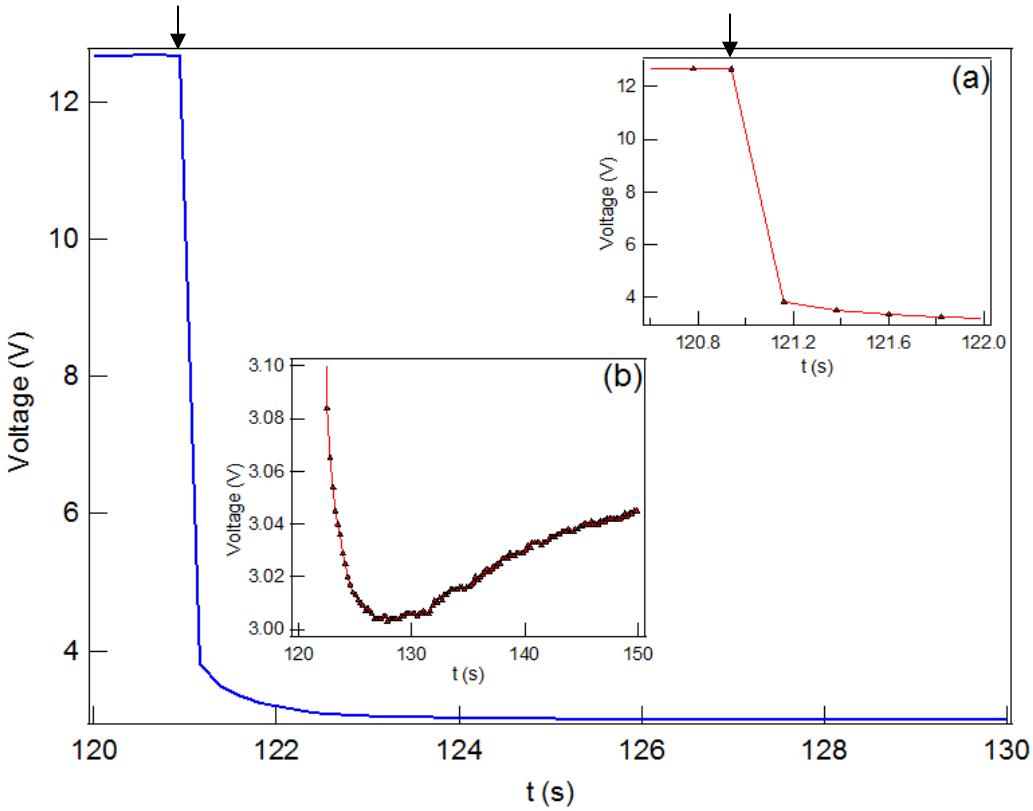

Fig. 2.5. Plot of an electrochemical cell voltage (*V*) versus growth time (*t*) for Fe on sample B1. Inset (a) shows the initial voltage drop (< 0.5 s). Inset (b) shows the increasing voltage with increasing *t*, after the initial drop when the sample is inserted into the electrolyte (shown by arrow).

The average Fe film thickness measured from focussed ion beam (FIB) cross-sectional scanning electron microscopy (SEM) images as a function of growth time for Fe on sample B1 at RT is shown in Fig. 2.6. (a). An example SEM image of a sample grown for 60 s is shown in Fig. 2.6. (b). In the image the sample is tilted 52° with respect to the electron beam about a horizontal axis meaning that the average film thickness is

the measured image value times sin 52°, in this case, 245 ± 30 nm. The Fe/GaAs interface is visible due to the greater probability for secondary electron emission from the metal compared to *n*-GaAs. The film is continuous with a surface roughness on the order of 10–20% of the total thickness. The smooth striations in the film and substrate along the growth direction are FIB artifacts. The solid line in Fig. 2.6. (a) is the calculated thickness assuming a total cell current density of 0.1 mA/mm^2 carried by Fe^{+2} ions to the GaAs sample with 100% deposition efficiency (equation 2.6). The growth rate at RT is constant, to within experimental error, for the first 30 s but then decreases. The average growth rate is initially 6 nm/s, determined by the current, but decreases to 3 nm/s (or 120 nm/min) by 60 s of growth.

For our conditions, equation 2.4 predicts this transition time away from linear behavior (Sand's time) (t_s) to be 10 s, on the order of the time at which our depositions began to deviate from a linear growth rate. Parallel transport processes, such as the dissociation of water at the cathode leading to the formation of H_2 gas, may also be contributing to changes in the cell voltage.

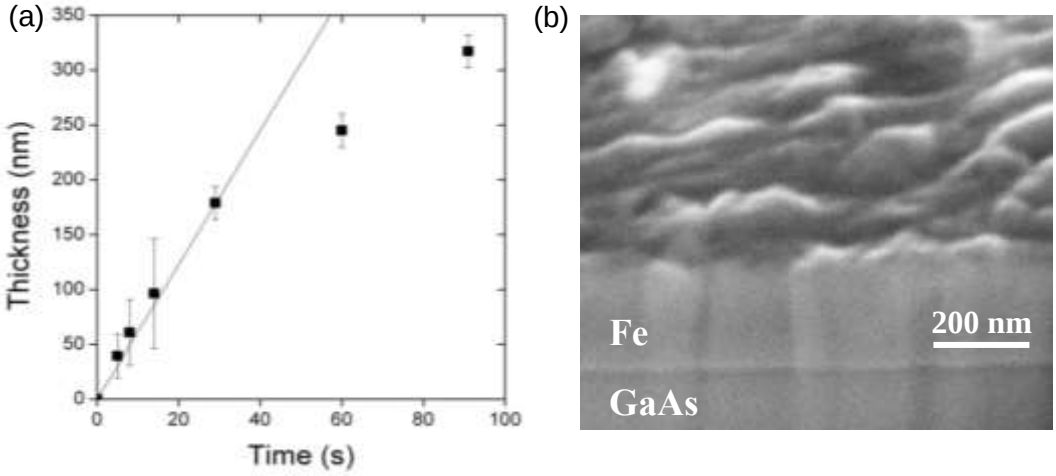

Fig. 2.6. Plot of (a) thickness of Fe film grown at RT on sample B1 versus growth duration and (b) an example of a secondary electron microscopy image (sample tilted 52°) for the sample grown for 60 s (B1-4). The measured thickness in this case was 245 ± 30 nm. The solid line is a linear fit including zero time.

Table 2.3 lists all samples prepared by electrodeposition of Fe on bulk wafers (type B). The sample no. is assigned depending on the particular type of bulk wafer used for the deposition as was listed in Table 2.1. Substrate orientation is given in the second column. Growth time, temperature, and current density applied for the deposition are listed in the consecutive columns. The last column lists the measurements performed on the sample.

Table 2.3. Specifications of samples of ED Fe on bulk GaAs substrate (type B, Table 2.1) for which data are presented in this thesis.

Sample no	Orienta-tion	Growth Time (s)	Growth Temperature (° C)	Current density (mA/mm^2)	Measurements
B1-1	110	8	22	0.1	XRD,TEM
B1-2	"	14	"	"	XRD,HRXRD,TEM, SQUID,FMR
B1-3	"	30	"	"	XRD,SQUID,APT
B1-4	"	60	"	"	XRD,SQUID
B1-5	"	90	"	"	XRD,HRXRD,TEM
B1-6	"	34	50	"	XRD,APT
B1-7	"	86	"	"	XRD,HRXRD,SQUID,TEM
B1-8	"	97	"	"	XRD
B2-1	100	15	22	"	*I-V*
B3-1	"	15	"	"	"

Similarly, Table 2.4 lists samples of Fe prepared on epi-GaAs (type E). Samples B1-2, B1-5, and B1-7 in Table 2.3; and E1-7, and E1-8 in Table 2.4 are the most important samples as many measurements were performed on a single sample. Atom probe tomography was performed on samples B1-3 and B1-6. Spin measurements were performed for samples E1-7, E1-8 (two structures) and E2-2.

Table 2.4. Specifications of samples of ED Fe on epi-GaAs samples (type E, Table 2.1) for which data are presented in this thesis.

Sample no	Orienta-tion	Growth Time (s)	Growth Temperature (° C)	Current density (mA/mm^2)	Measurements
E1-1	"	15	22	0.05	XRD
E1-2	"	"	"	0.08	"
E1-3	"	"	"	0.1	XRD,HRXRD
E1-4	"	"	"	0.15	XRD,HRXRD
E1-5	"	"	"	0.2	XRD,HRXRD
E1-6	"	9	"	0.15	TEM
E1-7	"	15	"	"	HRXRD,SQUID, TEM,MOKE, *I-V*, Spin Valve
E1-8	"	"	"	"	*I-V*, Spin Valve, Hanle
E2-1	"	"	"	"	*I-V*
E2-2	"	"	"	"	*I-V*, Hanle

2.2.2. Summary

Two types of GaAs samples (bulk GaAs wafer and epi-GaAs layers grown on S.I. un-doped substrate) were used for Fe deposition. The resistance of the epi-GaAs samples was three orders of magnitude larger than the bulk GaAs samples. This increased the likelihood of non-uniform nucleation and growth of Fe over the area of the sample. The voltage gradient was reduced by producing a more constant field using contacts on all sides of the area to be deposited via a Cu foil rather than just at the top and limiting the total length of the deposited sample to 8 mm.

The growth rate of Fe on bulk GaAs samples (Fig. 2.6) was found to be constant up to 30 s as expected from theory. A subsequent decrease with increasing growth time is likely related to the depletion of Fe ions near the sample surface.

2.3. Fabrication of Spin Test Structures

As mentioned already, the design of our spin test structures was inspired by those of Lou et.al [11]. Their strategy was to have the thinnest tunnel barrier feasible, both to avoid spin scattering that predominantly occurs at dopant atoms, and to reduce the interfacial resistance before reaching the lower-doped semiconductor channel. Fig. 2.7 shows a schematic diagram of a cross-sectional view of the epi-GaAs sample used in our work with the nominal thicknesses and dopant concentrations. They consisted of a bulk semi-insulating GaAs (100) substrate (350 μm) upon which was epitaxially grown a buffer layer (300 nm un-doped GaAs), a Si-doped *n*-GaAs channel (2.5 μm, 4×10^{16} cm^{-3}), and a graded-doped layer (15 nm) transitioning to a heavily-doped n^+ surface layer (15 nm, 2 or 5 $\times10^{18}$ cm^{-3}). The n^+-GaAs layer produces the tunnel barrier between the deposited ferromagnetic metal layer and the GaAs spin channel. The doping concentration and the thickness of this layer determine the interface resistance which dictates the tunnelling probability of the spin polarized electrons. The *n*-GaAs layer is the spin channel designed to have a lower doping concentration optimized for maximum spin transport between lateral contacts [48].

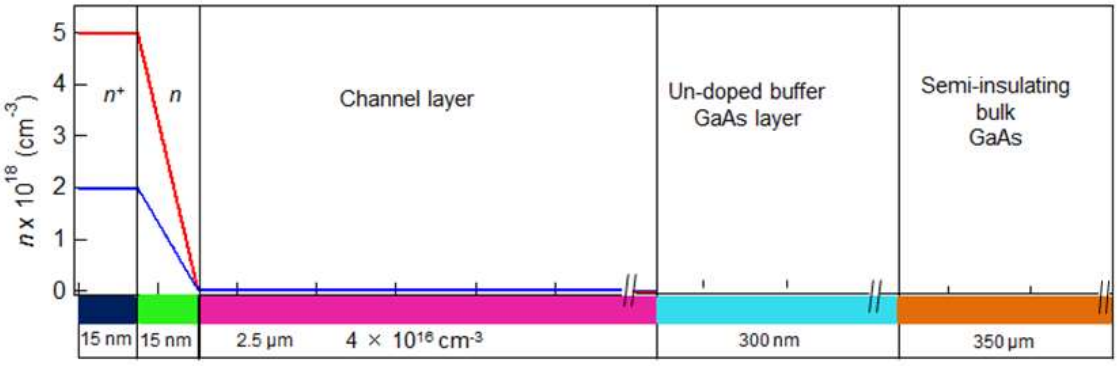

Fig. 2.7. Schematic diagram of a cross-sectional view of the epitaxially grown GaAs layers on a semi-insulating, bulk (001) GaAs substrate indicating the layer thicknesses and dopant concentration profile (not to scale).

To fabricate the required spin structure two methods of making ED Fe contacts on the epi-GaAs sample were considered. The first option was to make a blanket ED Fe film onto the sample, then pattern photoresist via lithography masking Fe bars (10 µm × 50 µm), and finally etching (dry or wet) the unwanted Fe. The second option was to prepare a photoresist mask on the sample with openings for the Fe contacts (10 µm × 50 µm) and then electrodeposit Fe directly into them. The first option (both wet and dry etching) failed to work for Fe films of 100 nm thickness. Wet etching was tried with various concentrations of dilute HCl or HCl + HNO_3 (1:1) solutions (concentrations starting at 1%, etching times from 3 s to 15 s) with and without surfactants. Surfactants can help to dissolve the etched material into the acid solution and also to reduce the rate of re-deposition of etched material onto the sample surface [49]. All of these trials failed primarily because lateral etch rates were much higher than vertical etch rates and feature size could not be controlled. Dry etching of Fe was tried with a chlorine gas plasma using Cl_2 + Ar, or Cl_2 + BCl_3. These trials also failed since hard-baked photoresist residues could not be removed without subsequent oxygen plasma cleaning (30 mins). Direct oxygen exposure to the ED Fe would cause damage to the surface of the film. Also a problem was the chlorine residues left on the surface of the sample after etching which corroded the Fe film even after thorough rinsing of the sample with deionized water for 10 mins. Details of these trials are described below.

Wet etching of Fe is feasible with aqueous HCl or HCl + HNO_3 (1:1) solutions (1% to 0.125% in double distilled water). In both cases the rate of lateral etching was greater than vertical etching such that no Fe remained on the sample for film thicknesses of 100 nm to 150 nm. Etching times were 3-6 s for the higher acid concentrations and became very non-uniform over the sample surface for the lower acid concentrations. To dissolve Fe from all non-desired areas with a lower concentration of acid, the sample needed etching times of 2-6 minutes. Figure 2.8 shows examples of the end results for two processes for a Fe film thickness of 100 nm ± 15 nm and a photoresist mask area of 10 µm × 50 µm (a) etched in HCl + H_2O solution (1:400) for 3 minutes and (b) in HCl + HNO_3 + H_2O (1:1:600) for 5 minutes at RT. The photoresist bars are clearly outlined by the dark line. Both show only small regions of discrete Fe films (yellow dots, patches or thick lines) left underneath the photoresist on the sample. Both images indicate that 5 µm of lateral etching underneath the photoresist had occurred to obtain 100 nm in the vertical direction. Reducing the etch time for this acid concentration resulted in patches of incomplete vertical etching with similar large degree of under etching.

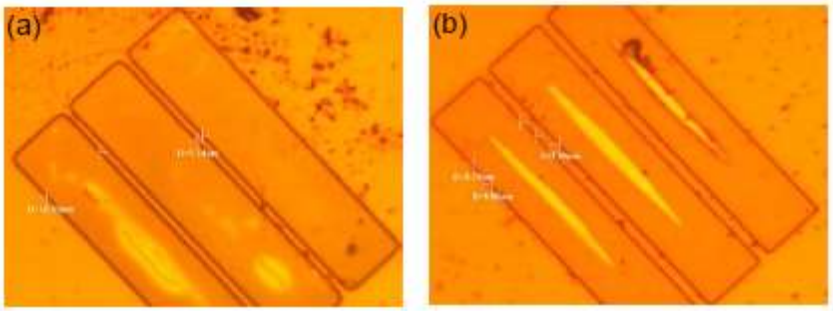

Fig. 2.8. Optical micrographs of 3 etched Fe pads. The remaining yellow patches are the Fe inside the thick darker outlines of photoresist bars that originally masked the desired Fe bar area of 10 µm × 50 µm. Traces of the 100 nm Fe film are also left on the substrate after (a) etching in aqueous HCl + H_2O (1:200) for 3 min, and (b) aqueous HCl + HNO_3 + H_2O (1:1:400) for 5 min indicating lateral etching on the micrometer scale while vertical etching only in the nm range.

After unsuccessful trials with wet etching of Fe, reactive ion etching using a RF (radio frequency) plasma with two different gas compositions, Cl_2 + Ar, or Cl_2 + BCl_3 were tried. The known issues were the reactivity of the gas composition towards photoresist and the exposed surface, and incomplete etching to avoid damage to the photoresist or the etched surface for a Fe film thickness of 100 nm - 150 nm.

The Cl_2 + Ar combination was more aggressive than Cl_2 + BCl_3 towards the photoresist and the etched surface. Also, any long (> 2 min) gas exposure of the photoresist (PMMA) layer eventually oxidized and disrupted the underlying Fe film. Hard baked photoresist left inadvertently on the Fe surface (etch time > 1 min for both gas combinations) was difficult to remove in acetone or resist remover (80 °C for 4-6 hrs). Another major issue was oxidation of etched Fe bars a few weeks after long (> 1 min) Cl exposure; oxidation would start at the edges and eventually spread over the entire bar. Etching could be done successfully without affecting the photoresist for Fe film thicknesses of up to 10 nm in approximately 20 s. But the thinnest continuous ED film thicknesses feasible were 100 nm. Figure 2.9 (a) shows regions of Fe bars patterned using dry etching, after removal of photoresist. Energy-dispersive x-ray spectra (EDS) have been obtained from the region (I) and (II). (b) shows a SEM image of the edge of a Fe bar shown in Fig. 2.9 (a) with a 60° tilt and with a starting thickness of 130 nm $\pm$ 30 nm (based on growth time) after 2.5 min using a Cl_2 + BCl_3 gas mix (9:1, 7.5 mTorr and 100 W). The EDS detects the presence of Fe over the entire sample indicating incomplete etching. Note that the image shows a film thickness of 173 nm larger than the 130 nm Fe thickness since the photoresist layer was hard baked and remained on the Fe surface.

Patterning a blanket Fe film by wet or dry etching was not feasible. The second option was to pattern a photoresist (PMMA) mask on the epi-GaAs sample and then to deposit the Fe layer directly into the mask openings. This did succeed but there were other challenges using this method. Cleaning of the sample before PMMA spin coating was crucial for uniform adhesion of the photoresist to the sample surface. Otherwise, the PMMA pattern lifted off during subsequent native oxide GaAs etching (NH_4OH aqueous solutions). There is an increased resistance at each corner; therefore the deposition of Fe differed at the edges as compared to the middle of the bar. Removal of PMMA residue after e-beam lithography is usually performed via photoresist stripping in oxygen plasma (50 W for 3 min.). But oxygen plasma will oxidize the GaAs surface prior

to Fe deposition. The patterned epi-GaAs sample was only rinsed with deionized water for 1 minute before deposition.

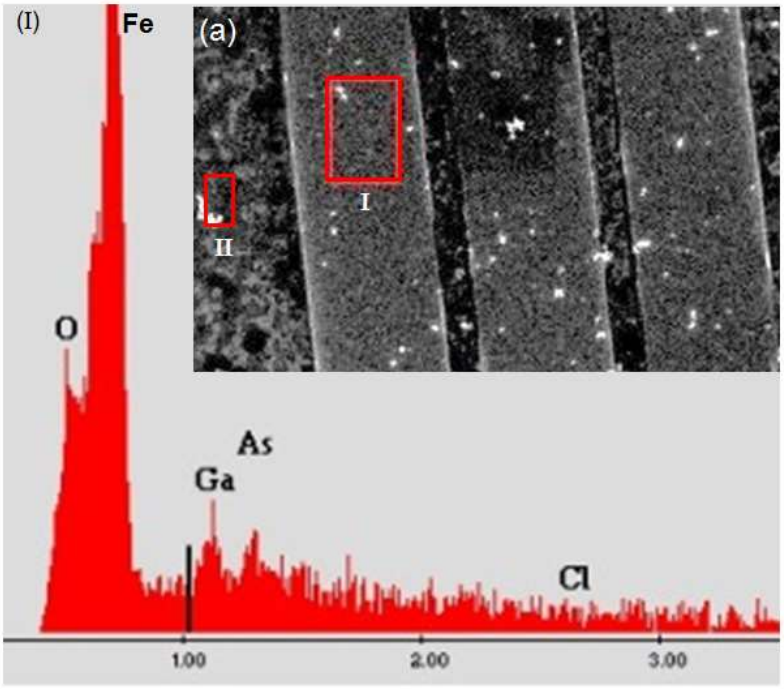

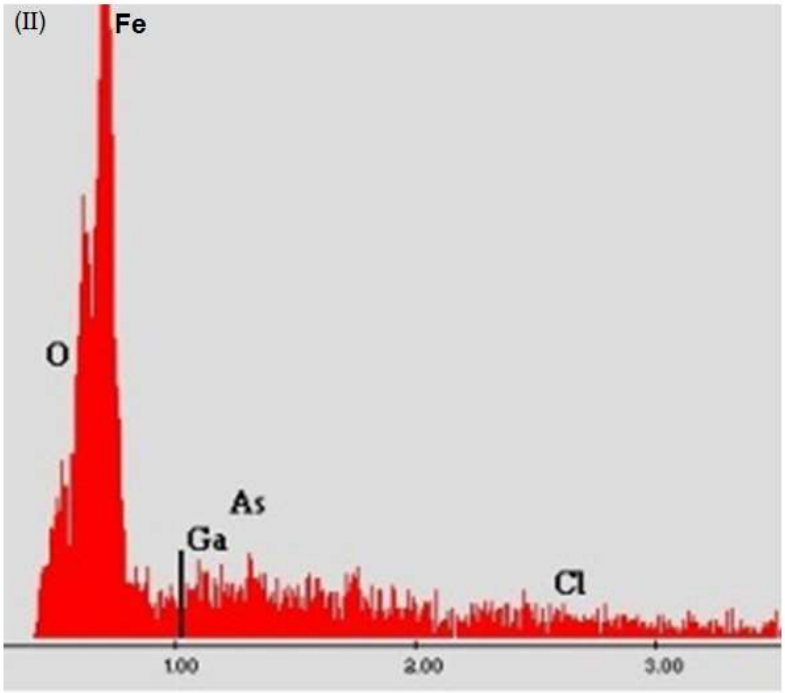

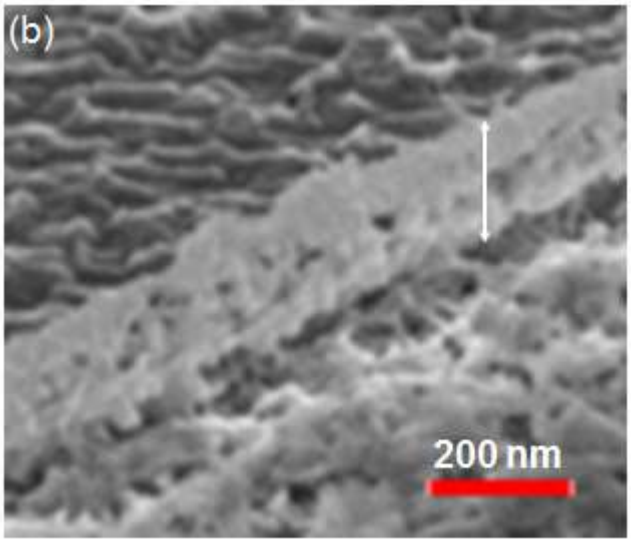

Fig. 2.9. (a) SEM image of a dry-etched sample after removal of photoresist. The region where 3 Fe bars were patterned is visible but EDS from regions (I) and (II) shown in associated spectra indicate that the Fe was not completely etched. (b) SEM image of the sample in (a) tilted 60° at an edge of a bar revealing a thickness of 173 nm that is composed of both Fe and residual photoresist. The Fe was 130 nm based on the growth time, indicating a contribution from remaining hard baked photoresist of 43 nm.

Fe bars of the spin structure were fabricated at an angle of 45° with respect to the edge of the sample (GaAs [110] directions) to make the length of the bars along in-plane GaAs [100] directions. The spin structure had five more process steps after ED of the Fe bars: a 50 nm protective gold, two GaAs etchings, one SiO_2 sputter deposition, and a gold deposition for contact pads and vias. E-beam lithography was used to pattern each layer. Figure 2.10 shows a schematic diagram of the fabrication process for each layer.

A protective gold layer of 50 nm was to protect the Fe layer from the photoresist cleaning agent (1165 photoresist remover) used to remove PMMA residues after each layer was done. GaAs doped layers were etched to a depth of 2.8 μm down to the semi-insulating substrate to ensure that there was no electrical connections between the spin structures. The n^+ and n^+ to n heavily-doped tunnel layers between the contacts were removed with an etch to a thickness of 50 nm. A SiO_2 layer (thickness 180 nm) was sputtered all over the sample, except for small windows on each Fe bar for the surface

Au pads. Gold pads of 150 µm × 150 µm and vias (180 nm thick, 60 to 150 µm) were evaporated to provide wire bonding pads to connect the device structures to the dual in line package (DIP).

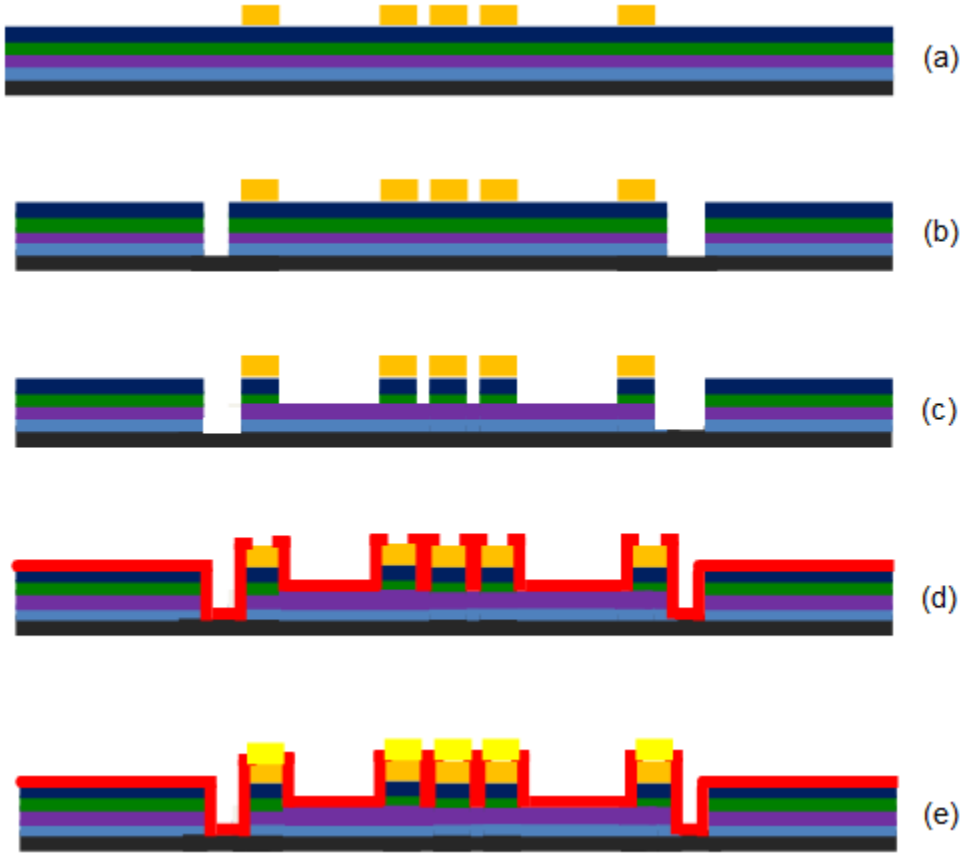

Fig. 2.10. Diagrams in cross-sectional view of the fabrication procedure. (a) After the Fe bar electrodeposition on the epi-GaAs sample. Fe contacts (10 µm × 150 µm) were placed 2 µm apart in the middle and 160 µm at either side from the central three bars. Protective Au evaporated and patterned onto the Fe, 50 nm. (b) GaAs mesa layer is etched (2.8 µm) down to the semi-insulating substrate. c) Surface heavily-doped GaAs layer is etched 50 nm vertically in between the contacts to fabricate the channel layer. (d) SiO_2 is sputtered over the entire structure except for small windows on top of each Fe bar. (e) Gold is evaporated on top of the Fe bars for electrical connections. The thickness of both SiO_2 and the Au layers was 180 nm.

Individual spin structures each required an area of 1 mm × 1 mm on the sample to accommodate the gold pads and vias on the top and bottom side of the bars for ease

of gold wire bonding. The total feasible dimension of the Fe spin structures could be 8 mm × 7.5 mm based on the maximum area allowable for our ED set up ($\leq$ 60 mm^2). The individual spin structure required 1 mm × 1 mm predominantly taken up by the Au vias and pads. So the maximum number of spin structures that could be patterned within the given area was 64. The total ED Fe area of the 64 sets of spin structures is 0.48 mm^2 (1500 × 5 × 64 μm^2). This small area resulted in an epi-GaAs sample resistance that was too high meaning the applied current corresponded to a very low over-potential. No Fe deposited. For example, if the total area of the patterned geometry was 0.48 mm^2, the total current required for this area (assuming a uniform resistance) for a current density of 0.2 mA/mm^2 would be 0.09 mA. This small current was insufficient to produce the threshold over-potential required for the Fe deposition on the GaAs sample. Higher current densities eventually resulted in deposits, but adhesion was poor and the Fe lifted off. To reduce the sample resistance blanket areas (unpattern regions) were used decreasing the total number of patterned spin structures to 35 on each sample. A diagram of an 8 × 14 mm^2 sample with 35 spin structures, 7 circles for diode measurements (0.8 mm diameter) and a blanket area of 0.5 x 8 mm is shown in Fig. 2.11 (a). The bottom and top of the sample are electrically connected via a Cu foil wrapped around the back to provide an ohmic contact as mentioned. The resistance to each bar varied depending on the position of the contact with respect to the ohmic contact of the sample (at the top from tweezers and at the bottom from the Cu foil). Therefore, not all bars deposited uniformly. Optical micrographs of Fe bars grown via ED into photoresist openings at two positions at different distance from the ohmic contacts are shown in Fig. 2.11 (b) and (c). The Fe bars in image (b) are far away from the ohmic contact located at column 2 and row 3 from the left in Fig. 2.11 (a), and are missing one bar, likely ripped off during the photoresist removal process in acetone. Meanwhile the Fe bars in image (c) are closer located at column 2 and row 1 from the top in Fig. 2.11 (a), and show all three bars. The overall result is non-uniformity in deposition across the sample.

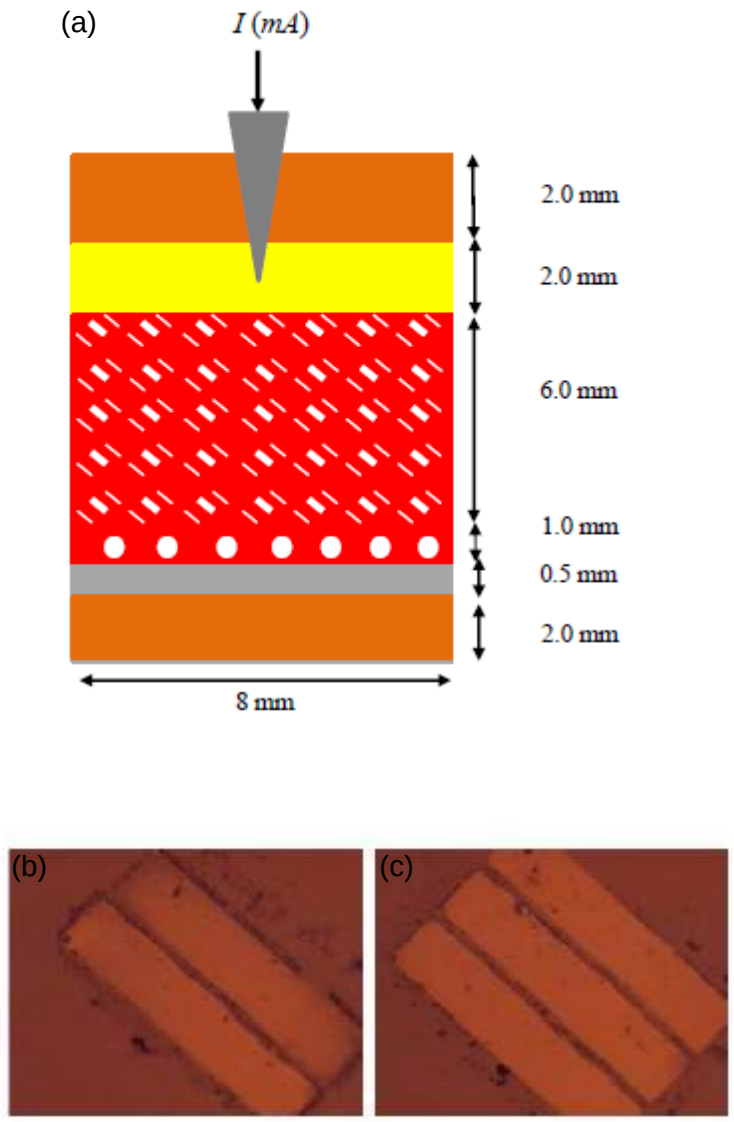

Fig. 2.11. (a) Diagram of the patterned epi-GaAs sample showing positions of patterned and non-patterned areas, the tweezers (grey) for a top ohmic contact using In-Ga alloy (yellow), and the wrapped Cu foil (orange regions, bottom ohmic contact). (b) Optical micrographs of Fe bars electrodeposited into openings in a photoresist mask for two positions with respect to the lateral ohmic contacts (b) far away (From the left, column 2 and row 3) showing one missing Fe bar, (c) closer (from the top, column 2 and row 1) with all three bars visible.

Further details of the etching, sputtering and evaporation procedures are described below: A positive photoresist (PMMA) mask was used for two GaAs layer etchings, a negative photoresist (maN2403) + LOR2B (lift off photoresist) and PMMA + LOR2B were used to define openings prior to SiO_2 sputtering and Au evaporation, respectively. After SiO_2 and Au depositions these layers were lifted off by dissolving the photoresist from the unwanted regions using photoresist remover (No. 1165). Lift off with either maN2403 or PMMA resist was difficult as both make vertical walls at the openings preventing 1165 from penetrating, stopping the lift-off process. LOR2B was used as a base layer in each case to make sure that diffusion of 1165 through the photoresist opening occurred. The spin speeds for PMMA, maN2403 and LOR2B were 3000, 2000, and 2000 rpm, respectively, with duration 40 s in all cases. The pre-bake temperature for PMMA and LOR2B was 180 °C, while maN2403 was baked at 90 °C, all for 1 min.

The channel mesa was first defined by wet etching the doped GaAs layers down to the semi-insulating GaAs substrate (approximately 2.8 μm deep) in a 20 μm wide strip surrounding the channel (50 μm × 375 μm) and the bar (10 μm × 150) areas. Etching was done in an aqueous solution of ammonium hydroxide and hydrogen peroxide ($H_2O+NH_4OH+H_2O_2$, 100:1:1) for 13.5 min. The thickness of the etched area was measured before and after using a profilometer.

The highly-doped and transition layers plus a small fraction of the channel layer were etched to a total depth of approximately 50 nm with an aqueous ammonium hydroxide and hydrogen peroxide solution (1:1:100; 3 min) defining a channel area of 50 μm × 375 μm. The depth of this etch was measured using a profilometer at the extremities of the bar areas.

The SiO_2 layer (180 nm thick) was deposited at a rate of 0.8 A/s using RF (radio frequency) sputtering (250 W in high vacuum, 10^{-6} Torr). Unwanted material and resist was lifted off by dipping the sample in photoresist remover solution (1165) (80 °C for 4 hrs). Negative resist (maN2403) left a non-uniform residue over the entire sample and made the SiO_2 deposition and subsequent lift off uneven throughout the sample. Often, I had to repeat this process step to obtain good SiO_2 coverage over the surface of the sample.

Gold (180 nm) and chromium (15 nm) were deposited via electron beam evaporation at a deposition rate of 0.8 *Å*/s and 0.5 *Å*/s, respectively to fabricate gold

pads (150 µm × 150 µm) and vias. Due to the non-uniform thickness of the SiO_2 layer, the thickness of the photoresist layer for gold deposition varied and the lift-off process became non-uniform. Sonication was one option to remove the undesired gold but not feasible since it also ripped off the Fe contacts. Instead, 1165 was used to lift off unwanted photoresist and gold (80 °C for 4 hrs). Because of this problem, I had to repeat this layer multiple times. As a result the wire bonding onto the gold pads became more challenging due to uneven pressure (depends on the smoothness of the surface) of bond needle to the gold pad.

Figure 2.12 displays a SEM image of a complete spin structure with 5 Fe bars of 10 µm × 150 µm areas on n^+-GaAs (2-5 × 10^{18} cm^{-3}) with a *n*-GaAs channel (3.9 × 10^{16} cm^{-3}) of 50 µm × 375 µm area. The three Fe bars at the center are spaced with an effective length of 4 µm (designed to be 2 µm apart but MOKE imaging to be described later showed a non-magnetic strip of 1 µm thickness on either side of each bar). The other two Fe bars are placed at either side of the central position 160 µm away from center. These bars are connected through an *n*-GaAs channel not visible in the image.

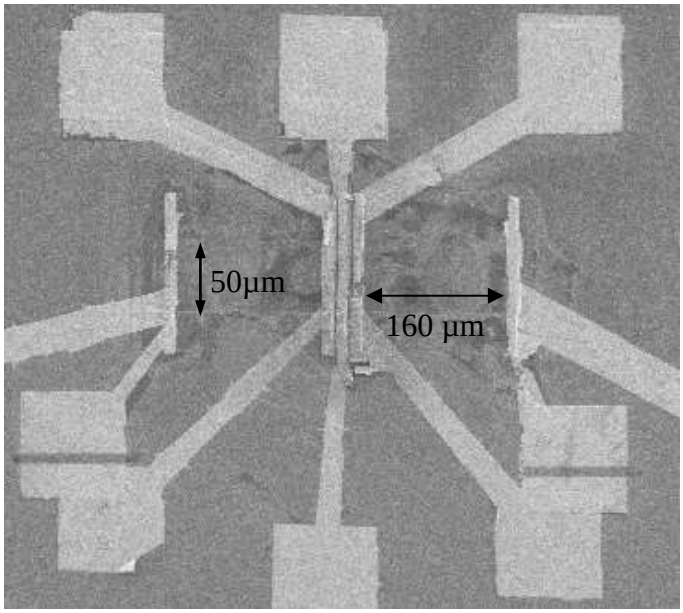

Fig. 2.12. SEM image of a fabricated spin structure with Au vias and pads. Black arrows indicate the GaAs channel width location. There are 5 Fe bars each with an area of 10 µm × 150 µm and an n-GaAs channel of 50 µm × 375 µm.

The Fe bars are longer than the channel width to reduce fringing magnetic field effects inside the channel area originating at the corners of the bars. The spin-polarized electrons tunneling from Fe into GaAs are confined within the channel width of 50 μm to make sure the effective length to width ratios for contact bars is 1:5 - standard for lateral spin contacts [50].

2.3.1. Summary

There were two methods of fabricating the Fe contact bars on epi-GaAs samples; i) etching Fe from blanket ED Fe film or ii) directly depositing into masked epi-GaAs sample areas. Wet etching was a complete failure, for 100 nm of Fe, since the vertical etch rate was slower than the horizontal rate. And dry etching was found to be corrosive to Fe films due to chlorine residues and was therefore ruled out. The second method worked better but deposition within the corners and edges of the bars was discontinuous giving discrete islands. This phenomenon can be explained as due to a higher resistance to Fe diffusion in the electrolyte in these regions. Another drawback of this option was that potential photoresist residue left on the sample after lithography reduced the adhesion of Fe film to the sample and often lead to poor film lifting during subsequent processing. Nevertheless this second method worked well enough to fabricate devices for the transport measurements presented in Chapter 5.

3. Structural Properties

The structural properties of the ED Fe film and Fe/GaAs interfaces influence the magnetic and transport properties of these contacts. In this chapter, structural analysis is described including the theory, experimental techniques and the results from x-ray diffraction (XRD), transmission electron microscopy (TEM), and atom probe tomography (APT) for both types of samples.

3.1. X-ray Diffraction

Two types of x-ray diffraction techniques, low and high resolution, were used to analyze the crystal structure of ED Fe films. The low resolution technique was easy to operate and the duration of the measurement was much shorter than for high resolution measurement. The low resolution technique was used to determine whether there was any preferred crystal orientation in the ED film with respect to the GaAs sample used for the deposition, and to estimate grain sizes if the film consisted of grains. Once the primary orientation of the film was found with respect to the substrate orientation, the high resolution technique was used to determine the details of the crystal structure of selected ED samples, e.g. lattice constants along the in-plane and out-of-plane directions of the film, the strain, and the mosaic spread of the grains.

3.1.1. Low resolution XRD technique

Crystallographic information including the dominant film orientation with respect to the substrate, degree of crystallinity and grain size, L, were determined by performing x-ray diffraction (θ - 2θ) measurements using a collimated beam from a fixed tube (Cu) diffractometer (Siemens D5000). This system had an x-ray detector slit opening of 22 arc sec (slit size 0.1 mm) and a minimum peak width of 0.027 degrees based on the full width at half maximum (FWHM) of the GaAs substrate peak. The wavelength was a

weighted average K_α ($\lambda_{K\alpha1}$ = 1.54056 *Å* and $\lambda_{K\alpha2}$ = 1.54433 *Å*), equal to 1.54178 *Å* with K_β ($\lambda_{K\beta1}$ = 1.39217 *Å*) radiation partially filtered by a Ni foil [51].

The incident and diffracted x-ray beam directions for θ - 2θ scans are displayed in Fig. 3.1. The incident angle θ is with respect to the surface of the sample. The detector is at an angle 2θ with respect to the incident beam. In the Siemens diffractometer the sample is fixed on a horizontal platform (without any goniometer) located at the axis of rotation of the x-ray tube and detector. The x-ray tube is moving clockwise from $\theta = 0$, and detector is moving anti-clockwise towards the surface normal of the sample plane.

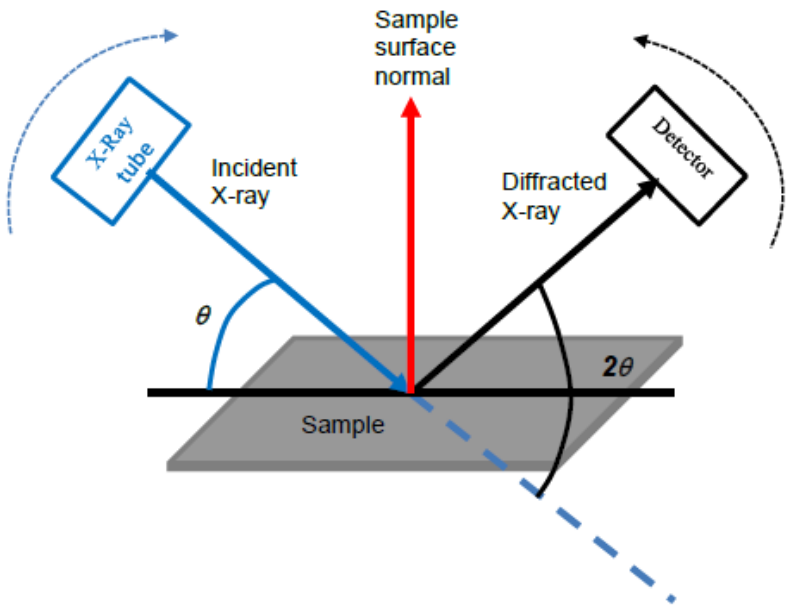

Fig. 3.1. Schematic diagram of the incident and diffracted x-ray beams for θ - 2θ measurements showing the position of the sample and the direction of rotation of the x-ray tube and the detector. Arrows indicate increasing θ and 2θ directions.

The orientation of the film is determined from the peak positions while the full width at half maxima (FWHM), $P(2\theta)$, is a measure of grain size, *L,* perpendicular to the surface, based on the Scherrer equation [51]:

$$L = \frac{0.94\,\lambda}{P(2\theta)\,\cos\theta}\,. \tag{3.1}$$

$P(2\theta)$ consists of two factors one from sample grain size and the other from broadening due to instrumental resolution. The instrumental resolution can be calculated from the FWHM from the GaAs substrate peak as mentioned in the preceding paragraph [51]. This value is subtracted from the measured sample peak width giving the portion of $P(2\theta)$ due to grain size effects used in equation 3.1.

3.1.2. High resolution XRD technique

Further analysis of the crystal structure was performed using high resolution ω - 2θ rocking curves, pole-figures and reciprocal space mapping using a collimated and monochromated x-ray beam from another fixed-tube-source diffractometer, Panalytical X-pert Pro MRD (Cu $K_{\alpha 1}$). The conditioned beam provided a higher resolution resulting in a FWHM of the GaAs (004) peaks of only 0.006° consistent with the theoretical peak widths for perfect crystals. This system was equipped with a goniometer stage that allowed accurate alignment of the sample with respect to the beam direction capable of finding both symmetric reflections, planes parallel to the sample surface, for example (110)/(220) and asymmetric reflections, planes tilted with respect to the surface by an angle ψ, for example (211)/(422). Figure 3.2 shows diagrams explaining the parameters for these two types of reflections. The diffraction vector $(\overrightarrow{k})$ and the surface normal $(\overrightarrow{n})$ overlap for symmetric reflections whereas these two are at an angle (ψ) for the asymmetric reflection. Angle ω is the rotation angle of the sample with respect to incident beam. Diffraction from the desired planes (*hkl*) of the sample (GaAs) is optimized by maximizing the intensity of the substrate peak. In general, ω is equal to the Bragg angle, θ_B, for a particular (*hkl*) only if those planes are exactly parallel to the sample surface. To calculate perpendicular and in-plane strains, $\varepsilon_{\perp}$ and $\varepsilon_{//}$, rocking curves (ω - 2θ) at symmetric and asymmetric Bragg reflections are required [52, 53]. For GaAs (220) and (422) θ_B is given in Table 3.2.

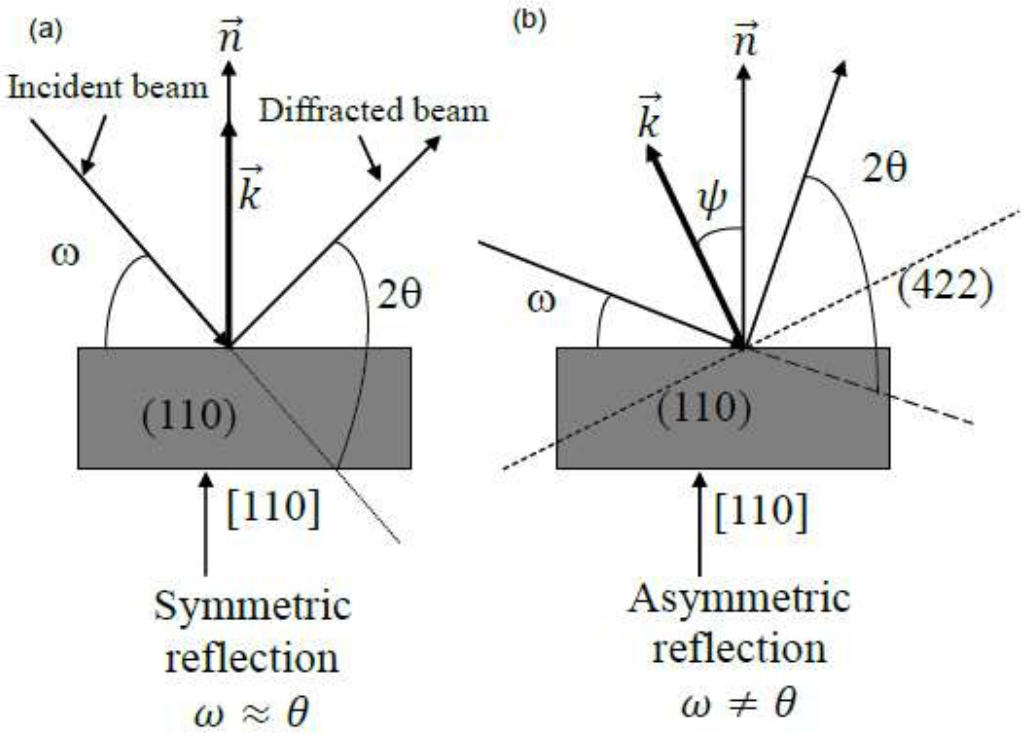

Fig. 3.2. Diagrams showing beam paths for (a) GaAs (220) symmetric and (b) GaAs (422) asymmetric crystallographic planes. The 2θ angles of the detector position are measured with respect to the incident x-ray beam direction.

Fig. 3.3 (a) shows an example of the raw data for a set of ω - 2θ rocking curves from Fe/GaAs (220) for two in-plane sample rotations ϕ about the normal axis to the surface of the sample, 0° (red) and 180° (black). Each plot consists of intensity (counts/s) versus the angle ω of the sample surface. The two peaks from the GaAs sample were not at the identical ω position due to a microscopic tilt of the sample with respect to the surface of the sample holder (mounting tilt). In (b) the GaAs peak position has been normalized to a nominal value to eliminate this effect. The parameters $\Delta\omega$ and $\Delta\psi \pm \Omega$ are extracted from the plots, where Ω is the macroscopic tilt of the film with respect to the GaAs sample planes, ψ is the angle between the (*hkl*) reflection plane and the surface of the sample, $\Delta\psi$ is the tilt in the film with respect to the GaAs sample due to strain, and $\Delta\omega^{+}$ or $\Delta\omega^{-}$ is the difference in the positions of the Bragg peaks.

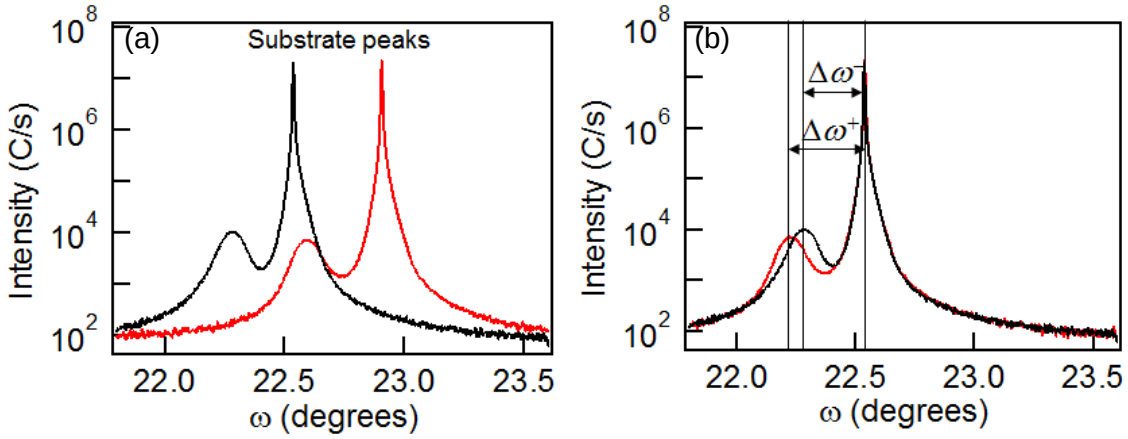

Fig. 3.3. Examples of ω - 2θ rocking curves from Fe/GaAs (110) for symmetric Bragg reflections (220) for in-plane ϕ rotations of 0° (red) and 180° (black), (a) raw data and (b) normalized to a nominal value for the GaAs substrate peak.

For a symmetric reflection ψ is zero, provided that there is no wafer miscut but the value of Ω is found from half of the difference between $\Delta\omega^+$ and $\Delta\omega^-$,

$$\Omega = (\Delta\omega^- - \Delta\omega^+)/2 \ , \tag{3.2}$$

while $\Delta\omega$ is the average of the angular differences,

$$\Delta\omega = (\Delta\omega^- + \Delta\omega^+)/2 \ . \tag{3.3}$$

For an asymmetric reflection, the tilt is a combination of $\Delta\psi \pm \Omega$ also given by half of the amplitude of the difference,

$$(\Delta\psi \pm \Omega) = (\Delta\omega^- - \Delta\omega^+)/2 \ . \tag{3.4}$$

The value of Ω is found from $(\Delta\omega^- - \Delta\omega^+)/2$, for the symmetric reflection, as $\Delta\psi$ is zero for the symmetric reflection. The perpendicular and parallel x-ray strains (mismatch), $\varepsilon_\perp$ and $\varepsilon_{//}$, respectively are then given by [52-54],

$$\varepsilon_{\perp} = \frac{\sin(\theta_B)\cos(\psi)}{\sin(\theta_B + \Delta\omega)\cos(\psi + \Delta\psi)} - 1 \tag{3.5}$$

and

$$\varepsilon_{\parallel} = \frac{\sin(\theta_B)\sin(\psi)}{\sin(\theta_B + \Delta\omega)\sin(\psi + \Delta\psi)} - 1, \tag{3.6}$$

where θ_B is the Bragg angle of the diffracting planes. $\varepsilon_{\perp}$ and $\varepsilon_{/\!/}$ x-ray strains are related to the *d*-spacing of the film epilayer and the substrate as follows [52-54]:

$$\epsilon_{\perp} = \left(\frac{\mathrm{d}_{epi} - d_{sub}}{d_{sub}}\right)_{\perp} \tag{3.7}$$

$$\epsilon_{/\!/} = \left(\frac{\mathrm{d}_{epi} - d_{sub}}{d_{sub}}\right)_{/\!/} \tag{3.8}$$

$$\gamma = \left(\frac{\mathrm{a}_{/\!/} - a_f}{a_{\perp} - a_f}\right) \tag{3.9}$$

$$a_f = \left(\frac{\mathrm{a}_{/\!/} - \gamma a_{\perp}}{1 - \gamma}\right), \tag{3.10}$$

where γ is the film Poisson ratio. $a_{/\!/}$, $a_{\perp}$, and a_f are the lattice constants in-plane and out of plane with respect to the substrate, of the relaxed film, respectively. $a_{/\!/}$ and $a_{\perp}$ can be calculated from the *d*-spacing and a_f is calculated assuming $\gamma = 0.29$ for Fe [55].

A measurement called a pole-figure was used to determine whether the Fe film was aligned with the sample in-plane rotation. This was obtained by measuring a ϕ scan, the rotation of the sample about the surface normal, for various values of χ (tilt of the sample above or below the diffraction plane). A 360° ϕ rotation with χ tilt ranging from 0° to $\pm$ 75° was collected to obtain a 2D plot of the intensity with respect to ϕ and χ axes. These plots contain either spots or rings (depending on the crystal structure) representing the stereographic projections of the indexed crystallographic planes in the desired reflection plane. Bragg peaks corresponding to GaAs (422) and Fe (211) crystal planes were used for pole figures.

Reciprocal space maps were obtained from collections of individual ω - 2θ rocking curves measured at a range of ω positions (angles in real space) to measure the strain and mosaic spread of the film crystal structure. Mosaic spread can be calculated from the 2-D (ω - θ) map as full width of a contour at half of the maximum intensity. An analyzer crystal with an effective aperture of 12 arc sec was used to collect diffracted signals for both pole figures and reciprocal space maps.

3.1.3. Fe on bulk wafers (Sample B1)

3.1.3.1. Data from low resolution XRD

Fig. 3.4 shows plots of x-ray intensity (counts/s) versus detector position (2θ) from θ - 2θ scans for Fe on sample B1 (sample no: B1-1 to B1-8) grown at (a) RT and (b) 50 °C, respectively, as a function of growth time, *t*. In each case, a Fe (011) peak at an angle 44.6° is clearly visible along with the GaAs (220) at 45.3°. For both growth temperatures, the intensity of the Fe peak increases with growth time consistent with increasing Fe thickness. The GaAs peak intensity is varying with the sample but not due to thickness of the Fe film; rather this is likely the effect of a macroscopic tilt of the sample with respect to the incident X-ray beam from the poorly controlled mounting capability (sample alignment is not provided with a goniometer) on the Siemens diffractometer. Multiple scans from the same sample were obtained as a function of the rotation of the sample on the holder. This would change the substrate and film peak intensities meaning that the tilt from mounting varied, perhaps by as much as 1 to 2 degrees. Comparing the data for the two growth temperatures, it is clear that the Fe peak intensity is larger for 50 °C, probably the result of better crystallinity, since the GaAs peak is uniform. When the sample is well aligned the extra peak near 43.2° is due to GaAs diffraction of residual K_β x-rays.

The $P(2\theta)$ of the most intense GaAs (220) peak (45.6°) is found to be 0.027° which represents the instrument limited peak width (also checked with a polycrystalline Si reference). The FWHM and the intensity of the Fe (110) peaks in Fig. 3.4 (a) and (b) are included in Table 3.1. Thus, based on equation 3.1 and correcting these FWHM for

instrumental broadening (0.027°), Fe grain sizes have been estimated and listed in Table 3.1. The Fe (011) x-ray peak intensity (*I*) from Fig. 3.4 versus growth time for each growth temperature is shown in Fig. 3.5. As mentioned, the peak amplitude for Fe (110) grown at 50 °C is much larger (10x) compared to the similar growth time at RT, indicating greater thickness and or better crystallinity with increasing growth temperature. The intensity increases for the 50 °C grown films with growth time while those of the RT films levels off to a smaller maximum intensity. Fig. 3.6 shows a plot of grain size from Table 3.1 versus growth time for each growth temperature. Grain sizes increase slowly with growth time for both RT and 50 °C growth temperatures. Grain sizes for 50 °C growths are double that of RT films (49 nm versus 28 nm). Fig. 3.5 is consistent with a better epitaxy.

Table 3.1 Summary of results from low resolution XRD of Fe on Bulk wafers, listing sample no; growth temperature, *T*; growth time, *t*; Peak intensity, *I*; FWHM of the Fe peaks, *P*(2θ); grain size, *L*.

Sample no	*T* °C	*t* s	*I* *C/s* ± 10%	*P*(2θ) degree ± 0.01	*L* nm ± 1%
B1-2	22	14	1155	0.40	24
B1-3	"	30	1874	0.35	28
B1-4	"	67	1972	0.38	25
B1-5	"	90	1874	0.30	33
B1-6	50	34	3098	0.18	49
B1-7	"	86	9530	0.20	52
B1-8	"	90	21611	0.21	59

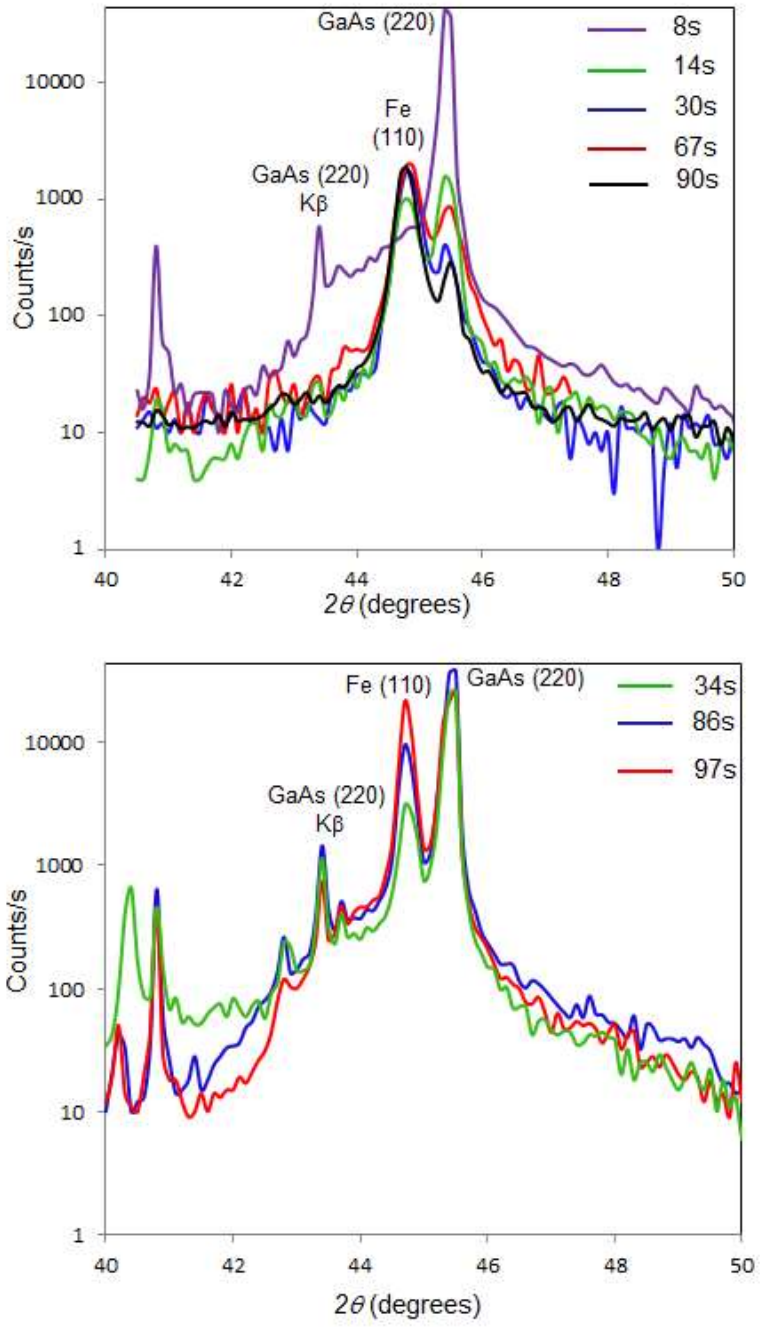

Fig. 3.4. Intensity of x-ray θ - 2θ plots of Fe on sample B1 grown at (a) RT for durations from 8 s to 67 s, and (b) at 50°C for durations of 34 s, 86 s, and 97 s. The intensity of the Fe (110) peak increases with increasing growth time as expected for films increasing in thickness with time.

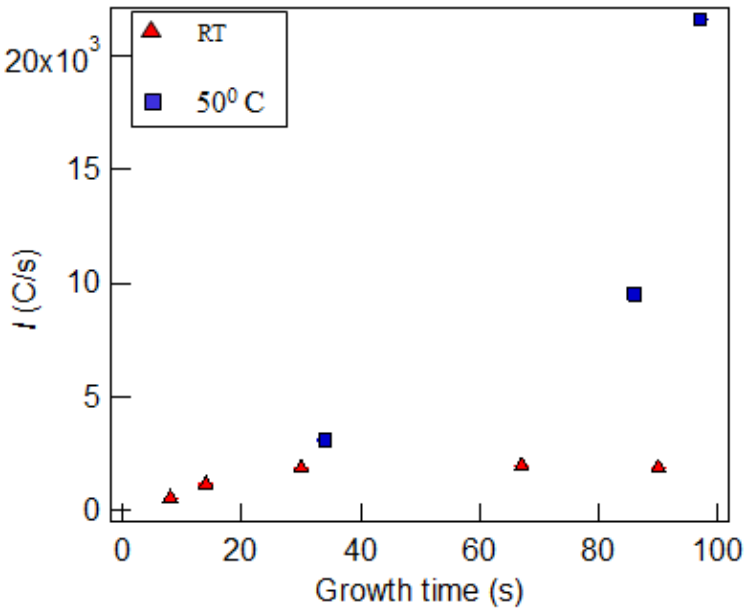

Fig. 3.5. Plots of Fe (110) XRD peak intensity (*I*) as a function of growth time for Fe grown on sample B1 at RT (red triangles) and at 50 °C (blue squares), respectively.

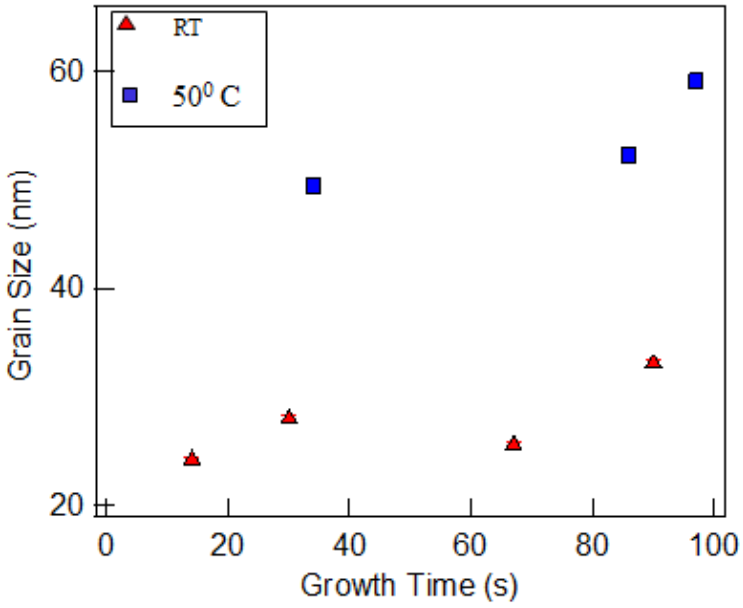

Fig. 3.6. Plots of grain size as a function of growth time for Fe grown on sample B1 at RT (red triangles) and at 50 °C (blue squares), respectively.

3.1.3.2. Data from high resolution XRD

For Fe/GaAs (110) samples, symmetric and asymmetric Bragg diffraction peaks (220)/(110) and (422)/(211) occur with the Bragg angles (θ_B), listed in Table 3.2 (page 45). Fig. 3.7 shows x-ray diffraction intensity versus sample rotation angle, ω, from ω - 2θ rocking curves for the samples B1-5 and B1-7 (similar growth time) grown at (a) and (b) RT and (c) and (d) 50 °C for symmetric [GaAs(220)/Fe(110)] and asymmetric [GaAs(422)/Fe(211)] reflections. Table 3.2 lists results for the parameters θ_B, ψ, $\Delta\omega$ and $\Delta\psi$ based on the analysis of these ω - 2θ rocking curves. Table 3.3 lists the calculated values for x-ray strain (mismatch) and lattice constants along in-plane and out-of-plane directions based on the data in Table 3.2 and equations 3.5 – 3.10. The in-plane lattice constants for both cases are higher than that of the out-of-plane lattice constant by small fractions, 0.02 *Å* and 0.01 *Å* at RT and 50 °C, respectively which indicates a small tensile stress in the film. It is also evident from the x-ray strains along in-plane and out of plane directions compared to the value of the lattice mismatch of 1.4 % between GaAs and Fe. Also, the relaxed lattice constants 2.857 ± 0.001 *Å* and 2.864 ± 0.001 *Å* (RT and 50 °C respectively) are slightly lower than that of the bulk lattice constant of Fe (a_{Fe_bulk} = 2.866 *Å* [56]) meaning the Fe film is not 100 % pure. The FWHM (rocking curves) and estimated grain sizes calculated using the Scherrer equation 3.1 are 0.3° and 30 nm for Fe film grown at RT (B1-5) and 0.1° and 93 nm for the 50 °C sample (B1-7), smaller than the total thickness of the films (RT 245 nm). If the Fe had been perfect single crystal the expected FWHM would be 0.002° much smaller than these [51].

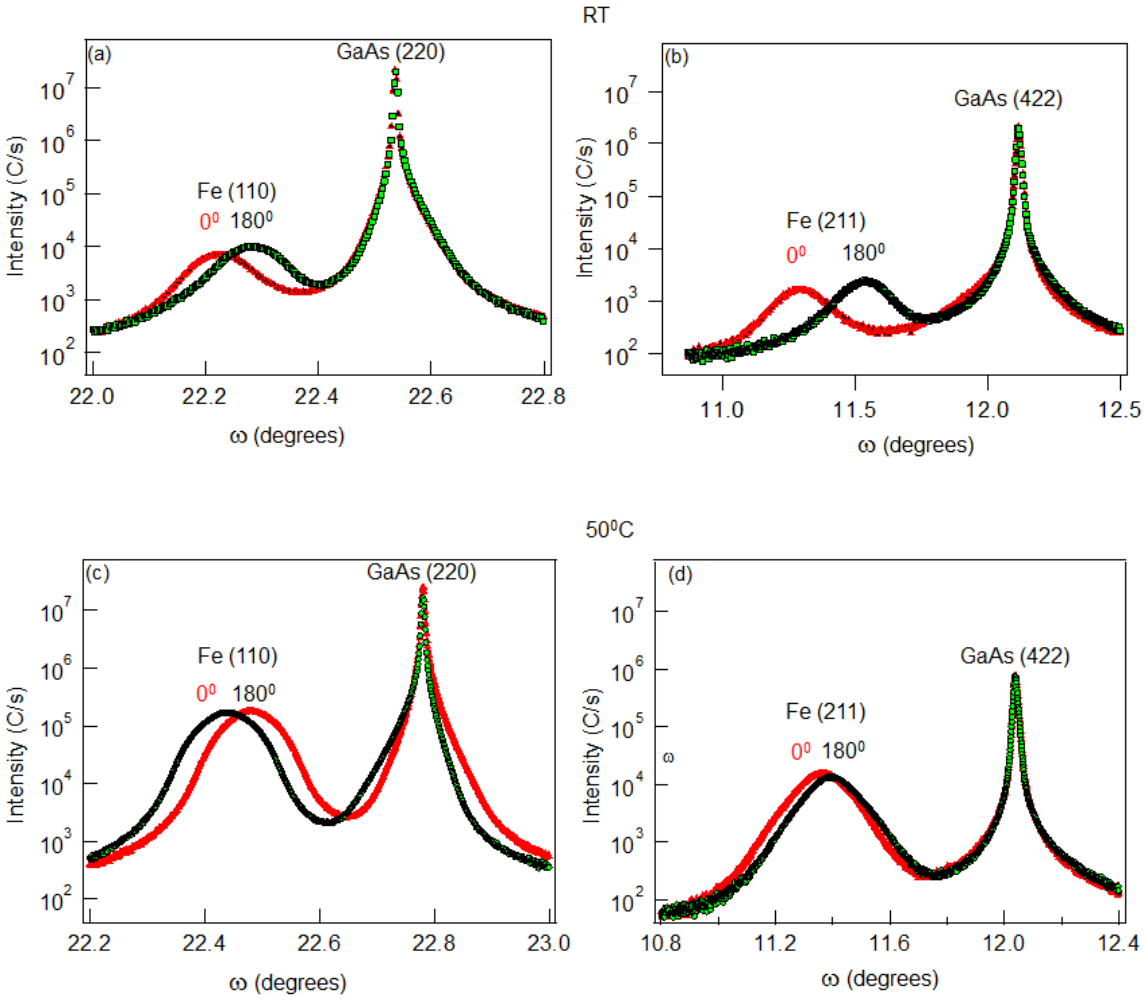

Fig. 3.7. ω - 2θ rocking curves for samples B1-5 and B1-7 grown at (a) and (b) RT and (c) and (d) 50 °C, respectively, for symmetric [GaAs(220)/Fe(110)] and asymmetric [GaAs(422)/Fe(211)] reflections.

Table 3.2. Results from the analysis of the rocking curves of Fig. 3.6 for samples B1-5 and B1-7. Listed are the growth temperatures, *T*; the scattering planes, *hkl*; the theoretical Bragg angle, θ_B; tilt in *hkl* planes with respect to the substrate surface (110), ψ; average of the raw differences in substrate and epilayer peak positions, $\Delta\omega$; tilt in the film with respect to the substrate due to strain, $\Delta\psi$; macroscopic planar tilt of the film with respect to the substrate, Ω; is obtained from the value of $\Delta\psi \pm \Omega$ for symmetric reflections, since $\Delta\psi$ is zero.

T °C ± 1	*hkl*	θ_B degrees	ψ degrees	$\Delta\omega$ degrees ± 0.001	$\Delta\psi \pm \Omega$ degrees ± 0.001	$\Delta\psi$ degrees ± 0.001
22	(220)	22.7531	0	0.317	0.029	0
″	(422)	41.9563	30	0.775	+0.115	0.086
50	(220)	22.6885	0	0.320	0.020	0
″	(422)	41.9329	30	0.702	-0.018	0.038

Table 3.3. In-plane and out-of-plane Fe film strain, $\varepsilon_{\parallel}$ and $\varepsilon_{\perp}$, and lattice constants, $a_{\parallel}$ and $a_{\perp}$, and resulting relaxed film lattice constant, a_f, for samples B1-5 and B1-7 at growth temperatures RT and 50 °C.

Growth Temp	X-ray strain		Lattice constants		
°C			Å		
	In-plane	Out-of-plane	In-plane	Out-of-plane	Relaxed
T ± 1	$\varepsilon_{\parallel}$ ± 0.0002	$\varepsilon_{\perp}$ ± 0.0002	$a_{\parallel}$ ± 0.001	$a_{\perp}$ ± 0.001	a_f ± 0.001
22	0.0165	0.0129	2.873	2.853	2.857
50	0.0152	0.0132	2.869	2.863	2.864

Fig. 3.8 shows a 2-D angular map for symmetric reflections of GaAs (220)/Fe (110) planes for samples B1-5 and B1-7 grown at (a) RT and (b) 50 °C, respectively (contour map in ω - θ coordinate). A horizontal displacement between Fe (110) and GaAs (220) peaks (in the ω axis) would be due to a macroscopic tilt between the Fe (110) and GaAs (220) planes for RT and 50 °C samples. These plots show no such tilt to within the accuracy, ± 0.02° of the map. The horizontal displacement (in the θ axis), 0.5° for the symmetric map is due to the difference in the d-spacing of GaAs (220) and Fe (110) planes. Fig. 3.9 shows contour plots for asymmetric reflections of GaAs

(422)/Fe (211) planes for samples B1-5 and B1-7 grown at (a) RT and (b) 50 °C, respectively displaying GaAs (422) and Fe (211) peaks in the reciprocal space coordinate system for Fe/GaAs(110). Inset shows the 2-D angular plots (in ω - θ coordinate) for these reciprocal space maps. The asymmetric map shows a strong increase in the Fe peak intensity with increasing growth temperature meaning better Fe crystalline structure for higher growth temperature, consistent with the single rocking curves shown earlier. Parallel and perpendicular mismatch calculated from the maps for (422)/(211) reflection (reciprocal coordinate) shown in Fig. 3.9 (a) and (b) are 1.3% and 1.2% for RT and 1.6% and 1.2% for 50 °C samples, respectively. Angle between GaAs (422) and Fe (211) plane, 0.07° for RT and 0.09° for 50 °C samples, is observed from asymmetric map (horizontal black lines passing through GaAs (422) and Fe (211) peaks in the angular plot). A larger mosaic spread (0.8°) is obtained for the RT sample compared to the 50 °C sample (0.2°).

Fig. 3.10 shows pole figures for GaAs (422) and Fe (211) reflections for sample B1-3 and B1-7 grown at RT ((a) and (b)) and 50 °C ((c) and (d)), respectively. Fig. 3.10 (a) and (c) shows the expected peaks with a 2-fold symmetry axis for a single crystalline GaAs (110) substrate. Fig. 3.10 (b) and (d) also show a similar spot pattern indicating a significant degree of epitaxial Fe (110) alignment. The scattered diffraction intensities especially towards higher χ angles in the RT film indicates random polycrystalline growth. At higher growth temperatures, Fig. 3.10 (d), there is less random diffraction except for a strong ring at a χ of 62°. This is a signature of a textured set of polycrystalline structures which must all have a tilt of 62° - θ_B (422) = 20.5° with respect to the substrate normal. The intensity and FWHM (in-plane and azimuthal) for GaAs and Fe peaks are listed in Table 3.4.

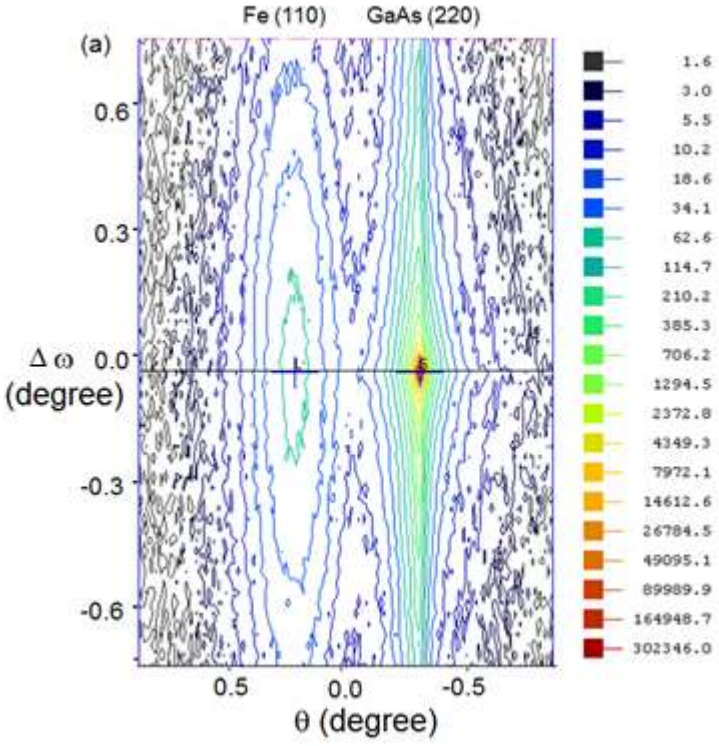
Fe (110) GaAs (220)
(a)
0.6
0.3
Δ ω 0.0
(degree)
-0.3
-0.6
0.5
0.0
-0.5
θ (degree)
1.6
3.0
5.5
10.2
18.6
34.1
62.6
114.7
210.2
385.3
706.2
1294.5
2372.8
4349.3
7972.1
14612.6
26784.5
49095.1
89989.9
164948.7
302346.0

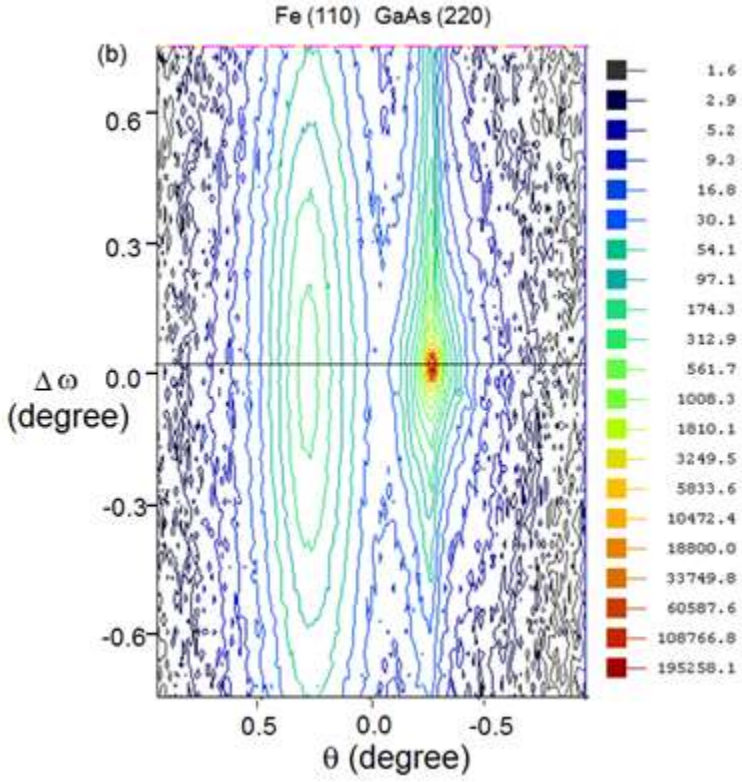
Fe (110) GaAs (220)
(b)
0.6
0.3
Δ ω 0.0
(degree)
-0.3
-0.6
0.5
0.0
-0.5
θ (degree)
1.6
2.9
5.2
9.3
16.8
30.1
54.1
97.1
174.3
312.9
561.7
1008.3
1810.1
3249.5
5833.6
10472.4
18800.0
33749.8
60587.6
108766.8
195258.1

Fig. 3.8. Symmetric contour plots for samples B1-5 and B1-7 showing GaAs (220) and Fe (110) peaks with no vertical separation of the substrate and film peaks for both (a) RT and (b) 50 °C sample, respectively. Horizontal separation is 0.5° occurring from the difference in d-spacing for Fe (110) and GaAs (220) planes for these ED samples.

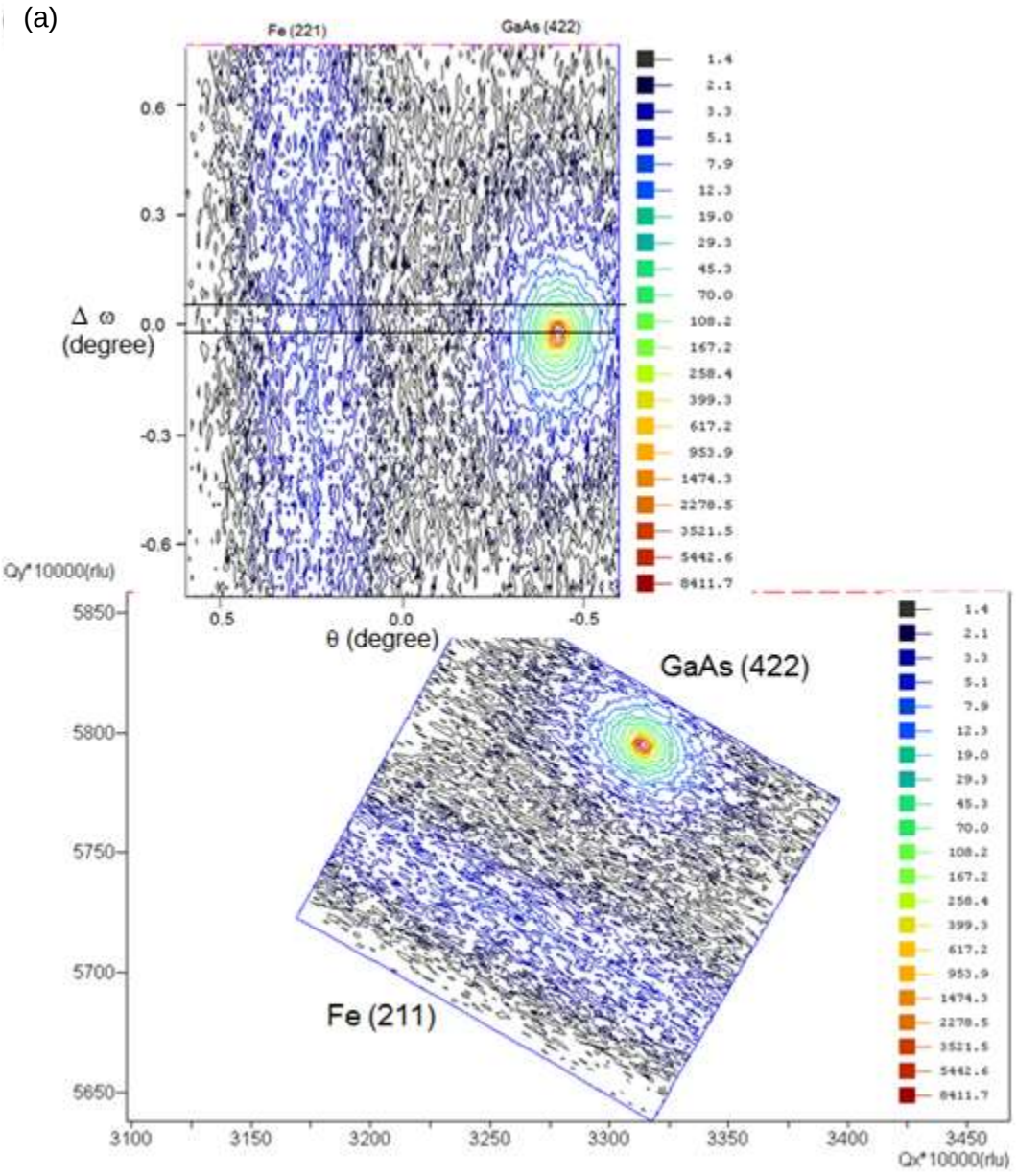

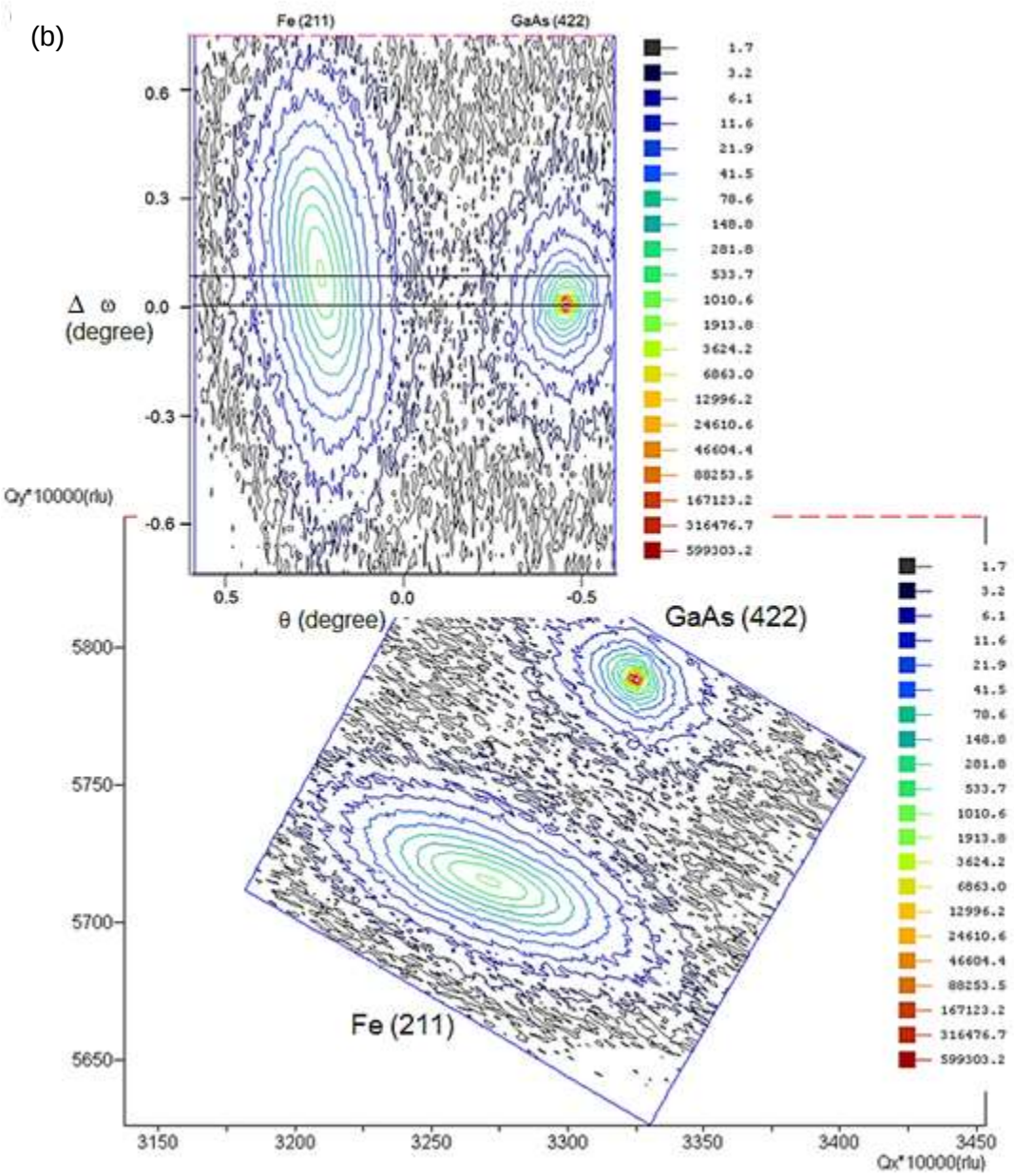

Fig. 3.9. Reciprocal space maps for samples B1-5 and B1-7 at (a) RT and (b) 50 °C respectively, for asymmetric reflections of (211)/(422). Inset shows the 2-D angular plots in ω-θ coordinate of these reciprocal space maps. Angular distances between GaAs (422) and Fe (112) peaks along ω axis are shown by black lines. The Fe peak intensities for the 50 °C sample in (b) 46,000 counts/s is higher compared to the RT data in (a) 700 counts/s, indicating better Fe crystallinity. Mosaic spreads calculated from these maps are 0.8° and 0.2° for RT and 50 °C growths, respectively.

Table 3.4. Peak intensities and FWHM from the (422)/(211) pole figure scans for samples B1-5 and B1-7 grown at RT and 50 °C respectively, shown in Fig. 3.9.

Sample no	Material	Intensity	FWHM	
			ϕ	χ
		C/s	degrees	degrees
B1-5	GaAs	1.4 M	0.3	2.8
	Fe	760	3.5	3.3
B1-7	GaAs	1.4 M	0.3	2.8
	Fe	18 K	2.7	3.3

The intensity of the Fe peaks from pole figures is larger for higher growth temperature similar to the results observed using rocking curves and in reciprocal space maps again indicating Fe crystallinity improved at higher growth temperature.

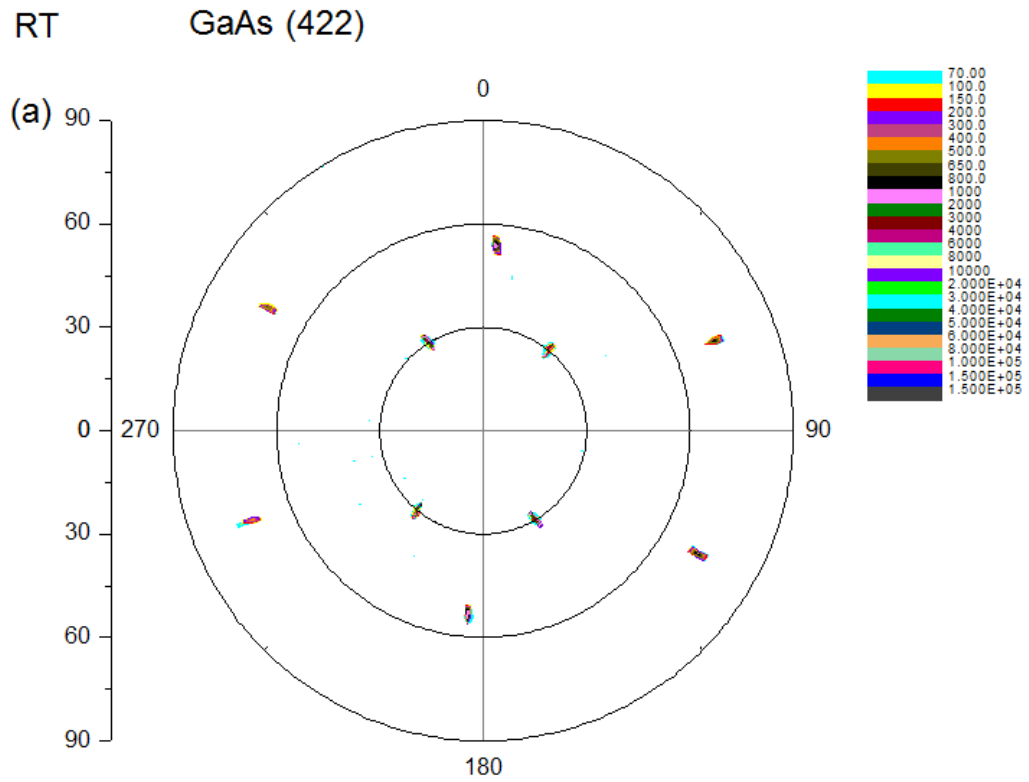
RT
GaAs (422)
(a)
0
90
60
30
0
270
90
30
60
90
180
70.00
100.0
150.0
200.0
300.0
400.0
500.0
650.0
800.0
1000
2000
3000
4000
6000
8000
10000
2.000E+04
3.000E+04
4.000E+04
5.000E+04
6.000E+04
8.000E+04
1.000E+05
1.500E+05
1.500E+05

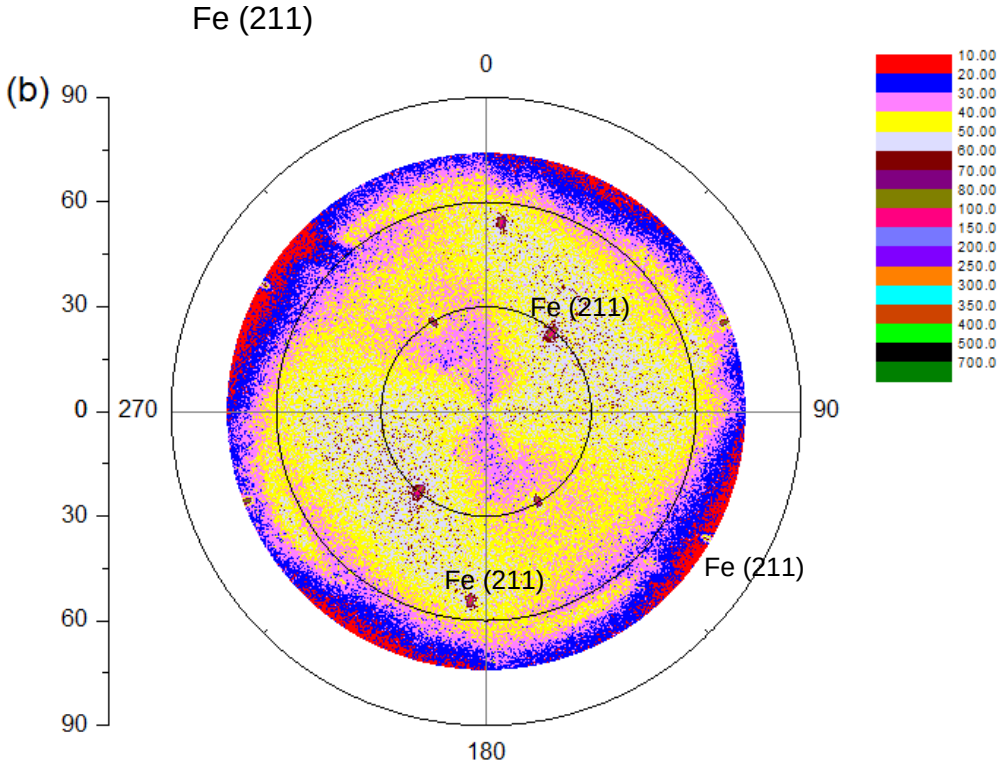
Fe (211)
(b)
0
90
60
30
0
270
90
30
60
90
180
Fe (211)
Fe (211)
Fe (211)
10.00
20.00
30.00
40.00
50.00
60.00
70.00
80.00
100.0
150.0
200.0
250.0
300.0
350.0
400.0
500.0
700.0

50°C GaAs (422)

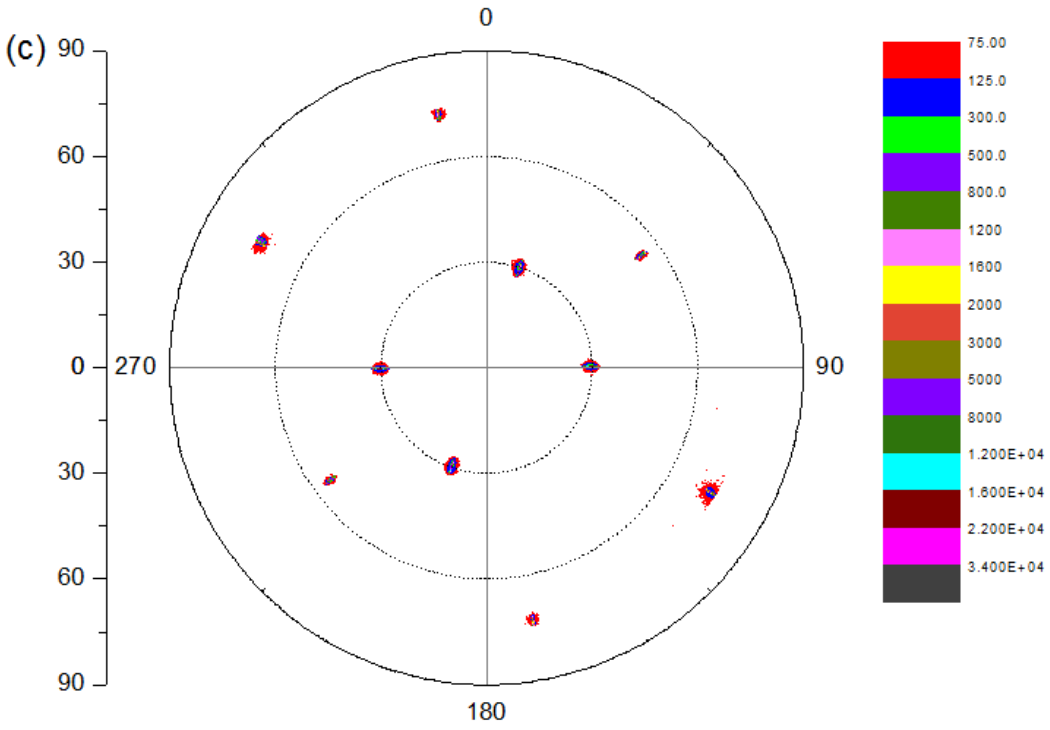

Fe (211)

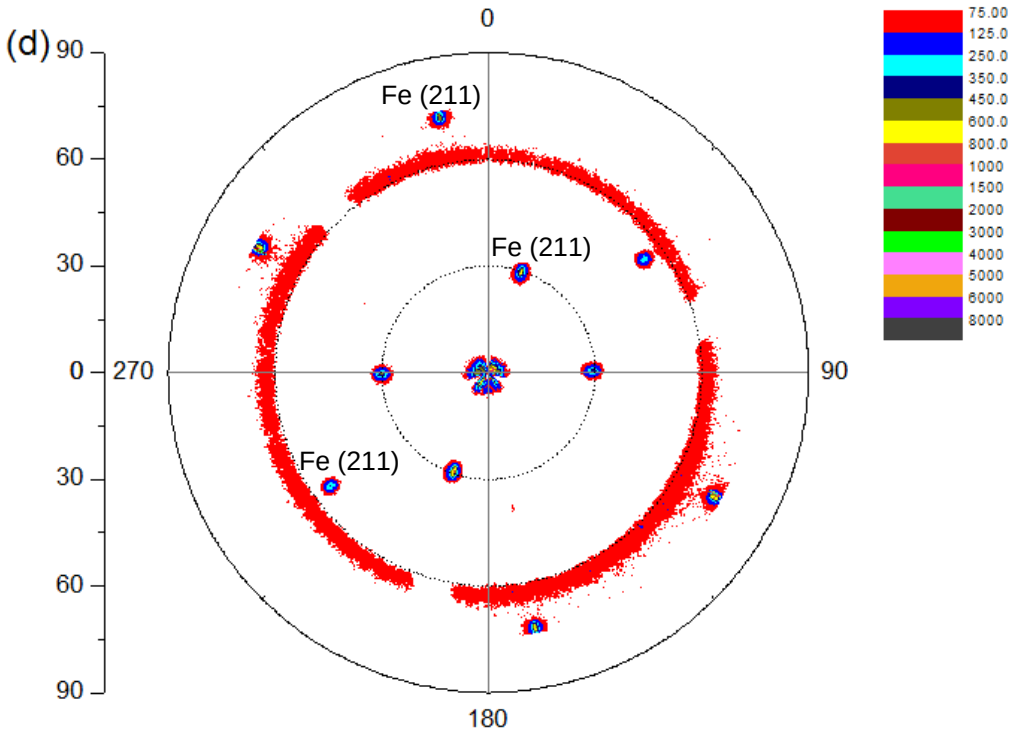

Fig. 3.10. Results from GaAs (422) / Fe (211) pole figures for samples B1-5 and B1-7 at RT ((a) and (b)) and for 50 °C ((c) and (d)), respectively.

3.1.3.3. Summary of XRD results from Fe on bulk GaAs

The perfection in the Fe epitaxial growth on bulk GaAs substrate improved at the higher growth temperature, as indicated by both the low and high resolution XRD diffraction intensity and peak widths. The grain size increased for higher growth temperature. Pole figures confirmed that the in-plane crystallographic directions of the Fe are parallel to the identical directions of the GaAs. The two materials are aligned in-plane. The HRXRD analysis of the film strain found in-plane tensile strain of 0.7%. Parallel mismatch is found larger than the perpendicular mismatch for both growth temperatures also indicating that the film stress is tensile. However, the relaxed film lattice constant was found to be smaller than pure Fe by 0.1% - 0.3% indicating that impurities were present in the Fe film [57]. A larger mosaic spread in the XRD peaks was observed for the RT sample than 50 °C which is consistent with the smaller grain size and poorer crystallinity for this growth temperature.

3.1.4. Fe on epi-GaAs (Sample E1)

3.1.4.1. Data from low resolution XRD

To optimise the Fe crystallinity for growth on epi-GaAs samples (sample no; E1-1 – E1-5), J was varied between 0.05 mA/mm^2 to 0.20 mA/mm^2 based on the known optimal current density for bulk wafer ED (0.1 mA/mm^2). Above 0.2 mA/mm^2 Fe films did not adhere to epi-GaAs samples and at lower currents than 0.05 mA/mm^2 no deposition was observed. Fig. 3.11 shows x-ray θ - 2θ plots as a function of J for Fe on epi-GaAs (001) sample (samples: E1-1 to E1-5) measuring from only a deposition area of 2 × 6 mm^2. The lower intensity of GaAs and Fe peaks is due to the sample misalignment in the Siemens diffractometer. The samples were also smaller and could not be rotated to improve the beam alignment. The GaAs (004) peaks are now resolved due to Cu $K_{\alpha 1}$ and $K_{\alpha 2}$ wavelengths being at a higher angle than for the (220) peaks from the GaAs

(110) previous data. The Fe (002) peak is visible perhaps only for the current density of 0.15 mA//mm^2. The expected difference in 2θ between the GaAs (004) and the possible Fe (002) peaks of 0.8° is seen.

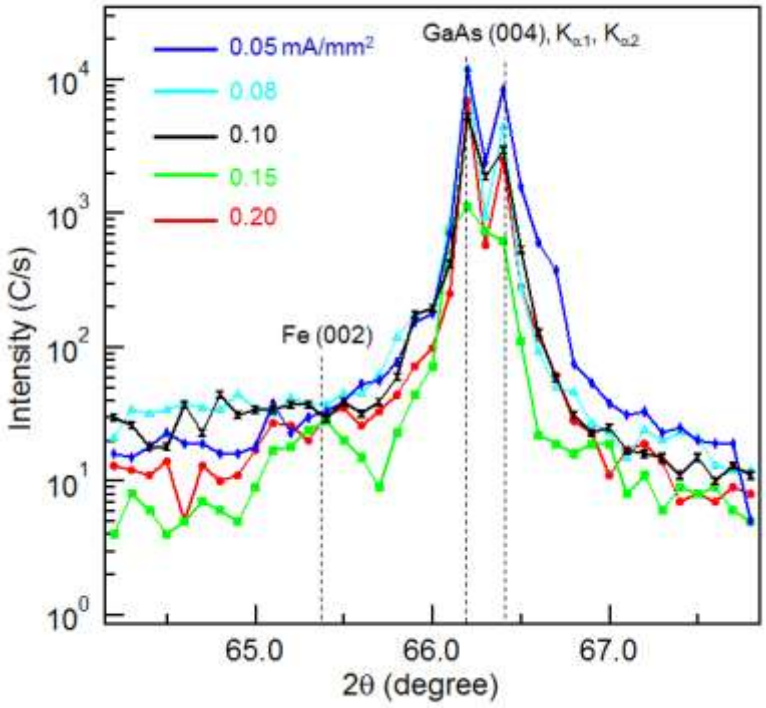

Fig. 3.11. Results from θ - 2θ plots (Seimens diffractometer) showing x-ray diffraction intensity versus detector position 2θ as a function of deposition current density *J* for samples E1-1 - E1-5 with an area of 2 × 6 mm^2. Fe (002) peak is possibly detected only for the current density of 0.15 mA/mm^2 at the expected 2θ position, 65.4° and the GaAs peak at 66.2°.

Fig. 3.12 displays an SEM image of a Fe on epi-GaAs (sample E1-4) showing the typical microstructure everywhere except near the edges (1-2 microns away) for an applied current density of 0.15 mA/mm^2. Similar microstructure was observed for 3 other samples made in the same way. Possible in-plane textures are along in-plane (110) and $(1\bar{1}0)$ crystallographic directions shown by arrows. Average feature size in the image is 150 nm.

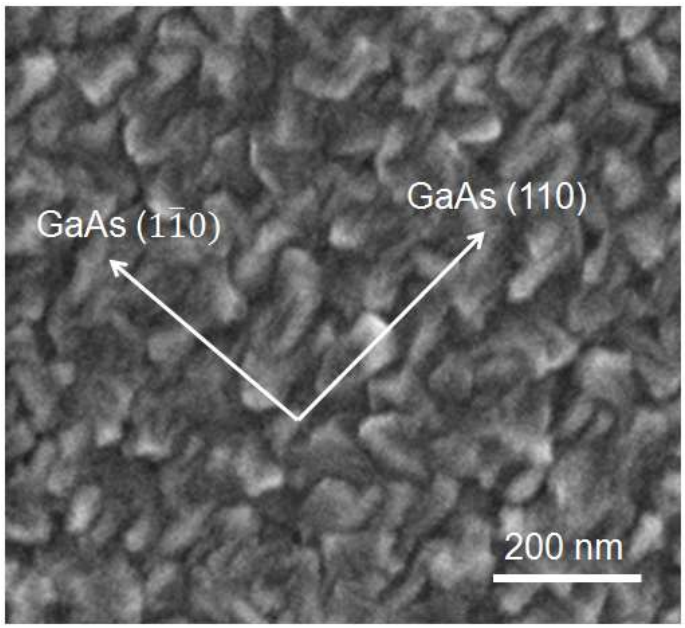

Fig. 3.12. SEM image of sample E1-4, grown with current density of 0.15 mA/mm^2 showing feature size of 150 nm. A possible in-plane textures are along in-plane (110) and (1$\bar{1}$0) directions (arrows).

3.1.4.2. Data from High resolution XRD

High resolution XRD rocking curves were obtained to further analyse the crystallinity of Fe film of samples E1-3 - E1-5. Fig. 3.13 shows results from ω - 2θ plots for samples E1-3 - E1-5 grown with *J* of 0.2 (blue), 0.15 (red) and 0.1 mA/mm^2 (black). From these plots the amplitude of the Fe peak doubles from a maximum 80 Counts/s for *J* of 0.20 mA/mm^2 to 160 Counts/s for 0.015 mA/mm^2.

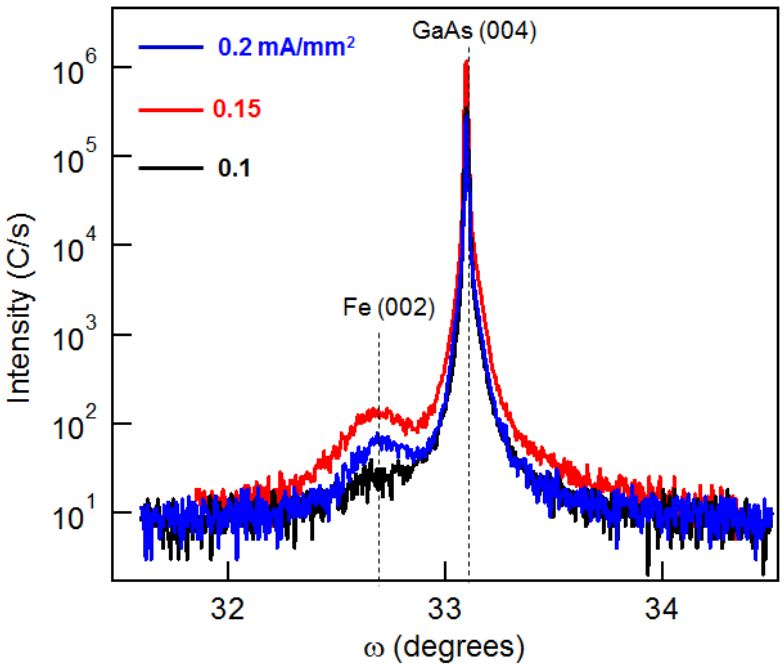

Fig. 3.13. x-ray ω - 2θ rocking curves for samples E1-3 - E1-5 grown using a current density of 0.2 mA/mm^2 (blue), 0.15 mA/mm^2 (red) and 0.1 mA/mm^2 (black).

Fig. 3.14 shows x-ray ω - 2θ rocking curves (two axis) for sample E1-7 for (a) symmetric GaAs (400) and (b) asymmetric GaAs (422) reflections, respectively, showing Fe (200) and Fe (211) peaks. The FWHM of the Fe peaks are both 0.4° for (002) and (211) peaks, which are comparable to their counterparts from growth on bulk GaAs (110) sample (30 nm for sample B1-5) giving also a comparable grain size estimate of 25 nm (equation 3.1). Although the growth time is less for the sample E1-7 than the sample B1-5. The GaAs peaks are broadened in the tail regions suggesting a second peak shifted from the main peak by 0.02° and 0.03° for symmetric and asymmetric reflections, respectively. The origin of the broadening is unknown and is not investigated in this thesis.

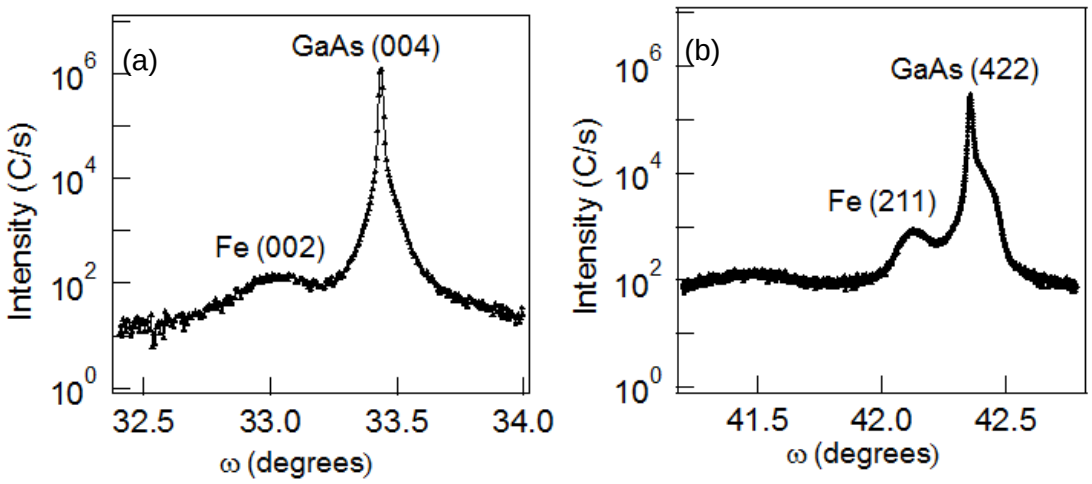

Fig. 3.14. x-ray ω - 2θ rocking curves for sample E1-7 grown at RT (a) symmetric reflection (400)/(200) and (b) asymmetric reflection (422)/(211) showing peaks for Fe (200) and Fe (211) with intensities (C/s) 125 and 765, respectively.

Fig. 3.15 displays x-ray pole figures Intensity versus ϕ and χ $(0 \text{ to } 60°)$ for sample E1-7 for GaAs (422) and Fe (211) planes each showing four peaks 90° apart at a χ of 35°. There are also scattered spots indicating polycrystalline grains in the Fe pole figure with an interesting preference for one half of the ϕ rotation. The in-plane texture of the substrate and the film are well aligned. The FWHM of the peaks is larger than from rocking curves since the width is affected by mosaic tilts as well as grain size. The data from pole figure measurements is summarized in Table 3.5.

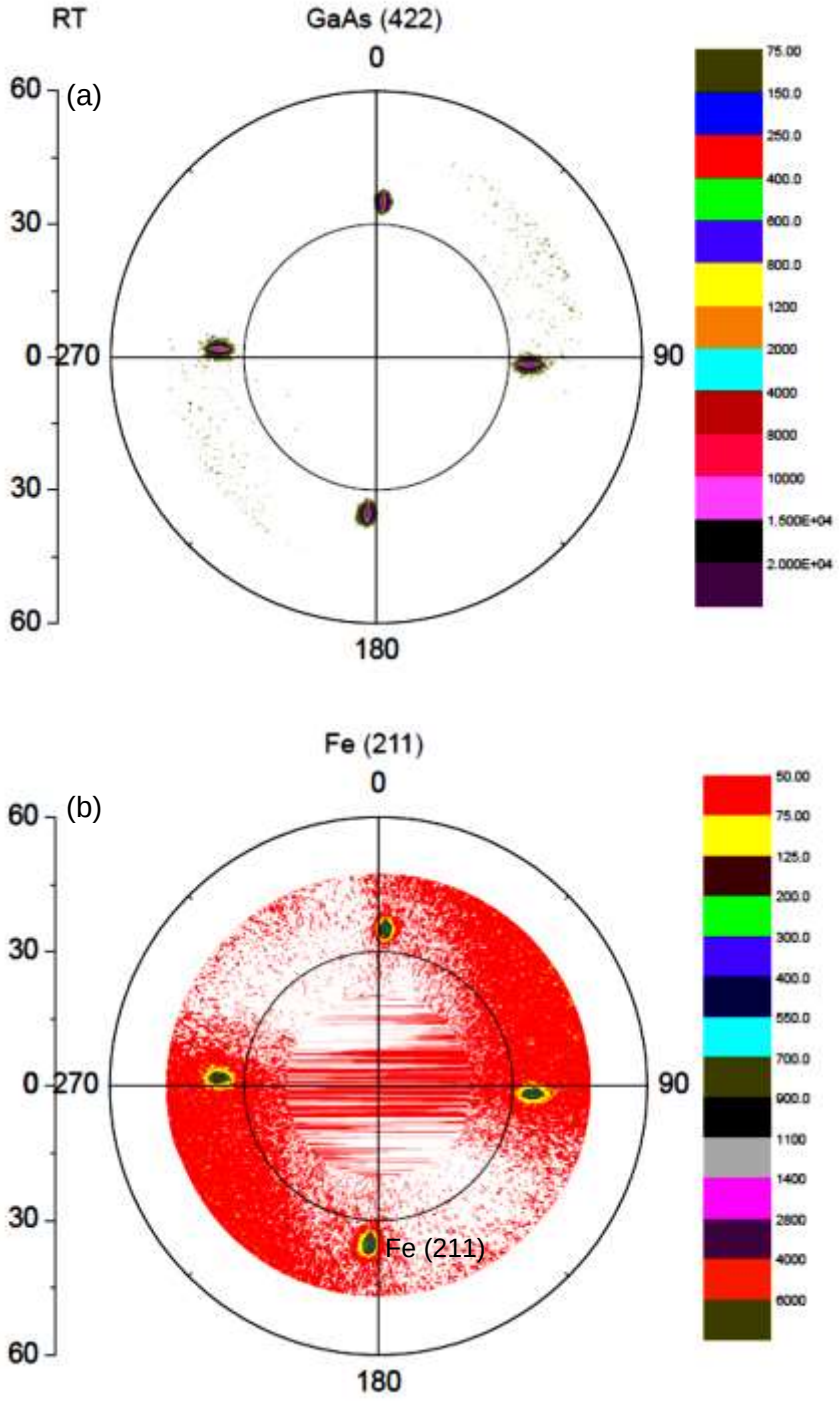

Fig. 3.15. Results from pole figures obtained for E1-7 for (a) GaAs (422) and (b) Fe (211) each displaying 4 reflections at a χ of 35°, 90° apart confirming in-plane Fe texture aligned with the GaAs sample.

Table 3.5. Intensities and FWHM of peaks from pole figures for samples E1-7 and B1-5 at RT:

Sample no	Material	Intensity C/s	FWHM In-plane degrees	FWHM Azimuth degrees
E1-7	GaAs	1.2 M	0.6	3.0
	Fe	765	4.3	4.4
B1-5	GaAs	1.4 M	0.3	2.8
	Fe	760	3.5	3.3

3.1.4.3. Summary of XRD results from Fe on epi-GaAs

As mentioned earlier in Chapter 2 the larger resistance of the epi-GaAs sample resulted in a larger over-potential gradient along the length of the sample during the ED process requiring optimization of the current density for similar Fe growth as on a bulk GaAs sample. The optimal current density (0.15 mA/mm^2) was found to be 50% greater than that used for bulk GaAs sample deposition.

The crystal structure of the Fe films on epi-GaAs samples was a combination of strong epitaxial texture with polycrystalline grains, similar to the structure of films grown on bulk GaAs samples. The vertical grain sizes obtained from HRXRD for E1-7 (25 nm) were comparable to the growth of sample B1-5 at RT (30 nm). A larger mosaic spread was observed in these ED films meaning that there was more misalignment in the

coalescence of these films than in Fe on bulk GaAs samples. However, the Fe peak intensities are comparable for both cases.

3.2. TEM Analysis

To analyse microstructure (e.g. misorientation, grain size, and defects) of the Fe/GaAs sample and the interface, transmission electron microscopy (TEM) imaging was carried out using either a field-emission gun (FEG) (Tecnai G2) or a thermal source (Hitachi 8100) transmission electron microscope. Both operated at a voltage of 200 keV with a minimum point resolution of 2.3 *Å*. Two sample orientations (B1 and E1), plan-view and cross-section, were investigated.

Plan-view samples were prepared by polishing the GaAs side down to 50 µm, gluing it onto a Cu grid with epoxy, and finally Ar ion-milling (4.2 kV and 3.7 mA) at a low angle (10-15 degrees) at liquid nitrogen (LN) temperatures, until a hole was obtained. Cross-sectional samples were first cleaved into two equal pieces which were then sandwiched with a thin epoxy layer in between and cured. The sandwich was cut into 1 mm slices with a diamond saw, then polished on both sides, glued and cured onto a Cu grid, and Ar ion-milled as above until a central hole was obtained.

At lower magnifications, bright field (BF) and dark field (DF) images were obtained depending on the choice of the transmitted beam using an objective lens aperture size of 20 µm. Corresponding diffraction patterns were obtained using selected area diffraction (SAD) apertures of 50 µm or 100 µm. For both types of images, a limiting aperture restricts which transmitted electrons contribute to the final image. In BF the forward scattered beam (center spot) produces the image while in DF any diffracted beam is chosen. Both amplitude and phase contrast are seen in BF and DF images. Amplitude contrast is a combination of diffraction and mass-thickness variations. Any real sample will have areas with non-uniform thickness. Thicker regions of the sample cause more electron scattering than thin regions. As a result, fewer electrons reach the image plane and therefore thicker areas appear darker in BF and brighter in DF images [58]. The contrast of a DF image is complimentary to BF image. In a DF image, brighter

areas occur where the electron beam is diffracted the most by a specific (*hkl*) plane. For phase contrast one needs at least two beams to interfere with each other, evident when fringes are visible (examples are, lattice and Moiré fringes).

A lattice image of a thin sample is created via phase contrast from interfering electron beams at high magnification close to a low index direction perpendicular to the interface. If the sample is periodic with atomic spacings less than the point resolution of the TEM (0.23 nm), the images shows fringes with symmetry that is a representation of the periodicity of the crystal structure at the interface of the epitaxial film and the substrate.

Moiré fringes form when two beams from two different crystal lattices interfere. There exist two distinct types of Moiré fringes or mixtures of them depending on the alignment of the lattices with respect to each other, translational (perfectly aligned but two different lattice constants) and rotational (same lattice constant but rotated) [58]. Moiré fringes are a magnified display of the crystal structure of the sample layers and are distorted by any deviation in the lattice (defects, dislocations and lattice mismatch strain in the sample). Moiré fringe spacing can be calculated as follows [59],

$$D_{fringe\ spacing} = \frac{d_1 d_2}{((d_1 - d_2)^2 + d_1 d_2 \beta^2)^{\frac{1}{2}}} \quad , \tag{3.11}$$

where d_1 and d_2 are the lattice *d*-spacing of the materials and β is the angle between the two lattices. Experimental fringe spacings can be used to confirm strain or rotation in a film with respect to the substrate.

Defocussing the objective lens could expose grain boundaries in the crystal lattice of the specimen. Fig. 3.16 illustrates image formation at different focussing conditions (under-focus, focus and over-focus). Bright and dark fringes form around any edge (e.g. voids or grain boundaries) due to phase contrast (Fresnel contrast) in the under and over focus conditions of the lens, respectively. There is minimum contrast for a single crystalline material at a perfect focus condition.

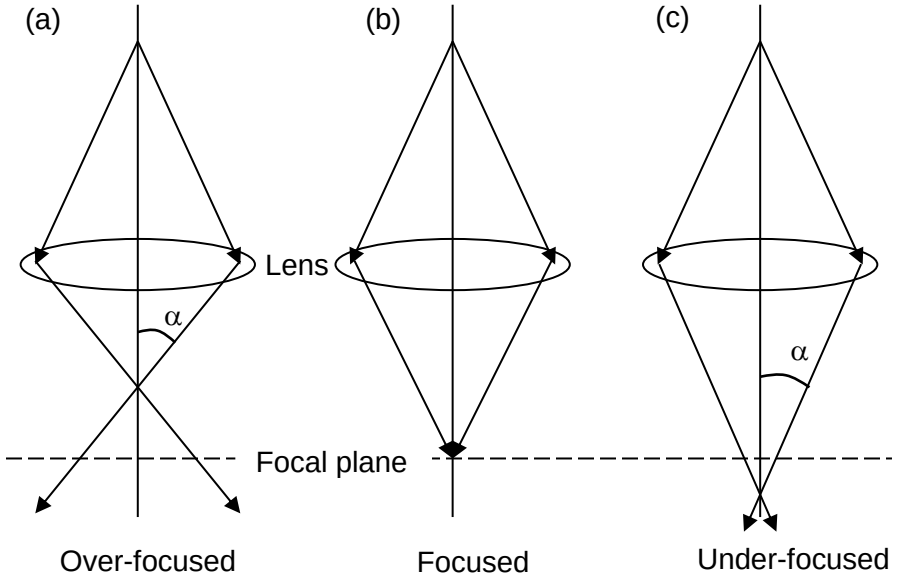

Fig. 3.16. Schematic diagram of the electron beam through the objective lens while forming an image with (a) over-focused (b) focused and (c) under-focused conditions.

To determine the crystal structure and the orientation of the film with respect to the substrate one needs to obtain electron diffraction patterns from the film as well as the substrate. The diffraction pattern from epitaxial-Fe/GaAs is a superposition of both Fe and GaAs TEM diffraction patterns. It is easy to differentiate between the spots from Fe and GaAs knowing the individual diffraction patterns for the film and the substrate. Fig. 3.17 shows diffraction patterns from (a) GaAs (110) and (b) GaAs (100) substrates where the electron beam direction is out of the page approximately perpendicular to the (110) and (100) substrate surfaces, respectively. If these were exactly down the pole the intensity of the spots would be perfectly symmetric. In these patterns the intensity of the diffraction spots shows a preference for one direction over another, indicating that the substrate was slightly tilted away from exactly parallel [110] and [100], respectively. Fig. 3.17 also shows the schematics of diffraction spots from an epitaxial (c) bcc Fe (110) and (d) Fe (100) lattice structure (same beam directions).

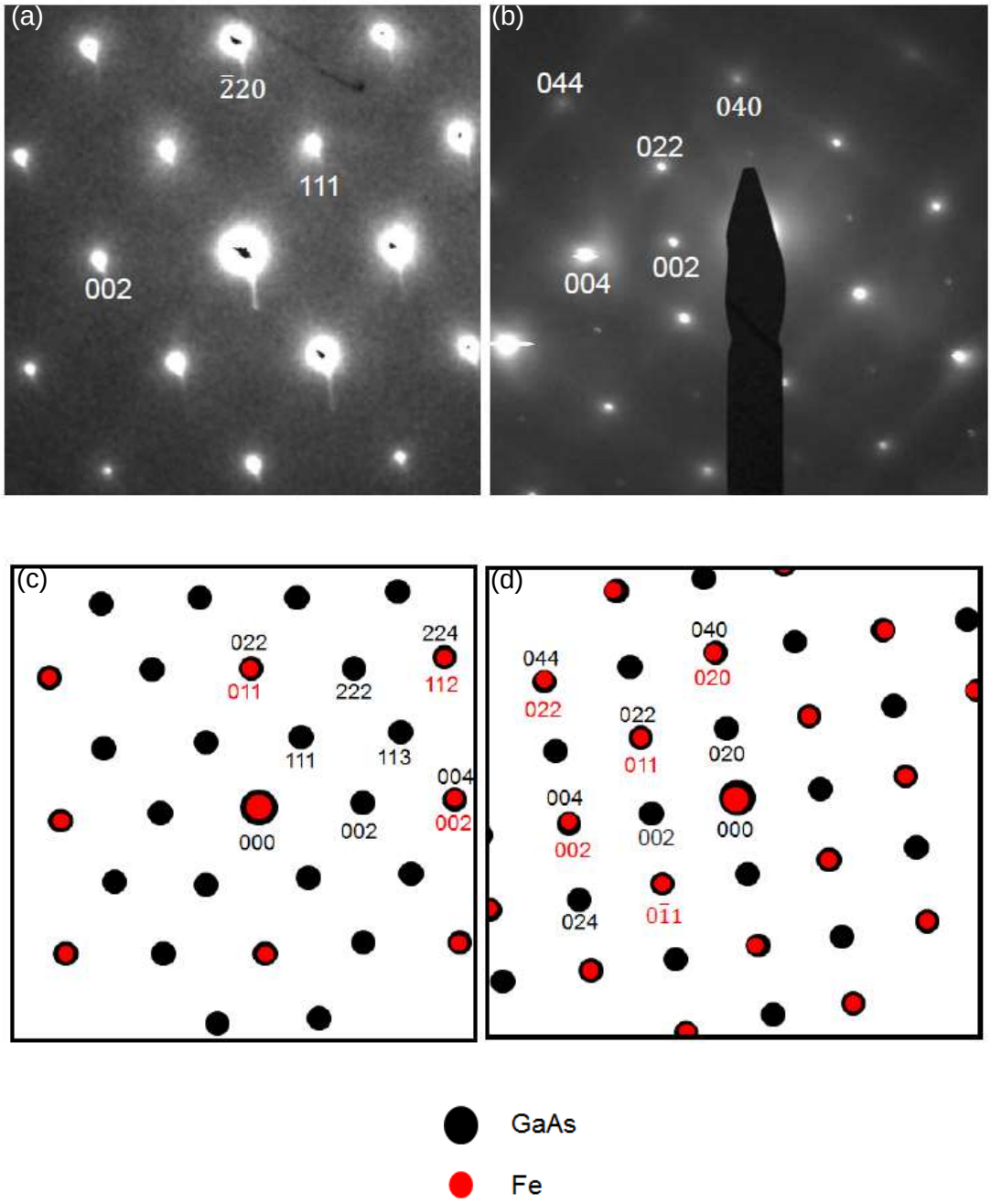

Fig. 3.17. Indexed diffraction patterns in planview for GaAs (a) (110) and (b) (100). Schematic bcc Fe diffraction patterns (c) (110) and (d) (100) overlaid epitaxially with GaAs.

3.2.1. Fe on bulk wafers (sample B1)

Fig. 3.18 shows BF planview TEM images of samples B1-5 and B1-7 grown at (a) RT and (b) 50°C, respectively. The visible fringes have spacings that range from 11 nm to 12 nm consistent with Moiré type fringes from overlapping lattices. If this was perfectly single crystalline Fe on GaAs, there should be one set of straight fringes for each set of planes. Spacing would be given by equation 3.11. Any deviations in the fringe pattern (such as the areas circled) are due to variations in orientation or lattice constant such as would be the case from small angle grain boundaries formed during coalescence of individual ED Fe crystalline islands. The corresponding selected area diffraction patterns confirm that the majority of the Fe has the (011) crystallographic orientation of the film and the substrate. There is evidence of polycrystalline grains as seen by the rings aligned with the spot spacings in the SAD. Moiré fringe spacings for the RT and 50°C samples calculated from the images are 11 nm $\pm$ 2 nm and 12 nm $\pm$ 2 nm, respectively. These values are smaller compared to the theoretical value of 13.9 nm calculated using equation 3.11 assuming the Fe film is unstrained with β = 0, d_1 = 2.027 Å [56], and d_2 = 1.998 Å [60].

Defocussing the objective lens can expose grain boundaries in the crystal lattice of the specimen. Fig. 3.19 shows over-focused and under-focused BF images of sample B1-2 grown at RT, 100 nm thick, displaying black and white lines (dark and bright fringes, features show better when images are viewed on a computer screen) where grain boundaries are occurring from coalescence of imperfectly aligned Fe nuclei during deposition. The fringes are parallel to both the in-plane <011> and <002> crystallographic directions as indicated by the corresponding diffraction pattern. The average feature size, outlined by black and white fringes in fig. 3.19 (a) and (b), is 40 nm $\pm$ 10 nm, which is in good agreement with the grain size estimated from XRD data using the Scherrer equation 3.1.

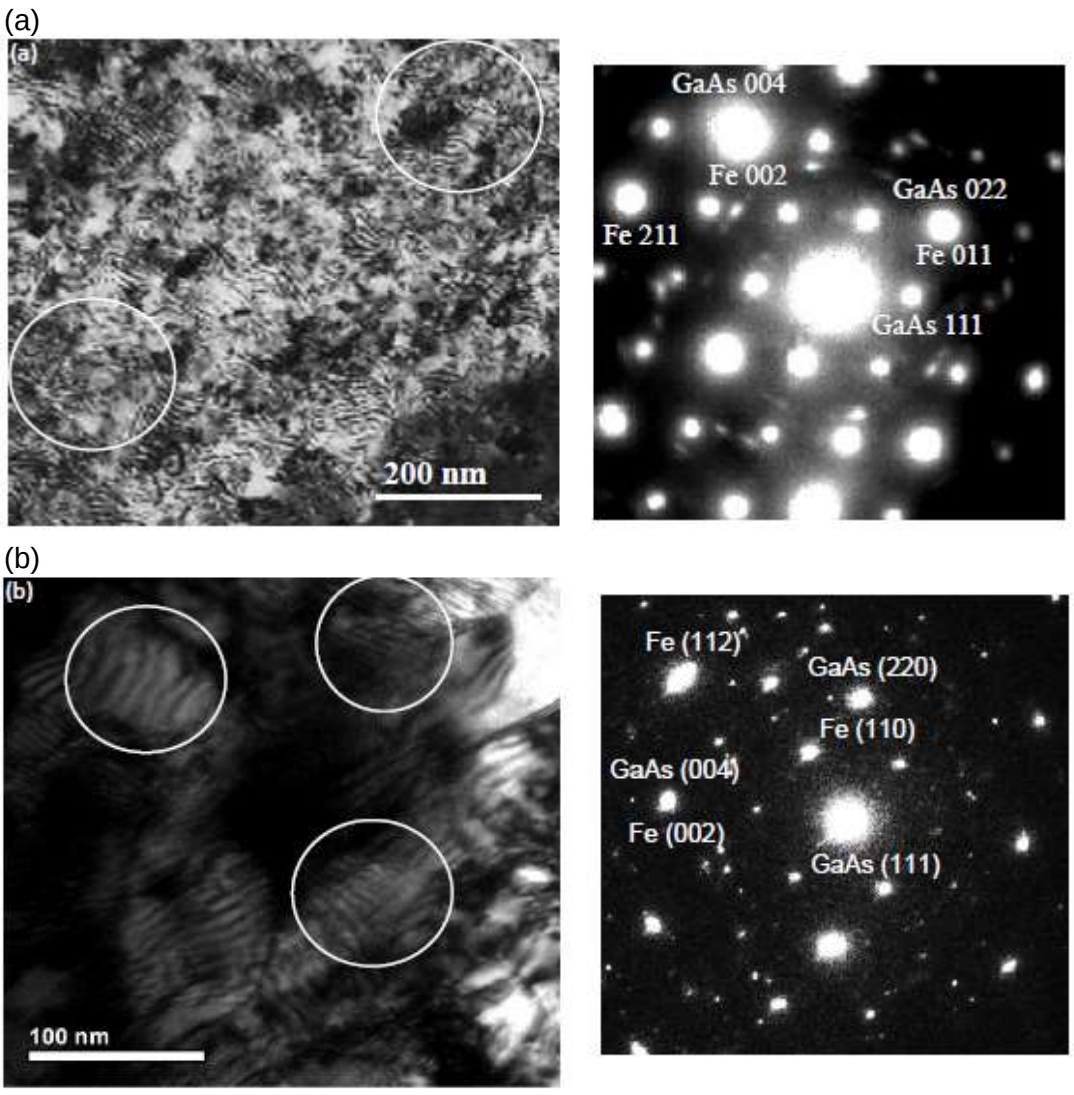

Fig. 3.18. BF planview TEM images of samples B1-5 and B1-7 grown at (a) RT and (b) 50°C, respectively. The corresponding SAD pattern confirms an epitaxial arrangement of the Fe on the GaAs showing a pattern consistent with the electron beam parallel to the [110] growth direction (down pole). The circled regions show Moiré fringes in more than one direction as expected.

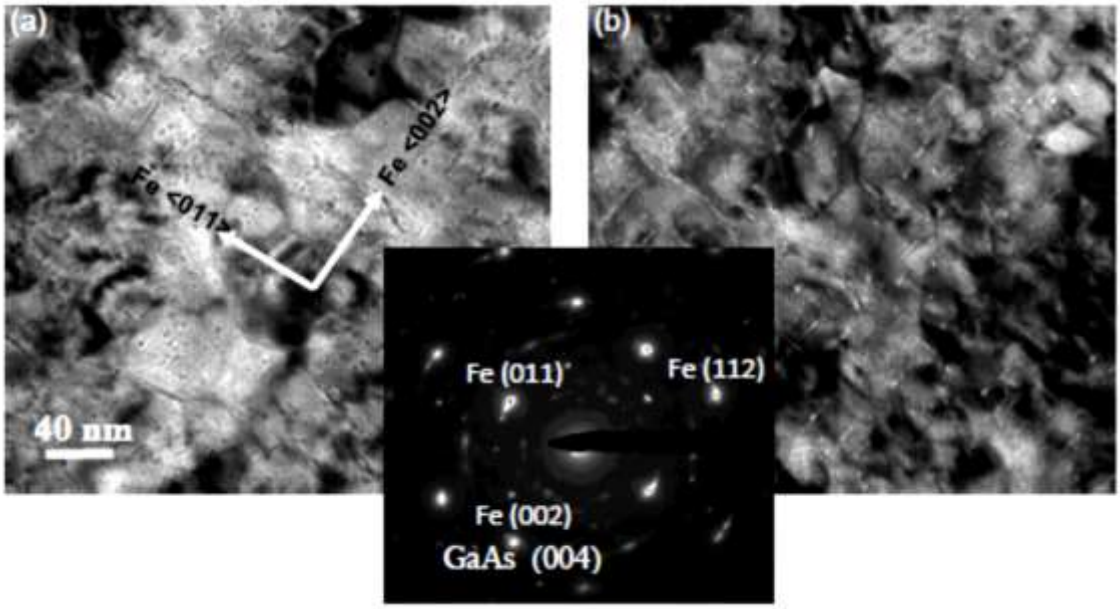

Fig. 3.19. BF images of sample B1-2 obtained at (a) over-focused (b) under-focused condition showing black and white fringes, respectively. These fringes are signatures of defects likely grain boundaries, which occur due to the imperfect coalescence of individual Fe nuclei during the ED process. The diffraction pattern obtained indicates that the crystallographic direction of the grain boundaries is predominantly parallel to <002> and <110> directions. Overall, the contrast in the image occurs from thickness variations as well as diffraction contrast from small misalignments in the grains. The average size of the grain-like features is 40 nm $\pm$ 10 nm.

Tilting the sample away from the substrate zone axis towards strong diffraction from one set of planes, can reveal planar defects. Fig. 3.20 (a) shows a low magnification BF image of sample B1-2 grown at RT (14 s), obtained near the (110) pole (beam is perpendicular to the (110) substrate plane). Stacking faults (planar defects) are barely visible at this magnification and tilt. The image shows a uniform background contrast with dark lines. The dark lines are called “bend contours” (a signature of crystallinity), as they originate from low-angle curvature in the thin single crystalline part of the Fe film. Bend contours move when the sample is tilted and therefore can be easily distinguished from fixed defects. Fig. 3.20 (b) displays a magnified BF image of the circled area in Fig. 3.20 (a) with a sample tilt of 2 degrees about a [111] axis. Stacking faults become more clearly visible parallel to <111> directions. Fig. 3.20 (c)

shows even greater visibility of stacking faults acquired by a second tilt of 7° around the in-plane <110> axis from the same area as in Fig. 3.20 (b). The fact that the stacking faults are all aligned in the same direction is another strong indication that all of the 40 nm grains are part of the same very well oriented film.

(a)

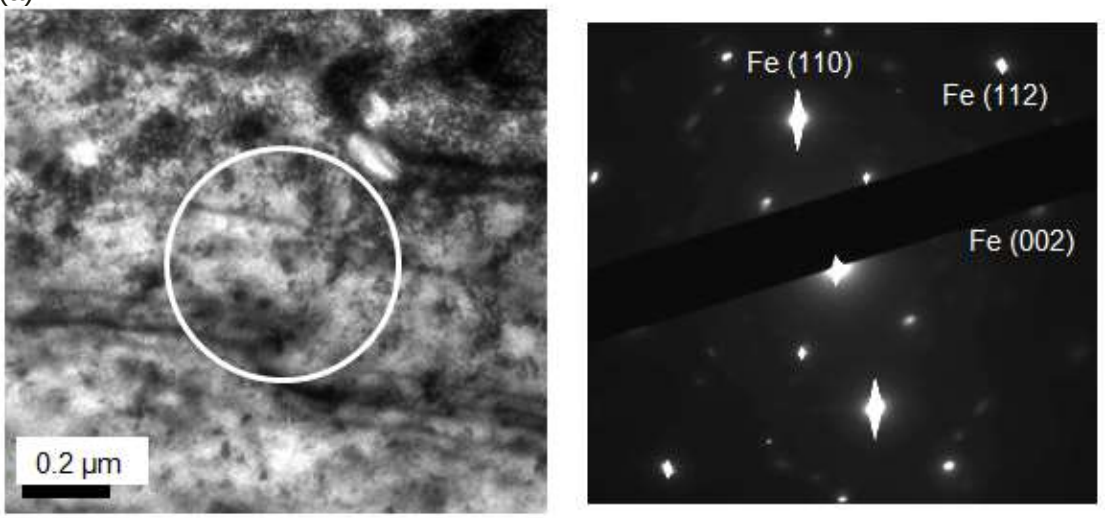

(b)

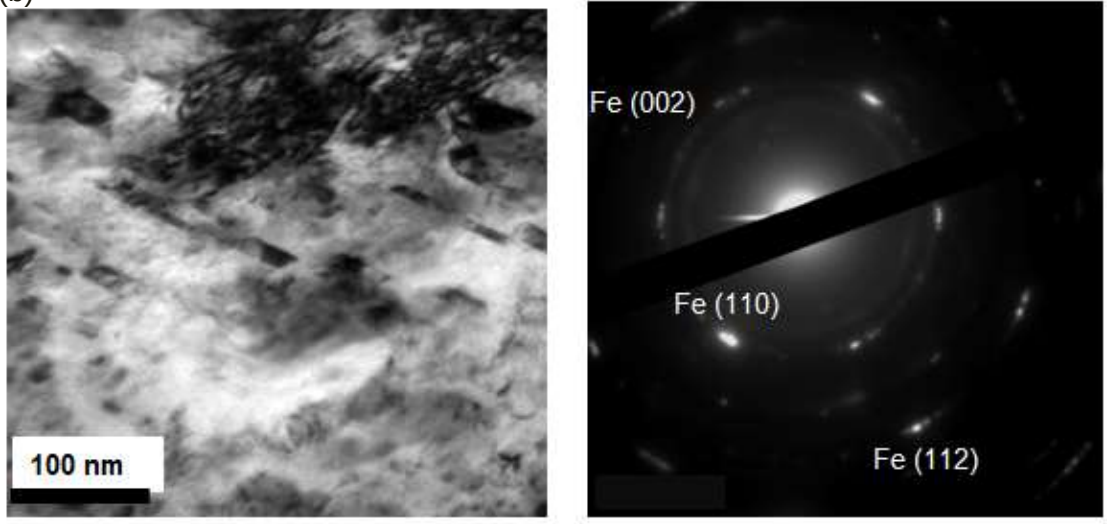

(c)

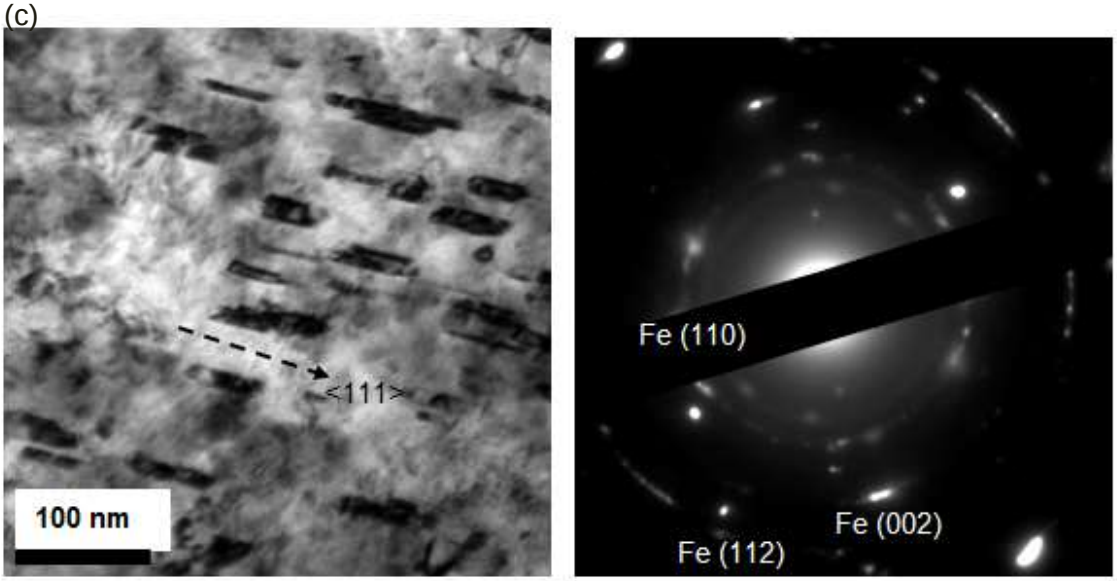

Fig. 3.20. TEM BF images of sample B1-2 grown at RT (14 s, 100 nm thick) and corresponding SAD patterns. This is the same material as shown in Fig. 3.19 with 40 nm grain sizes. The image in (a) has a non-uniform contrast with dark spots and lines (bend contours). The SAD pattern confirms the crystallographic orientation of the Fe to be along <110>. In (b) a BF image was obtained by magnifying the circled area in (a) and tilting the sample 2° about the in-plane <111> axis. Stacking faults along <111> are beginning to be visible. (c) More stacking faults in the same area along <111> are visible when the sample is tilted a total of 7° about the in-plane <110> axis.

Fig. 3.21 displays TEM images from planview of sample B1-7 grown at 50 °C (86 s) (a) (022) BF and SAD pattern, (b) (002) ring DF (c) (112) ring DF. The uniform contrast areas in the BF image confirm that the Fe film is (011) oriented. The dark lines correspond to Fe grain boundaries. We estimate an average grain size of at least 120 nm $\pm$ 10 nm, which is comparable to the value calculated from HRXRD measurements using Scherrer equation 3.1 (93 nm). The Fe (002) ring and (112) ring DF images show uniform dark contrast except for isolated bright regions where the strong diffraction into the DF spots had occurred.

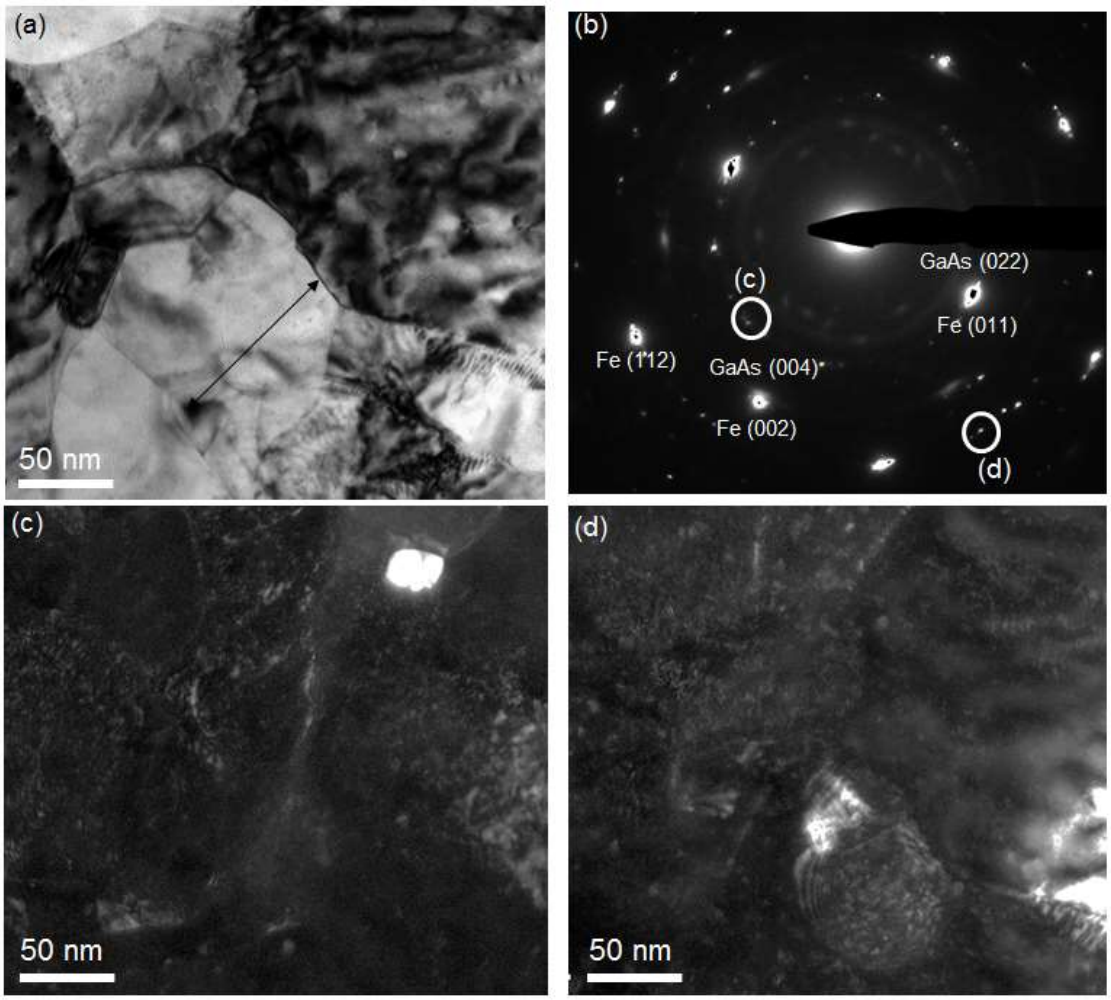

Fig. 3.21. TEM planview of the sample B1-7 grown at 50 °C showing (a) BF image and corresponding SAD pattern and (b) and (c) DF images obtained from indicated spots in SAD (b) Fe (002) ring and (c) Fe (112) ring.

Fig. 3.22 BF image of sample B1-1 grown at RT for 8 s. The image shows Moiré fringes confirming that both Fe and GaAs single crystal is present in those regions. The corresponding SAD pattern shows the Fe alignment with the GaAs sample (Fringes forming due to Fe and GaAs crystals are perpendicular to the <110> direction). The thickness of the Fe film at this growth time is 60 nm. A continuous Fe film is obtained at the growth time of 14 s with a thickness of 100 nm (shown in Fig. 3.19).

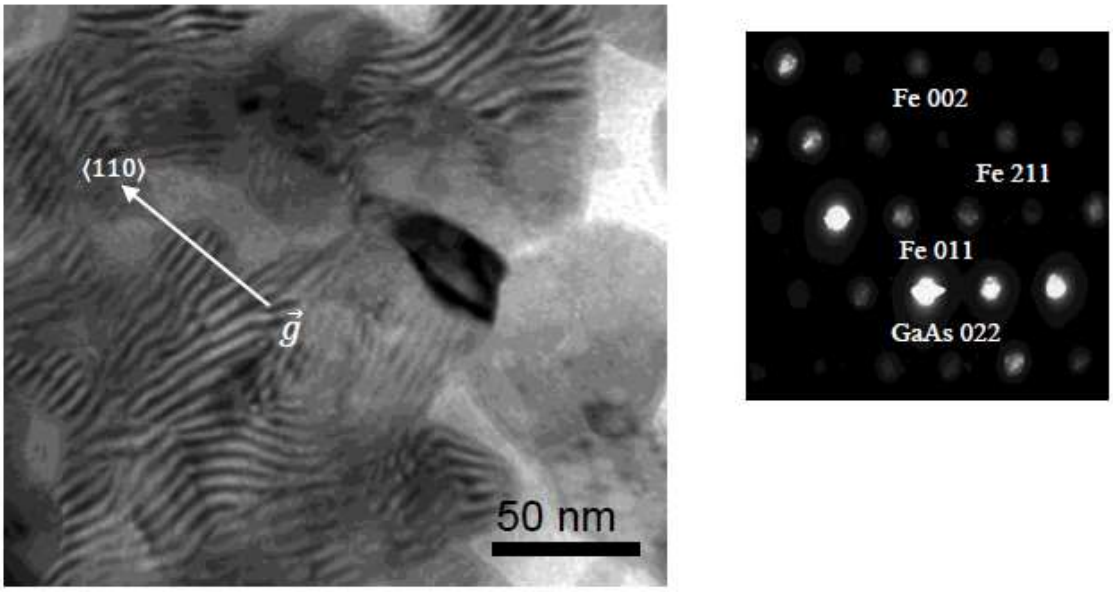

Fig. 3.22. BF image and corresponding SAD pattern of sample B1-1 at RT (8 s) showing a discontinuous Fe film (average thickness 60 nm). Moiré fringes are visible perpendicular to the strong 2-beam diffraction condition (1$\underline{1}$0), confirming the presence of both Fe and GaAs.

Fig. 3.23 shows cross-section (111) TEM images of sample B1-2 and B1-7 grown at RT and 50°C (a) and (c), respectively. The left images are low magnification BF images with corresponding SAD patterns while the right images (b) and (d) are high magnification lattice images from the areas indicated by the red circles in (a) and (c). The contrast and dark lines in the low magnification BF images are due to thickness variation and bend contours. Areas with circular bend contours (marked in blue rectangles) indicate strain in the Fe film. The Fe/GaAs (110) interface in the lattice images in Fig. 3.23 (b) and (d) for both samples is marked by arrows. Fringes in the lattice image are due to GaAs (220) and Fe (110) planes (lattice spacing 2.0 *Å*). The fringe width between the white arrows is 2.0 *Å*. The lattice image in (b) is exactly at the (111) pole whereas for (d) it is in a two beam condition for Fe (110) meaning slightly tilted away from the (111) pole. Thus, Fe fringes in Fig. 3.23 (d) are less clear than in Fig. 3.23 (b). The location of the interface is not always clear since the contrast difference between Fe and GaAs is not large. Furthermore, there may be a tilt away from

interface plane due to a misorientation of the surface (the wafer specification was ± 0.5°). Nevertheless, the interface appears to change from Fe to GaAs within 2 nm. There is no evidence of a continuous interfacial layer.

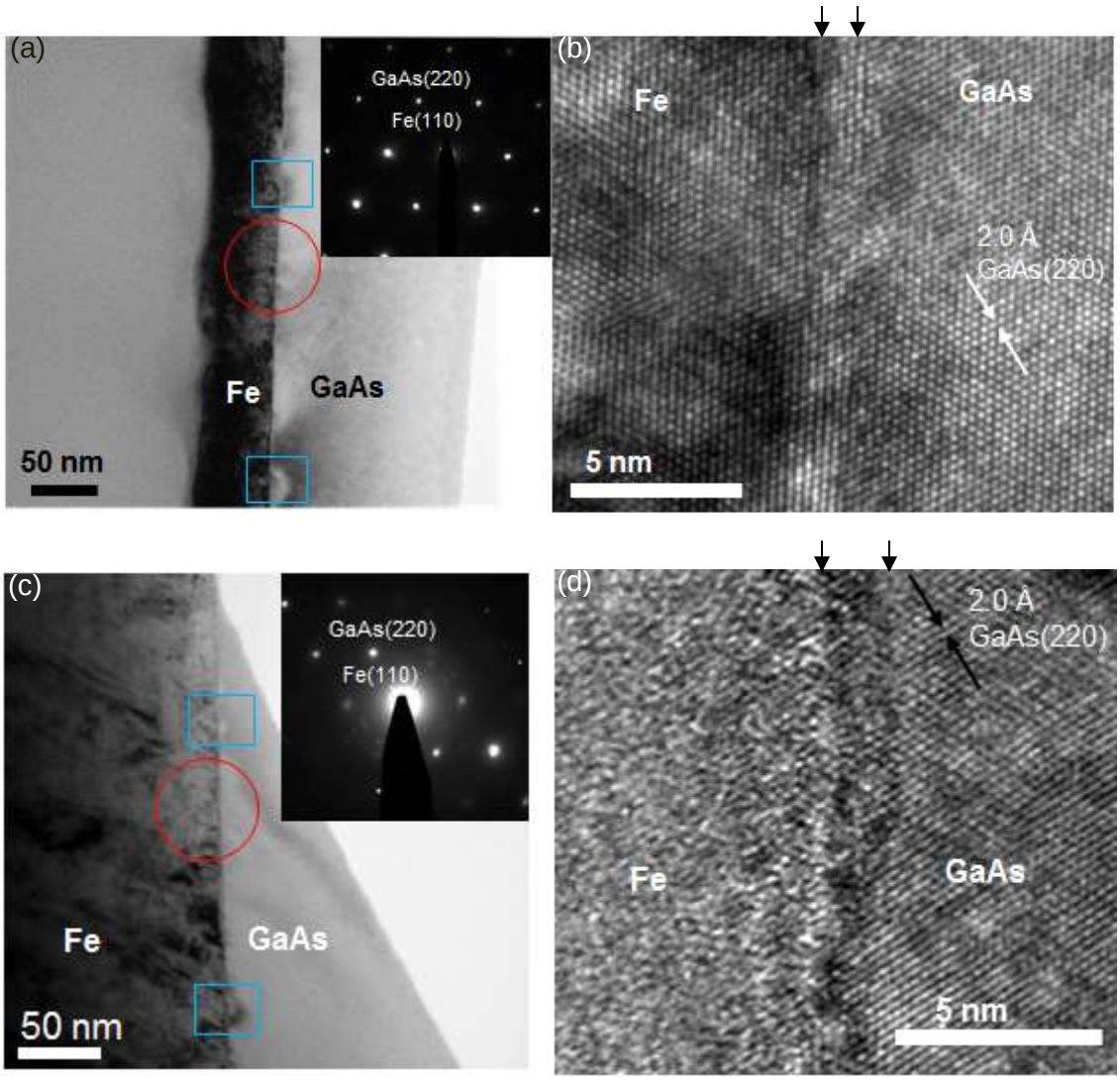

Fig. 3.23. BF lattice images from (111) cross-sectioned samples B1-2 and B1-7 grown at (a), (b) RT and (c), (d) 50 °C, respectively. The (111) diffraction pole is confirmed by the diffraction pattern obtained. The BF image shows circular bend contours (blue rectangles) at certain locations at the interface due to strain in the film and dark contrast and lines because of thickness variation and bending in the thin sample. The lattice spacings are 2.0 *Å* originating from GaAs (220) and Fe (110) lattice planes. Arrows on top of the images (b) and (d) show the interface.

3.2.1.1. Summary of TEM results from Fe on Bulk GaAs

There is a clear island growth and coalescence process that results in small-angle grain boundaries visible particularly in defocussed TEM images. There was also evidence of the presence of randomly oriented grains, particularly from the TEM diffraction pattern. A continuous ED Fe film was obtained for growth times $\geq$ 14 s. Planar {112} stacking fault defects, were detected under appropriate TEM diffraction conditions. These defects have been reported before by us as well as by another group, from TEM and XRD [23, 61]. Since these defects were well aligned with respect to each other they are further evidence for essentially single crystalline material.

No difference in the crystallographic structure of the interface of Fe/bulk-GaAs (110) was detected by HRTEM between samples grown at RT and 50 °C. However, the thicknesses of the samples were different. The width of the interface when viewed down the pole (111) for the RT sample was less than the resolution of the TEM (0.2 nm). In the case of the 50 °C sample, the view was not perfectly aligned with the (111) pole. Hence, the interface appeared artificially wider ~ 2 nm.

3.2.2. Fe on epi-GaAs (Sample E1)

Fig. 3.24 shows a plan-view BF image and SAD of a Fe film on sample E1 (sample E1-6) grown at RT for 9 s. The strong random diffraction contrast in the Fe film indicates a polycrystalline microstructure. The rings in the diffraction pattern confirm the presence of polycrystalline grains. The Fe film is predominantly oriented epitaxially as indicated by the overlapping strong spots in the diffraction pattern from Fe and GaAs crystal lattices. The BF image reveals that the film growth is discontinuous indicating coalescence of the Fe nuclei is incomplete at this growth time similar to Fe growth on bulk GaAs (110) sample. The average feature size in the BF image is 100 nm.

Fig. 3.25 displays a BF image and SAD obtained from near the corner of a rectangular Fe bar of 10 µm × 50 µm (part of a spin structure) made of Fe/epi-GaAs (001) sample (sample E1-7). The BF image shows the individual nuclei with facets along the <110> directions, some are rotated 45° to the <100> directions (circled areas).

The part of the image with uniform dark contrast is the thicker continuous patterned Fe film parallel to [001]. Elsewhere we see the discrete formation of individual crystals indicating that ED growth at the edge of the bars was discontinuous. The average crystal size is 150 nm ± 10 nm. The diffraction pattern shows a strong (001) pole with indication of polycrystalline grains (rings).

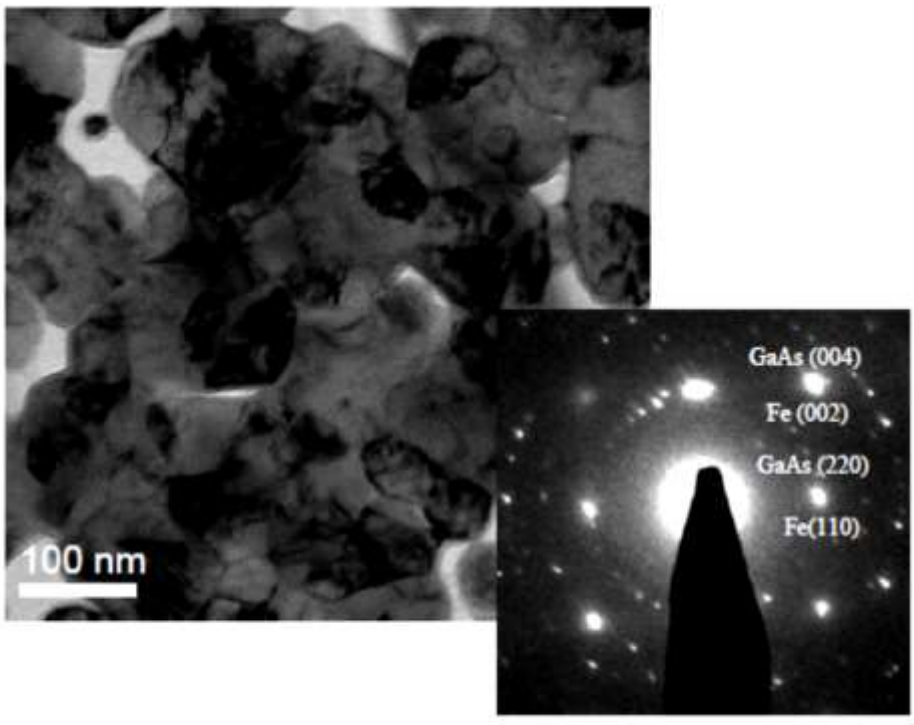

Fig. 3.24. Plan-view BF image and corresponding SAD pattern from Fe (001) quasi single crystalline structure of sample E1-6. Polycrystalline grains are present as indicated by the rings in the diffraction pattern and darker contrast grains in the image. The average grain size is 100 nm ± 10 nm.

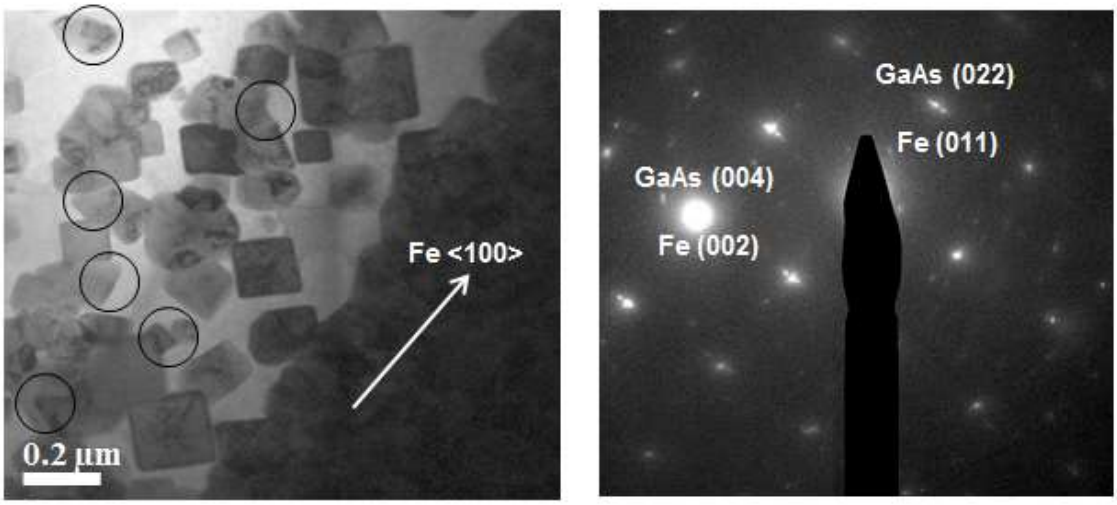

Fig. 3.25. BF image and SAD of one edge of a Fe/epi-GaAs (001) patterned bar (part of a spin structure of a low doped sample E1-7, 2×10^{18} cm^{-3}). We see uniform darker contrast due to the thicker Fe film in the main part of the bar. On the edge are discrete Fe crystallites that did not coalesce. Facets along <110> are visible in some. The BF image also reveals that some of the Fe crystals are rotated from <110> direction (circled regions). The diffraction pattern shows strong diffraction spots consistent with a (001) pole and rings from polycrystalline grains. Average Fe crystal sizes are 150 nm ± 10 nm.

3.2.2.1. Summary of TEM results from Fe on epi-GaAs

Continuous ED Fe films grew on epi-GaAs (100) sample for growth times ≥ 14 s, similar to growth on bulk GaAs samples. The crystal structure was quasi single crystalline, also similar to growth on bulk GaAs. But the lateral grain size found in plan-view BF TEM images of 150 nm is larger than the grain size of 40 nm on bulk samples at RT for a similar growth time. From BF images (Fig. 3.25) it is evident that the growth of the Fe film at the edges of spin contacts is not continuous. This happens due to the high resistance to Fe electrodeposition at the corners and at the edge of the bar openings as was explained in the section 2.3.1.

3.3. Atom probe tomography

Atom probe tomography (APT) was performed by T.Y. Prosa, IMAGO to analyse the chemical composition at the atomic level. They first prepared tip-shaped samples (diameter 40 nm) fabricated by focussed ion beam (FIB) milling. A high DC field is applied at the tip while a laser pulse (energies ranging from 0.2 nJ to 0.02 nJ) is used to evaporate a few atoms at a time which ionize and are then detected by a position-sensitive detector. It was found that a medium laser energy of 0.08 nJ was the best compromise for efficient ablation of atoms from the sample tip. Higher energy (0.2 nJ) produced low resolution for GaAs and the interface, but was good for Fe analysis, while lower energy (0.02 nJ) was good for GaAs analysis, but poor for Fe and often caused specimen failure during analysis. The sputtering direction was from the GaAs towards the Fe to avoid artifacts that might increase the Fe concentration in the substrate. Fig. 3.26 illustrates (a) the FIB lift out process, (b) the commercially available conducting post (Ag) for the sample holder, (c) mounting of the fibbed sample onto the Ag holder and (d) milling of a sample of GaAs/Fe for a tip prior to APT measurements [62].

Atom probe tomography (APT) was performed to analyse the chemical composition of an ED Fe/GaAs interface of samples B1-3 and B1-6 grown at RT and 50 °C, respectively. Pre-analysis SEM images of the sample tips are displayed in Fig. 3.27.

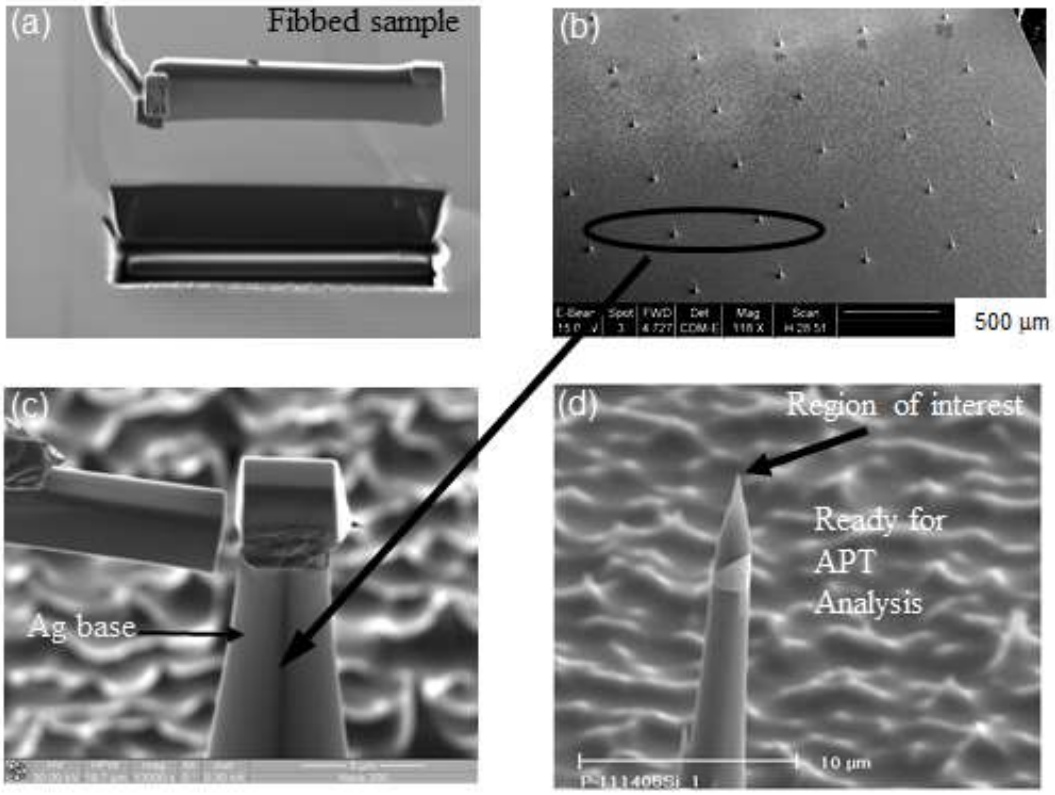

Fig. 3.26. SEM images taken by T.Y. Prosa, IMAGO, during (a) the FIB lift-out process where the Fe/GaAs interface is visible, (b) lower magnification image of the silver (Ag) base holder for the sample (conductive post) (c) higher magnification image of the fibbed lift-out sample placed on the Ag holder, and (d) final milled tip of a sample used for atom probe tomography measurements and analysis.

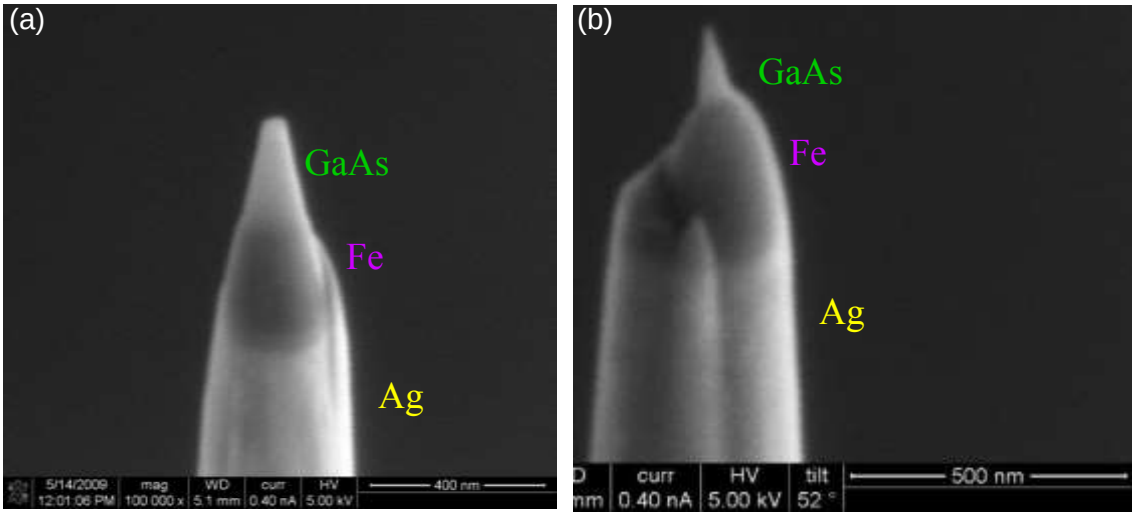

Fig. 3.27. SEM images of (a) RT and (b) 50 °C grown Fe/GaAs(110) sample (B1-3 and B1-6, respectively) fibbed into a tip shape with GaAs at the top prior to atom probe tomography analysis.

Fig. 3.28 displays a side view of an atomic concentration map and an average atomic composition profiling of the fibbed samples (a), (b) for RT and (d), (e) 50 °C grown sample (B1-3 and B1-6 with similar growth time). The elements are colour coded as indicated in (b) and (e) illustrating that the atomic profile through the interface includes evidence of other elements (oxygen, carbon and nitrogen) at the interface besides Fe, Ga and As. Fig. 3.28 (c) displays a plot of counts versus mass to charge ratio, from the Fe side of the interface (top region of interest, ROI), showing the presence of different mass fragments (labelled in the spectrum) including the presence of Iron oxides, FeN, and FeC. Preliminary results confirm that the ED Fe-GaAs interface had detectable levels of impurities including N, C, or O (oxygen impurities of 3.5%, 12%; at RT and 50 °C, from Fig. 3.28 (b) and (e), respectively) in an interfacial region of thickness 8 nm - 10 nm. In Fig. 3.28 (b) and (e), moving from the GaAs to the Fe side, when a Fe signal was first detected the C and O were also detected. Thus, the Fe comes with these impurities when first encountered. The resolution is limited by the roughness of the interface, shape and size of the sample tip, and the uniformity of the laser ablation rate across the interface and evaporation field variation of each element.

Fig. 3.29 demonstrates an atomic concentration map and a corresponding energy spectrum of charge to mass ratios for the GaAs only region to confirm that the impurities in the Fe sides are from the sample and not from the APT measurements.

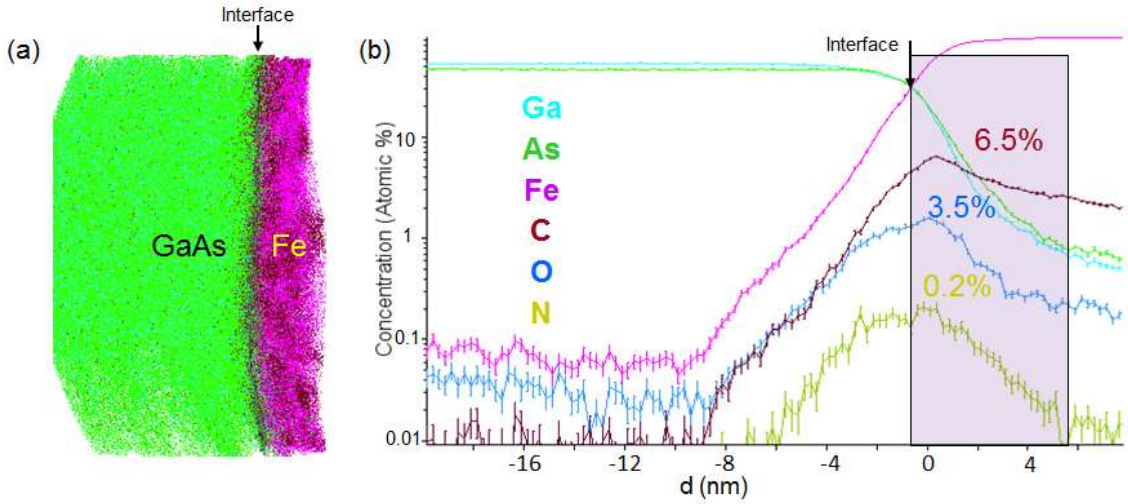

(c)

Top-Level ROI - Bulk Composition

Ion Type	Count	Ranged (%)
Fe	2514453	96.702
C	56443	2.170
O	12311	0.473
N	8504	0.327
As	5929	0.228
Ga	2549	0.098

Ionic Atomic Decompose

Background Corrected

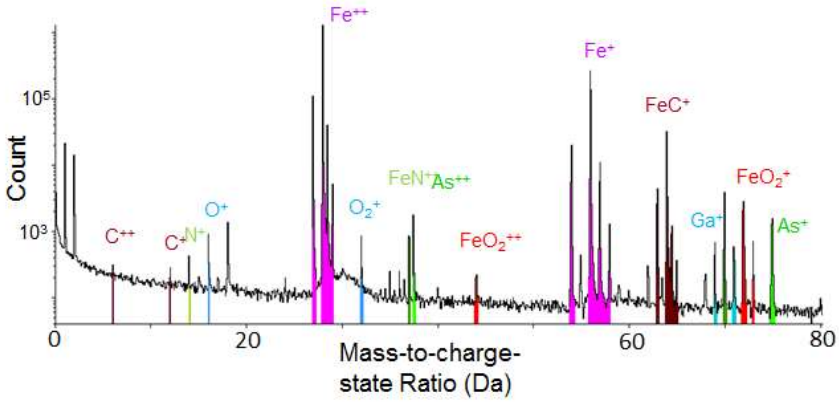

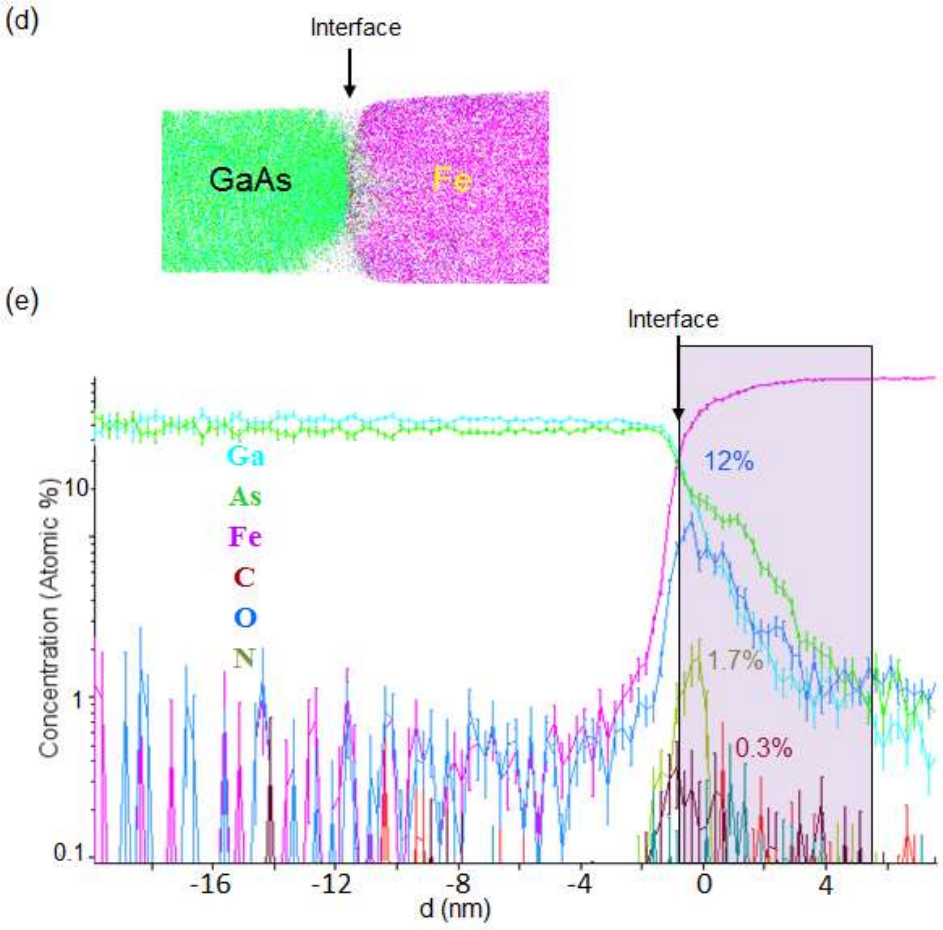

Fig. 3.28. Average atomic concentration map around interface and corresponding plots of average atomic concentration with distance along a direction perpendicular to the interface (shown by a black arrow) (a), (b) for RT and (d), (e) 50 °C grown samples (B1-3 and B1-6). The maximum atomic percentage of O is 3.5% (RT) and 12% (50 °C) as labeled in (b) and (e) using color codes displayed in the atomic profile in (c), in which counts versus charge to mass ratios of each element is plotted at the interface and Fe side of Fe/GaAs (RT sample only).

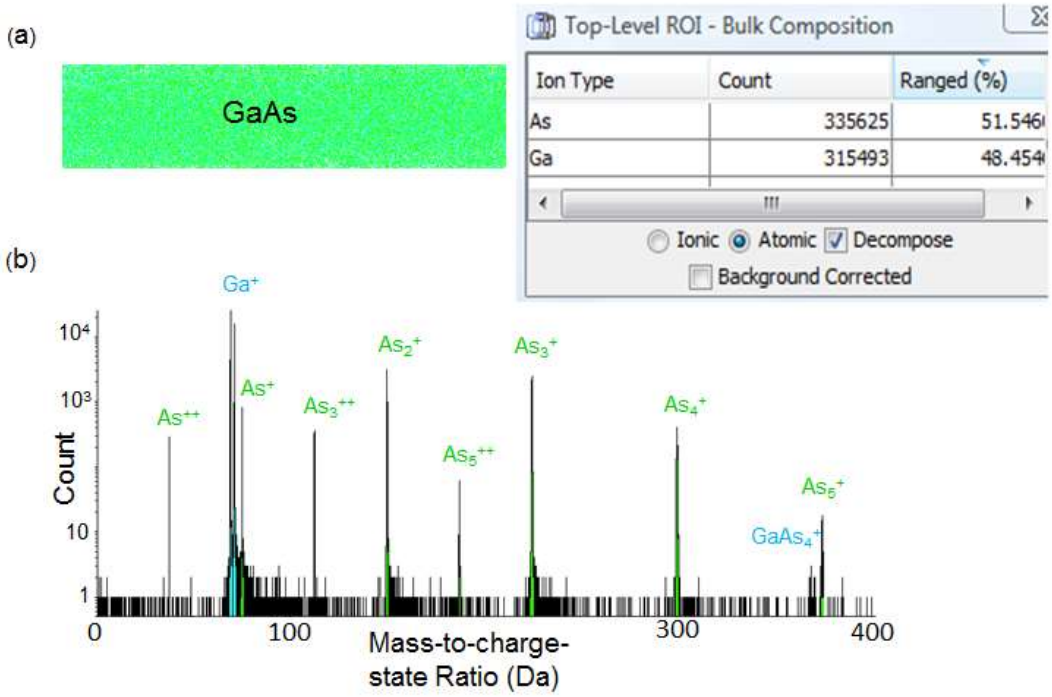

Fig. 3.29. (a) Average atomic concentration map and (b) counts versus mass to charge ratios of each element in the GaAs only region, confirming that the impurities found at the interface and Fe side are from the ED process.

3.4. Conclusion of structural properties

From TEM and XRD investigations it is evident that ED Fe films on bulk GaAs and on epi-GaAs samples consist predominantly of quasi single crystalline material. A continuous Fe film grows for deposition times greater than 14 s for both the cases. The average lateral grain sizes of the Fe on bulk GaAs (110) sample from TEM images increased from 40 nm for the growth at RT for 14 s to 120 nm at 50 °C for 86 s. These values are comparable to the previous reports for ED Fe/GaAs (100) with grain sizes of 30 nm at RT for 3 s to 200 nm at 64 °C for 60 s [23]. This result is not very conclusive as the thickness of samples grown at RT and 50 °C is different. However, the average grain thickness in the out-of-plane direction of samples with similar growth time, estimated from the HRXRD peak FWHM, showed a similar trend as the TEM results (33 nm and 93 nm at RT and 50 °C, respectively). The presence of randomly oriented

grains was confirmed from TEM investigations and pole figure plots. These defects also decreased in concentration at the higher growth temperature consistent with the other structural measurements.

The vertical grain size of 30 nm for Fe on epi-GaAs samples (E1-7) obtained from HRXRD was smaller than the average lateral grain size of 150 nm found in plan-view BF TEM images. This result is different for the similar growth on bulk GaAs sample (B1-2) at RT, for which the vertical grain size is 24 nm and lateral grain size is 40 nm. Comparing Fig. 3.23 and 3.24 it is evident that the Fe on epi-GaAs is not as good quality as Fe on bulk GaAs sample. This is not surprising because of the difficulties of Fe electrodeposition on these more resistive samples, as mentioned earlier in Chapter 2. A larger mosaic spread was also observed in these ED films showing that there was more misalignments of the grains than in Fe on bulk GaAs. All these factors may be the result of slower nucleation rates from the higher sample resistance.

The smaller relaxed film lattice constant calculated from the HRXRD results compared to pure Fe indicates the likely presence of impurities such as oxygen within the films [24, 63]. Oxygen impurities would cause a reduction in the average lattice constant based on the known properties of oxygen doped Fe [57]. However, a measurement of the effect of controlled amounts of added oxygen on the Fe lattice constant has not been reported.

While the XTEM of bulk interfaces shows no evidence of a uniform low density interfacial layer, atomic composition profiling of Fe/GaAs (110) via atom probe tomography shows evidence of 4% - 12% oxygen, and 6.5% - 0.3% carbon impurities at the interface within the depth resolution of the technique, which is 8 nm. The profile width is a function of how flat the interface is compared to the shape being ablated [61]. Abrupt profiles were difficult to obtain considering the ablation rate of Fe is 10 times that of GaAs, and that edges were preferentially removed compared to the centre. Differences in the As and Ga signals, which should be the same, are another indication of calibration difficulties. The shape of the Fe profile matched that of C and O impurities detected suggesting that they were all coming from the same location, at the interface or at grain boundaries of the Fe film intersecting the interface. Grain boundaries in the Fe were found to have more FeO signal than elsewhere. Thus, there would likely be

lateral non-uniformities in the impurity concentration at the interface. However, the XTEM of the Fe on epi-GaAs sample was not carried out so we do not know how thick the oxide layer is in the spin contact.

4. Magnetic Properties

The magnetic properties of Fe contacts play a crucial role in spin transport. In this chapter theory and the experimental techniques of SQUID, MOKE and FMR measurements have been described. The results from these experiments for ED Fe films grown on bulk GaAs (110) and for spin contacts on epi-GaAs (001) are also presented. MOKE images of spin contacts showed magnetic switching between parallel and antiparallel orientations of Fe bars in a sweeping magnetic field, a necessary criterion for the detection of spin voltage at a lateral detector contact.

4.1. SQUID principles

The magnetization of the Fe films was obtained using a superconducting quantum interference device (SQUID). Fig. 4.1 shows a basic circuit diagram of a SQUID magnetometer. It consists of a SQUID coil that is made of two superconducting Josephson junctions in parallel. This is next to inductance and pick up coils where the sample is placed. The sample was glued onto a thin glass rectangular bar with GE varnish (used for low temperature and magnetic measurements), then slid down a plastic drinking straw attached to a holder, and placed inside the pick-up coil. The applied *H*-field direction and the oscillation in the pick-up coil are both along the axis of the straw. The working principle for the magnetometer is that the change in magnetic flux inside the SQUID coil, with applied magnetic field is a multiple of a flux quantity, $\varphi_0 = h/2e$, where *h*, is Planck's constant. The phase change (δ) in the wave function of superconducting current at two Josephson junctions can be expressed in terms of φ_0 as [64],

$$\delta + \frac{2\pi}{\varphi_0}\varphi_T = 2\pi n, \tag{4.1}$$

where φ_T is the net flux inside the coil and *n* is an integer. In an applied magnetic field the magnetization of the sample influences the magnetic flux inside the pickup coil. When the sample oscillates, the change in magnetic flux in the pickup coil generates current in the secondary coil which is magnetically associated with the SQUID coil. So a current is induced in the SQUID coil, which can be transformed into a voltage modulation equivalent to the magnetization. The current (*I*) induced in the SQUID coil can be expressed as [65],

$$I = -I_0 \sin\left(\frac{2\pi\varphi_T}{\varphi_0}\right), \tag{4.2}$$

where I_0 is the critical current in the SQUID coil (the maximum current that flows through the coil in the superconducting phase).

Magnetization, *M*, versus applied magnetic field, *H*, (hysteresis plots) as a function of the in-plane direction of H were measured using a reciprocating sample option (RSO) in the SQUID. RSO measurements can be carried out in two ways, either by centered or maximum slope scans. Centering scans were chosen as these produce the most accurate results with a sensitivity of 5×10^{-9} emu [65]. In this measurement, a servo motor oscillates the sample around the center of a pickup coil. Before the measurement, centering of the sample (calibration) with respect to the pick-up coil is obtained from the SQUID response to the magnetization of the ferromagnetic sample. The maximum value of *M* at each value of H (magnetic hysteresis plot) is obtained from 4-8 oscillations of the sample. 8 oscillations were chosen for each measurement for the sake of increased accuracy. As a result, the whole curve takes longer to obtain, but during each *H*-field value *M* is measured in the center of the pickup coil minimizing error.

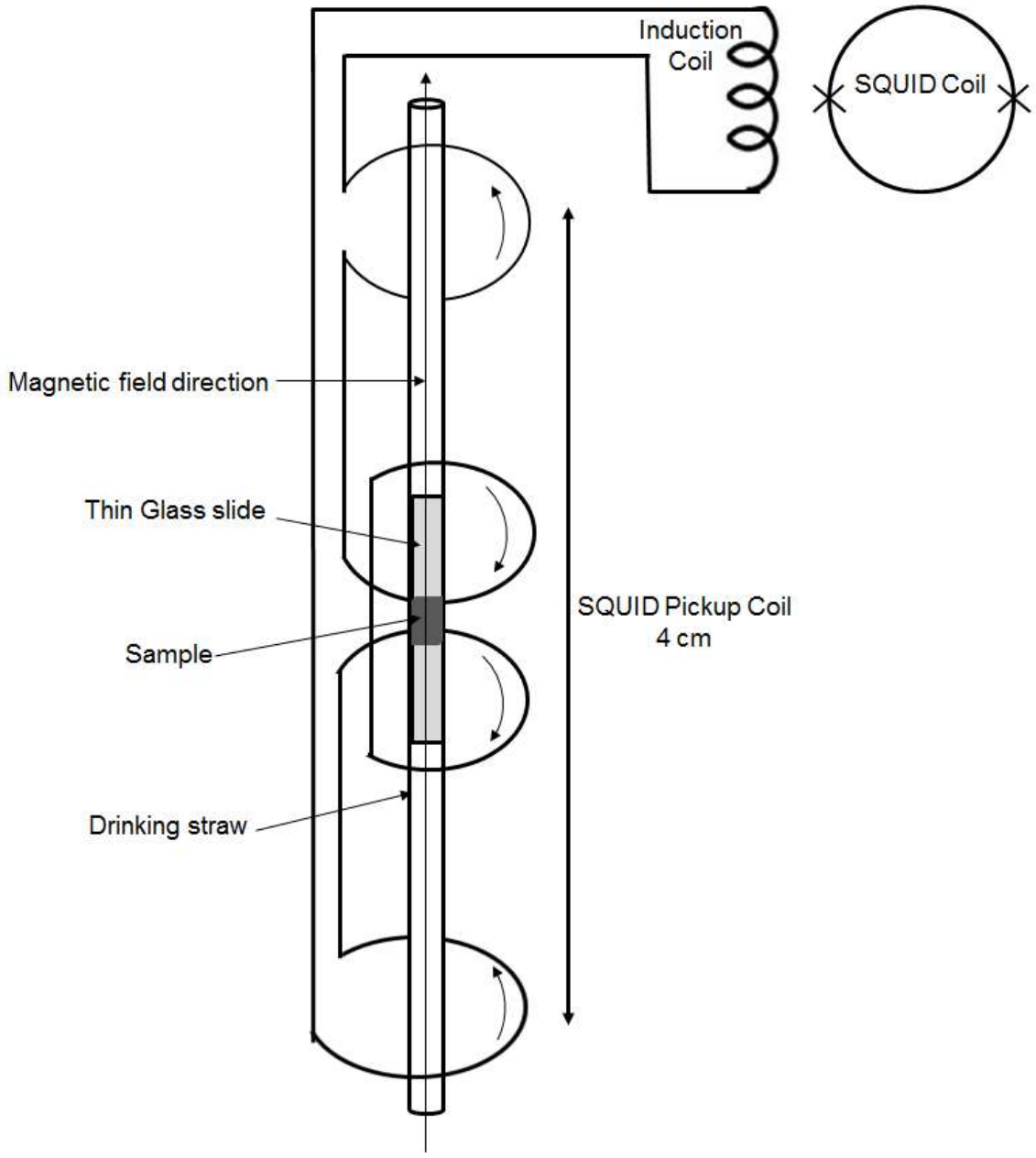

Fig. 4.1. A circuit diagram for the SQUID magnetometer showing a SQUID coil with two Josephson junctions (two crosses) and a secondary coil consisting of an inductance coil and a pick up coil. It also shows the sample assembly inside the pick-up coil (4 cm in length). The pickup coil is placed vertically inside the SQUID chamber. The direction of the sample oscillations and the applied magnetic field are along the length of the straw. The direction of current flowing in the pickup coil is shown by arrows. The sample glued to a glass slide is aligned such that either its <100> or <110> direction was along the applied magnetic field.

We performed micromagnetic simulations to model the magnetic hysteresis loop measured via SQUID. The sample was imagined to consist of a periodic lattice of planar domains, each with a volume of 64 nm x 64 nm x 2 nm as shown in Fig. 4.2 [66]. One boundary of the sample is along an in-plane $< 1\bar{1}0 >$ axis and the other along the perpendicular <001> direction. The perpendicular direction is a <110>.

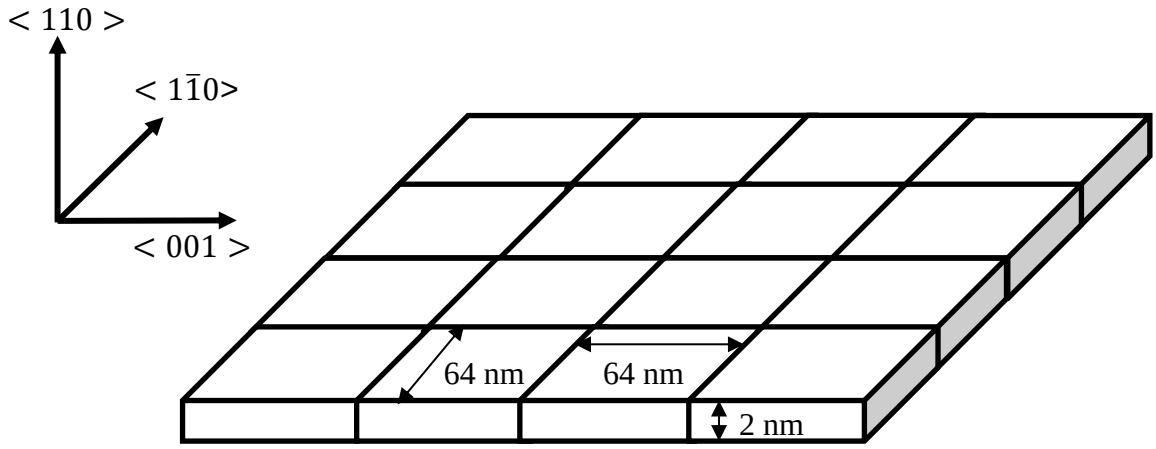

Fig. 4.2. Sample model consisting of a square pattern of magnetic domains (64 nm × 64 nm x 2 nm) with uniaxial anisotropy applied along the sides. The sides are parallel the crystallographic in-plane <001> and $< \mathbf{1\bar{1}0} >$ directions. The perpendicular direction is along <110>.

4.1.1. Fe on bulk wafers (sample B1)

Magnetic hysteresis plots, magnetization versus applied magnetic field, for ED Fe films of different thicknesses grown on bulk GaAs (110) are shown in Fig. 4.3 (sample nos: B1-2, B1-3, and B1-4; thickness: 96, 178, 245 nm, respectively). These characteristics display some of the expected behavior of bulk Fe. The easy and hard axes are along in-plane GaAs [100] and [110] directions, respectively, and the coercivity, H_C, increases with decrease in film thickness (Inset in Fig. 4.3). Fig. 4.4 (a) and (b) Fig. 4.4 shows magnetic hysteresis, major loops along crystallographic in-plane [100] and [110] directions with several minor loops obtained along in-plane [110] for ED Fe (a) RT deposited thickness 96 nm (B1-2), and (b) 50 °C deposited 300 nm (B1-7).

The coercive field is smaller for the 50 °C Fe film compared to the RT film because its thickness is 3 times larger. These plots display several discrepancies from expected behavior for a thin single crystalline Fe film. They cannot be explained using homogeneous rotation of the magnetization with uniform cubic plus uniaxial anisotropy. Deviations from expectations include a hysteresis along [100] showing curvature around saturation; the coercive field, $H_{C,}$ width of the hysteresis plot at zero magnetization is the same along both easy and hard axes, and minor loops extend outside major loops (In Fig. 4.4 black arrows point to minor loops).

When the field is applied along the in-plane [001] direction, magnetization occurs due to domain wall motion between domains along [001] and $[0\bar{0}1]$. However, from the plot we see that H_C is the same along the easy and hard axes, implying in-plane inhomogeneities are pinning domain wall motion. Rounding of the curve near saturation occurs from a distribution of easy axes about the mean [001] direction. Minor loops inside the major hysteresis loop describe the detailed information regarding the domain pinning of a ferromagnetic film [66, 67].

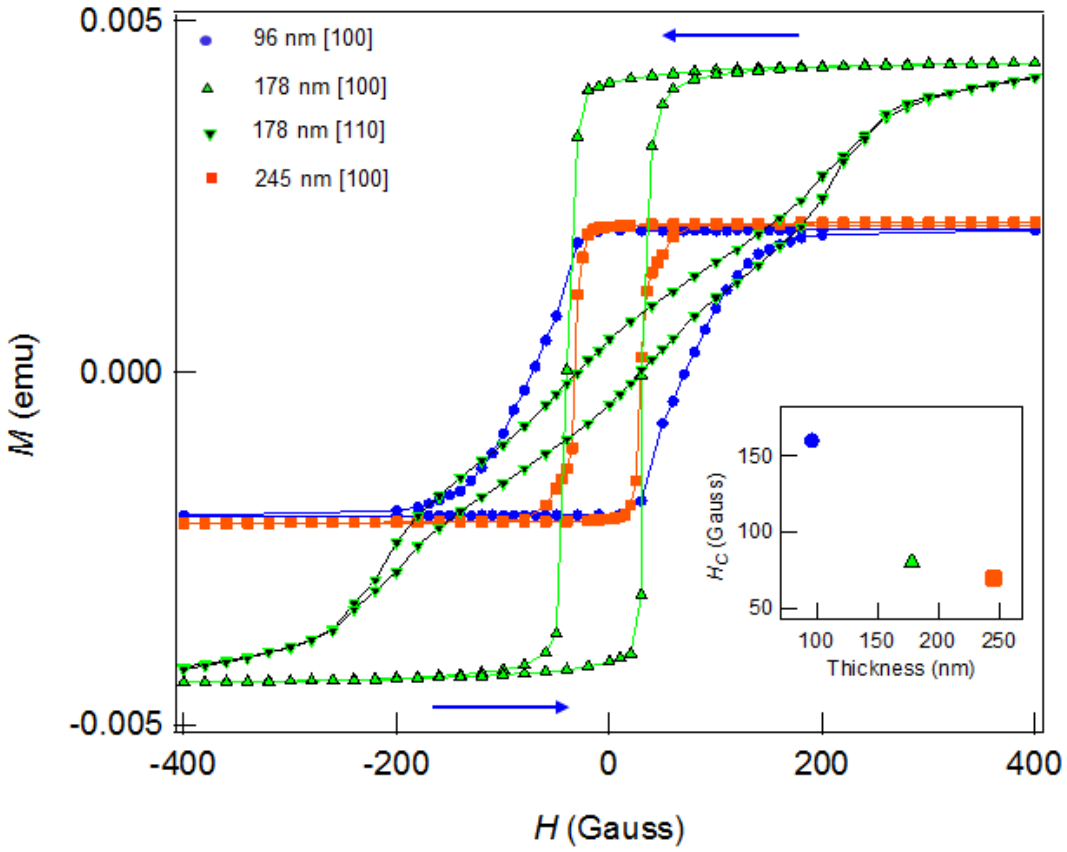

Fig. 4.3. Plots of hysteresis loops, magnetization, *M*, versus applied in-plane magnetic field, *H*, as a function of thickness of Fe film and the direction of applied *H* (sample no: B1-2 – B1-4). The coercive field, H_C, or the width of the loop at zero *M*, is plotted in the inset as a function of Fe thickness. The sweep direction of the applied field is indicated by the blue arrows on top and bottom of the plots. Hysteresis loops along in-plane [100] and [110] directions are shown only for films of thickness 178 nm for clarity (all others were similar). Like bulk Fe, the direction of applied *H* where *M* is easiest to switch, the easy axis, is along the in-plane [100] direction while the hard axis is along the in-plane [110].

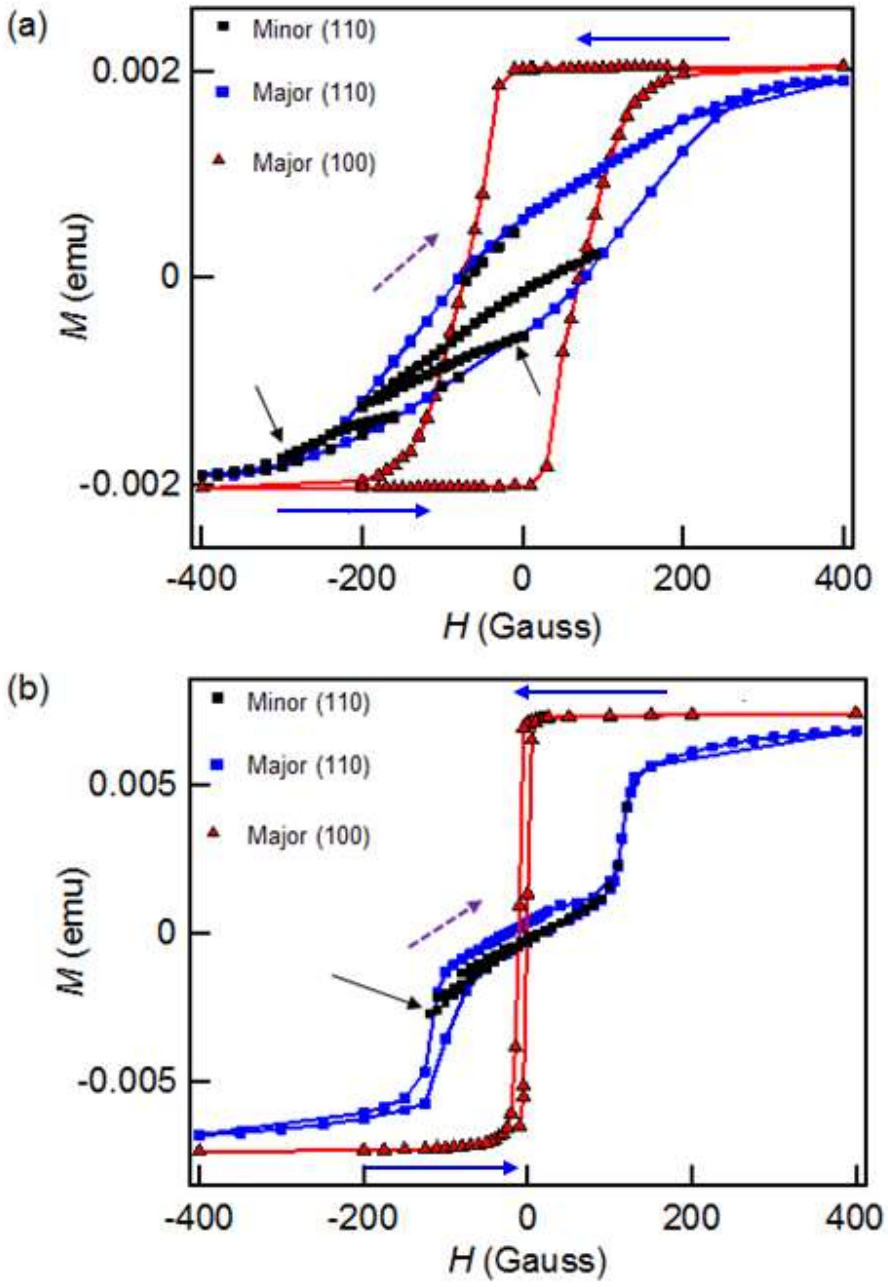

Fig. 4.4. Magnetic hysteresis loops along in-plane easy [100] and hard [110] axes of samples B1-2 and B1-7 grown at (a) RT, thickness of 96 nm, and (b) 50 °C, thickness 300 nm, respectively. Minor loops along the hard axis are lying outside the major loop in the regions indicated by black arrows. The sweep direction of the field for the major loops is shown by the blue arrows on the top and bottom of the plot and for the minor loops by the dashed purple arrow.

Dr. Anthony Arrott modeled minor loops using Scheinfein's LLG micromagnetic simulator to analyse the nature of magnetization in these ED Fe films [66]. Fig. 4.5 shows plots of calculated magnetization versus applied field. The dotted purple line (labelled "cubic") to the left is a theoretical plot of magnetization for Fe with only cubic anisotropy occurring when a magnetic field is applied along the [001] direction, for which an unstable field is reached at 100 G. A greater field (> 100 G) is needed in the negative direction and then the resulting hysteresis loops would be completely square loops. If sufficient uniaxial anisotropy is added uniformly throughout the sample, while reducing the contribution of the cubic anisotropy to keep the initial slope as it was without the uniaxial anisotropy, the hysteresis can be suppressed as shown by the middle curve (dark green labelled "both"). If there is only uniaxial anisotropy the magnetization process is linear to saturation as shown by the line to the right (purple solid line, labelled "uniaxial"). Major (blue) and minor (black) loops (magnetization versus applied field along the hard axis in-plane <110>) for Fe/GaAs(110) for the sample (B1-2) with thickness of 96 nm are illustrated with the theoretical plots to show that none of the above simulations could model the magnetization curve well.

Results from the micromagnetics calculation of Fig. 4.5 just described revealed that hysteresis along the hard axis in Fig. 4.4 cannot be from cubic anisotropy of Fe acting alone. The cubic anisotropy of Fe would account for a more rapid increase in magnetization with increasing field but would lead to a jump that is not observed. The problem of magnetizing in the [110] direction for a thin film is that the magnetization is confined to the film plane by the demagnetizing field which forces the magnetization to rotate through the magnetically hard in-plane [111] direction. Once the field is sufficient to do this, the magnetization jumps to the [110] direction. Reducing the field and going in the negative direction requires overcoming the same barrier and that results in full saturation in the opposite direction. Adding uniaxial anisotropy can suppress this hysteresis but, to fit the data, one would have to invoke an unlikely decrease in the fundamental cubic anisotropy of iron, which is not observed in the ferromagnetic resonance experiment above saturation. In any case, the modeling with uniform rotation cannot account for the slow approach to saturation using uniaxial anisotropy with an easy axis along the [001] [66].

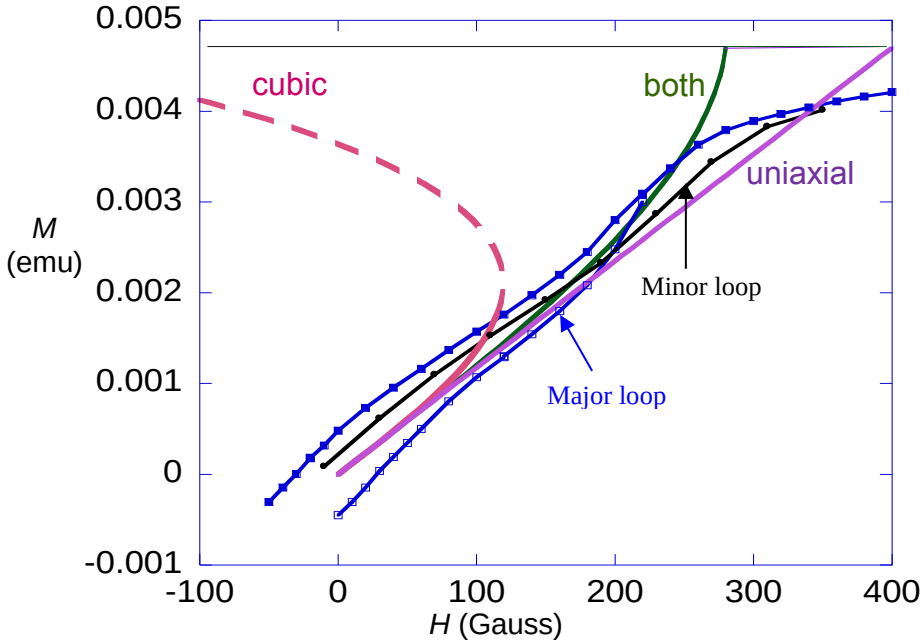

Fig. 4.5. Magnetization versus applied field along an in-plane hard axis <110> for sample B1-2 of thickness 96 nm, blue line (major loop) and black line (minor loop). Theoretical results from micromagnetic simulations for magnetization of Fe film using three different conditions are overlaid with the data, i) cubic anisotropy (purple dotted line) ii) uniaxial plus cubic anisotropy (green, labelled both) (1:1) iii) only uniaxial anisotropy (purple solid line).

Further micromagnetic simulations for the minor loop along the hard axis in-plane (110) were carried out by adding uniaxial anisotropy locally to the boundaries with the preferred axis along the boundary of the crystal domains. This model is described in Fig. 4.2. The domain edges correspond to the regions where the uniaxial anisotropy is present, and in our model these are defect regions from coalescence of the separately nucleated regions. The uniaxial anisotropy is added to the boundaries with a preferred axis along the boundary.

Fig. 4.6 shows results from the simulations. As the strength of uniaxial anisotropy is increased from calculation to calculation, there is a small increase in susceptibility at low fields as compared to just cubic anisotropy alone (pink line in Fig 4.5) because anisotropy along [100] and [010] helps in the magnetization process. When the uniaxial anisotropy assigned to the boundary cells reaches 1.7 MJ/m^3, the hysteresis loop is greatly narrowed, as shown in Fig. 4.6 (green line with hysteresis). When the anisotropy of the boundary cell is increased further to 2.1 MJ/m^3, the curve is reversible and the simulation approaches the experimental plot for the minor loop (red line in Fig. 4.6 without hysteresis).

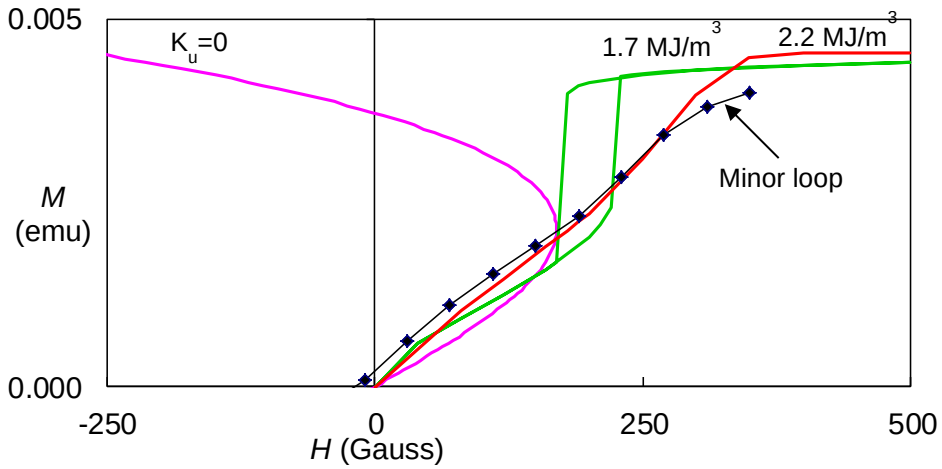

Fig. 4.6. Plot of the results of micromagnetic modeling of minor loops in the hysteresis plots of Fig. 4.4 for sample B1-2 using local regions of uniaxial anisotropy described as tiles and grout, with cubic anisotropy of iron acting everywhere. The instability curve for uniform rotation with the cubic anisotropy (pink line on left) of iron is repeated from Fig. 4.5. The green curves with hysteresis are for a smaller value of local uniaxial anisotropy without hysteresis. Surprisingly, the addition of local anisotropy increases magnetization at lower fields. The red curve without hysteresis is in fair agreement with a minor loop of Fig. 4.4 (black). The modeling is based on a periodic distribution of regions of uniaxial anisotropy. A more realistic model would have variations in the spacing of these regions, but such a calculation is prohibitive for the available computing resources.

4.1.2. Fe on epi-GaAs (Sample E1)

The magnetization as a function of applied magnetic field along easy and hard axes for Fe/epi-GaAs(100) sample (E1-7) (crystallographic <100> and <110>, respectively) is plotted in Fig. 4.7. The coercivity for <100> is slightly less than that for <110>. The coercivity depends on the mechanism of domain wall reversal with the applied field. The coercive fields along the in-plane <110> and <100> are equal meaning that there is an extra anisotropy acting along with the cubic anisotropy along in-plane [110] directions, pinning domain wall motion (any cubic crystal structure has cubic anisotropy). This anisotropy controls the rotation of domain walls at the reverse field. High resolution x-ray pole figures confirmed that the Fe texture is well aligned in-plane with the crystallographic orientation of the GaAs sample. Thus, if we have cubic anisotropy alone, it would saturate more easily along <100> than <110> and magnetization would increase linearly with field and saturate at the anisotropy field, which is 540 Gauss for bulk Fe [68, 69]. The inset in Fig. 4.7, shows a plot of magnetization against 1/*H* showing a linear behavior (expected) for fields above 1000 G at which point magnetization starts to saturate (magnetization versus applied field along the easy axis). But a non-linear behavior is observed for the 1/*H* dependence of the magnetization when approaching saturation (The point where the hysteresis loop is closed, indicated by the black arrow) indicating local domain pinning is occurring likely due to defects. (If it is a perfect single crystal without any defects then the magnetization change approaching saturation should be abrupt and the behavior of magnetization with 1/H should be linear in that region). The magnetization curves are not following any simple model of rotation against a uniform anisotropy. These hysteresis curves are very similar to the inhomogeneous magnetization seen in ED Fe/bulk-GaAs(110) and Ni-Fe/GaAs(100) [44].

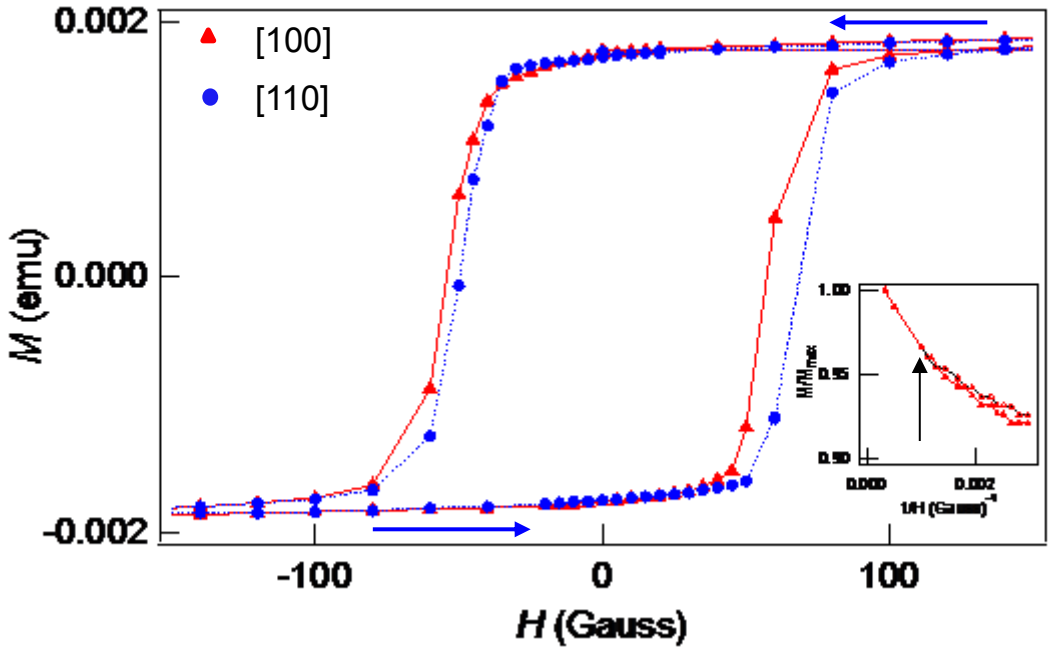

Fig. 4.7. Plots of magnetization, *M* versus applied field, *H*, for Fe on epi-GaAs (001) (sample no E1-7) with *H* parallel to the in-plane [100] (red) and [110] (blue) crystallographic directions. The sweep directions are shown by the blue arrows. Coercive fields are 110 and 115 Gauss along the in-plane [100] and [110] directions, respectively. Rounding of the curve towards the saturation point is an indication of defects in the crystal structure. The inset shows magnetization at saturation as a function of I/*H* (the black arrow shows the saturation point).

4.2. FMR principles

In an FMR measurement the sample is kept in a microwave cavity. A radio-frequency (r.f.) magnetic field, applied perpendicular to the static magnetization of the sample, sets up a ferromagnetic resonance. The microwave cavity locks the r.f. frequency at a desired value. When a dc magnetic field perpendicular to the r.f. field ranging from zero to 26 kOe is swept, the applied r.f. magnetic field causes precession of the magnetization of the sample around the dc field. At a certain dc field the precession frequency matches that of the r.f. frequency. To increase the signal to noise ratio of the lock-in detection system an additional AC field is applied with the DC field

with a modulation of 100 Hz. A quantitative analysis of intrinsic and extrinsic impurities in a ferromagnetic sample is possible [70].

The principle of the ferromagnetic resonance (FMR) measurement is based on the Landau Lifshitz (L-L) equation of motion for magnetic materials expressed as [71],

$$\frac{dM}{dt} = -\gamma\left[M \times H_{eff}\right], \tag{4.3}$$

where $\gamma = g\frac{|e|}{2mc} = 1.8379\times10^{7}$, is the gyromagnetic ratio of Fe with g = 2.09, H_{eff}, is the effective field acting on the magnetic moment, M, of the sample. The magnetic anisotropies (depending on the crystallographic orientation of the sample) change the direction of the magnetization in the DC magnetic field (applied to align the magnetization of the sample along the DC field), creating an angle between M and the H_{eff}, that can be incorporated in the L-L equation. The resonance field, $H_{resonance}$, can be evaluated by solving the L-L equation for a particular crystallographic film orientation, in our case (110). The solution is shown as follows in terms of the angular frequency of the microwave signal, $\omega = 2\pi f$ [72]:

$$\left(\frac{\omega}{\gamma}\right)^2 = \left(H_{resonance} + \beta + 4\pi M_{eff} + u_1\right)\left(H_{resonance} + \alpha + u_2\right). \tag{4.4}$$

Here,

$$\beta = \left(2\cos 2\theta - \frac{3}{8} + \frac{3}{8}\cos 4\theta\right)\frac{K_1}{M_{eff}}, \quad \alpha = \left(-\frac{1}{2}\cos 2\theta + \frac{3}{2}\cos 4\theta\right)\frac{K_1}{M_{eff}}, \tag{4.5}$$

$$u_1 = \frac{2K_\mu}{M_{eff}}\cos 2(\theta - \varphi), \text{ and } u_2 = \frac{K_\mu}{M_{eff}}\cos^2(\theta - \varphi), \tag{4.6}$$

where f is the frequency set at the microwave cavity and μ_B is the Bohr magnetron. K_1 and K_μ are the cubic and in-plane uniaxial anisotropy coefficients, respectively, θ is the angle between the magnetic field H (static magnetization) and the crystallographic axis [100] (the easy axis for Fe). The angle ϕ indicates the direction of the in-plane uniaxial anisotropy axis with respect to [100]. $4\pi M_{eff}$ is the sum of the saturation demagnetizing field and out of-plane uniaxial field. From equation 4.5, it is evident that α contains both twofold (2θ) and four-fold anisotropy (4θ) field contributions. In general, for bulk Fe

(cubic) oriented along (110) one can observe from equation 4.5, that the uniaxial anisotropy field is one third of the cubic anisotropy field and both fourfold and twofold anisotropy fields should have the opposite sign.

4.2.1. Fe on bulk GaAs (Sample B1)

Ferromagnetic resonance (FMR) measurements (24 GHz) have been carried out on RT deposited Fe on GaAs (110) (sample B1-2, thickness 96 nm) with an r.f. frequency of 24 GHz. Fig. 4.8 shows a plot of the resonant magnetic field, $H_{resonance}$, as a function of the angle, θ, between the static applied magnetization direction and the crystallographic direction [100] of the sample.

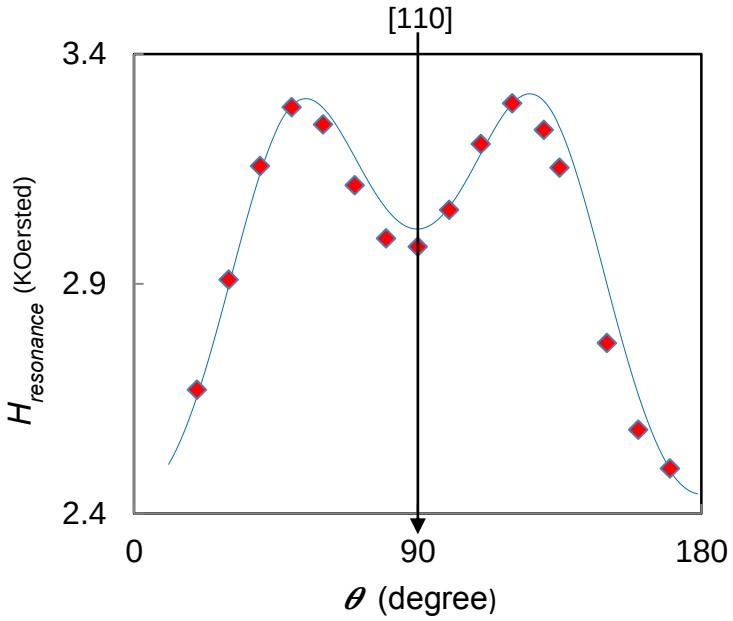

Fig. 4.8. Plot of the ferromagnetic resonance field, $H_{resonance}$ as a function of angle (θ) for sample B1-2, where θ is the angle between the static magnetization direction and the in-plane [100] crystallographic direction. The solid line is a fit obtained using the dispersion resonance equation 4.4 for a (110) orientation of the film.

The solid line in Fig. 4.8 is a fit using equation 4.4 for a surface oriented (110), varying the parameters $4\pi M_{eff}$, K_1, K_μ, and ϕ. Based on this, $K_1 = 3.35\times10^5$ erg/cm^3, $K_\mu = 1.79\times10^5$ erg/cm^3, $4\pi M_{eff} = 1.91\times10^4$ Oerstaed, and $\phi = 90.539^o$.

K_1 with an easy axis along [100] obtained from the fit was smaller than that of the bulk value for single crystal Fe indicating crystalline disorder. An additional positive twofold uniaxial anisotropy K_μ with a [100] easy axis, was obtained from the fit. This anisotropy was not a contribution to the two-fold anisotropy coupled in with four-fold anisotropy in the α term in the resonance equation 4.5. Surprisingly, this additional uniaxial anisotropy is large being half of the cubic anisotropy. In our case the film is thick and bulk-like so it does not originate at the interface. The origin of such a large magnitude of twofold anisotropy could arise locally from two magnon scattering [73].

Fig. 4.9 shows the FMR line-width d*H* versus magnetization direction with respect to the sample orientation (110). d*H* consists of two parts, intrinsic Gilbert damping and external damping. The intrinsic line-width occurs due to spin orbit interaction and the external component due to magnetic inhomogeneities in the sample [71, 66]. From Fig. 4.9 we see that the inhomogeneity along [110] is the higher than that of the [100] direction (line-width is higher along (110) than (100)). The value of the intrinsic Gilbert damping, d$H_{intrinsic}$, in Fe is isotropic, and can be calculated as [70],

$$dH_{intrinsic} = \left(\frac{G}{\gamma M_S}\right) \times \left(\frac{\omega}{\gamma}\right), \tag{4.7}$$

where *G* is the Gillbert damping relaxation parameter and M_S the saturation magnetization. For bulk Fe, $4\pi M_S = 21.5\ \mathrm{KOe}$, and $G = 6.7 \times 10^7 s^{-1}$ [70]. Therefore, $(dH)_{\text{intrinsic}}$ is only 17 Oe at 24 GHz calculated using equation 4.7. The FMR line-width is well above the expected value of the intrinsic line-width of Fe from Gilbert damping. So the extrinsic contribution to the FMR line-width (d*H*) from Fig. 4.9, a maximum value of 332 Oe and a minimum value of 161 Oe, are significantly larger. The extrinsic contributions to the line-width (d*H*) has potentially two parts. The largest contributors have a 90^o symmetry with maxima along [001] and [110] crystallographic axes, and minima approximately 45^o away from the [001] and [110] directions. The smallest contributor (dH_{minima} - d$H_{intrinsic}$) is anisotropic and is approximately 144 Oe. The largest contributor (dH_{maxima} - d$H_{intrinsic}$) is approximately 315 Oe.

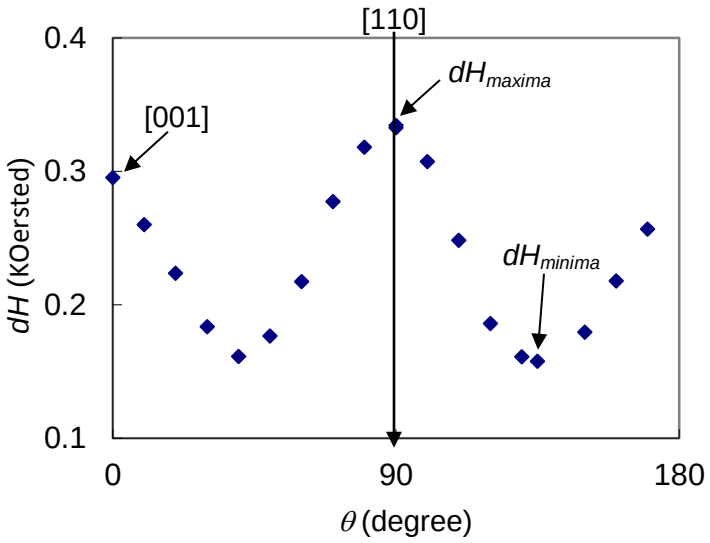

Fig. 4.9. Plot of the variation in resonance line-width, d*H*, with angle θ, of applied magnetic field.

4.3. Magneto Optical Kerr Effect (MOKE) measurement

Magnetic optical Kerr effect (MOKE) was used to image the magnetization of patterned Fe bars as a function of the applied in-plane magnetic field. As shown in Fig. 4.10, an incident beam from a white mercury lamp was collimated and passed through a polarizer where the light beam was polarized parallel to the plane of the incident beam. It then passed through an objective lens onto the sample. The reflected beam from the sample was detected by a charged coupled detector (CCD) camera via an analyser situated at an angle with respect to the polarizer to convert the rotation of reflected light, due to magnetization of the sample, into image contrast. The signal is collected while a magnetic field is applied parallel to the in-plane direction of the sample surface (along the length of the Fe bars shown in the spin structure in Fig. 2.12) and the plane of the incident beam (longitudinal geometry) [74]. The image formed in greyscale depends on the polarization of the reflected beam which is a direct measure of change in magnetization of the sample. The angle between the analyzer and polarizer is adjusted

depending on the rotation of the reflected beam due to change in magnetization of the sample in an applied magnetic field.

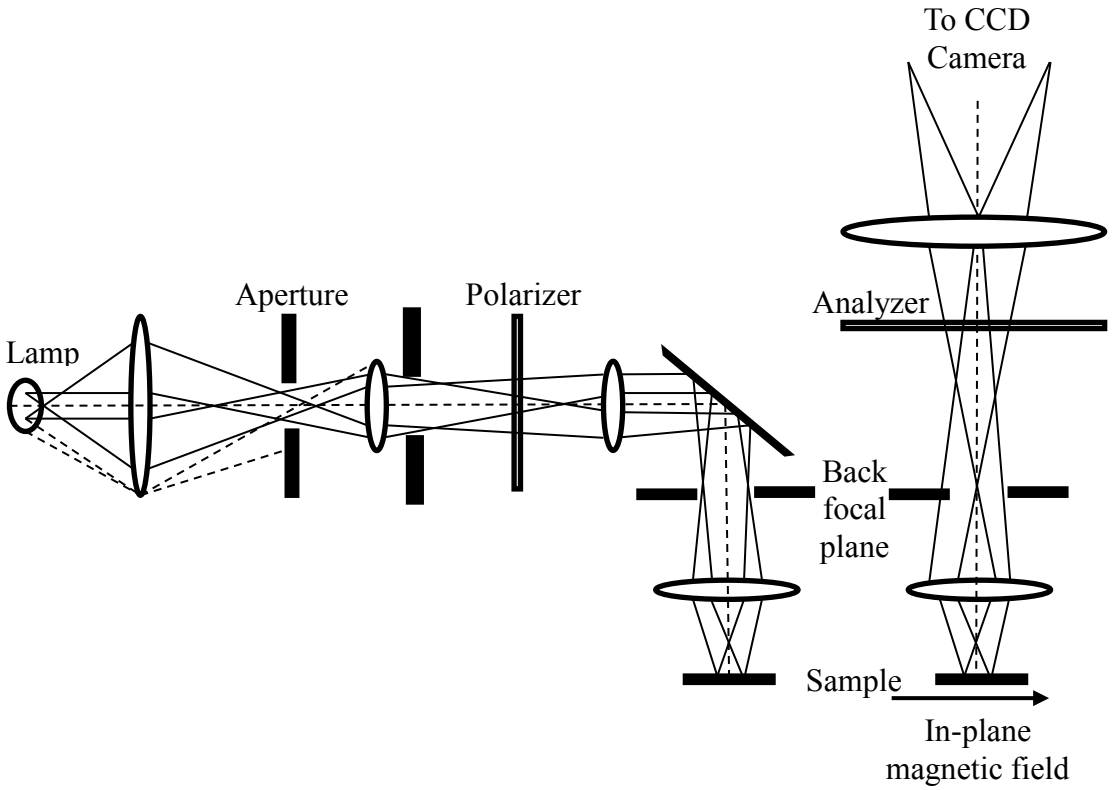

Fig. 4.10. Optical ray diagram for the incident and reflected light path in a MOKE microscope. The angle of the polarizer with respect to the analyzer is adjusted depending on the rotation of reflected light from the sample. A magnetic field was applied in the film plane along the length of the patterned Fe bars. (Redrawn from [74])

4.3.1. Fe on epi-GaAs (Sample E1)

Spin transport phenomena rely on the fact that the directions of magnetization of FM contacts used for the spin injector and the detector will be switching from parallel to antiparallel with an applied sweeping field. MOKE imaging was performed at RT on spin structures consisting of the three central Fe contact bars patterned on an epi-GaAs (100) sample (sample no. E1-7). Fig. 4.11 shows images of 3 contacts (Any two of these bars are used for injector and detector contacts), labelled 1 to 3, as a function of the applied

magnetic field *H*, sweeping between ± 120 G along a Fe in-plane <100> direction (along the length of the bars). The size of each image is limited by an aperture at the light source (30 μm diameter). The plot is a hysteresis curve showing the degree of optical polarization of the reflected light, *P*, as a function of *H*. The black arrows indicate the sweep direction of *H* starting at the top right corner of the *P*(*H*) curve. The contrast in each MOKE image is a measure of change in the in-plane magnetization in the Fe contacts. This change primarily occurs due to in-plane shape anisotropy and other demagnetizing field effects from impurities at the very edges of the contacts. From the hysteresis loop we see that the magnitude of the switching field (each red dot on the plot with field values labelled) for the parallel to antiparallel and then anti-parallel to parallel alignment between contacts 1 and 2, occurred at 53 G and -80 G, respectively. The many steps in the hysteresis curves indicate multiple domains are involved in the switching processes. These are likely also responsible for the local anisotropies found in the micromagnetic simulations of the SQUID minor loops. There are narrow regions of width, approximately 1 μm at both sides of the bars, where the magnetization does not change with the applied field. These correspond to regions of discontinuous film where only discrete misoriented islands were present, visible with plan-view TEM (Fig. 3.25). These regions may also look non-magnetic because the MOKE magnetic detection axis is along the length of the bar and it does not recognize any change in the out-of-plane magnetization.

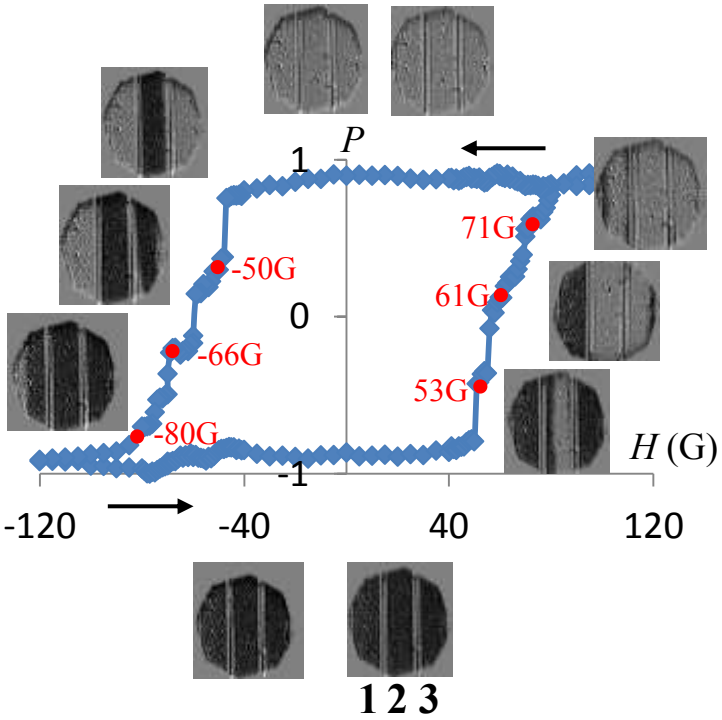

Fig. 4.11. MOKE images and corresponding magnetic polarization, *P*, versus applied in-plane magnetic field, *H*, of three central Fe bar contacts (Any two of these can be used for a spin injector and detector) on epi-GaAs sample (E1-7), labelled 1, 2, and 3. Arrows on the plot indicate the direction of the magnetic field sweeps. Contrast in these images is a direct measure of the change in the in-plane magnetization state. Red dots on the plot show the switching fields for the bars. Measurements were performed at RT. The width of each bar is 10 µm.

4.4. Conclusions about magnetic properties

A comparison of the magnetic hysteresis loops (major loops) for the [110] and [001] in-plane crystallographic directions, for both Fe on bulk GaAs and epi-GaAs samples, revealed the result that the coercivity was the same along both directions for both samples. If we had perfect single crystals then these two directions are the hard and easy rotation directions in thin Fe films (> 50 nm), so we would expect that the coercivity for the [001] direction to be larger. As seen from the TEM and XRD results the

samples have a preferred orientation but the large mosaic width (0.8 deg.) indicates that there is significant randomness to the in-plane orientations.

Magnetization curves are rounded towards the saturation field which indicates that the hysteresis curves do not follow any simple model of rotation against a uniform anisotropy, similar to Fe-Ni/GaAs(001) for which the magnetization can be determined by a strong coupling among the regions of different anisotropy axis [44]. The 1/*H* dependence of the magnetization (Fig. 4.10) at the approach to the saturation point (where the hysteresis loop is closed) shows a non-linear behavior indicating that defects contribute to pinning magnetic domains, which otherwise would have rotated due to the reversal of the field.

The most surprising phenomenon was that minor loops were found to lie outside the major loops. In general, the reversal process of major loops for Fe with the field applied along a [001] direction, is due to the propagation of domain walls, in sequence, through different regions of the material. The curve obtained for the reverse field direction, corresponds to the rotation of magnetization through a small angle until the walls move back through the sample in the reverse of the initial sequence [75]. But, our minor hysteresis loops cannot be explained with this simple model. Uniaxial anisotropy, preferring the [100] crystallographic axes, also does not explain these results unless is added inhomogenously into the modeling. By this we mean, there are smaller regions within the sample that are coupling with local neighbours in a different manner than if the domains of the entire region rotated together.

The micromagnetic model presented in this thesis to simulate minor loops along in-plane <110> (hard) axes had uniform blocks (tiles) each with three different directions for the local uniaxial anisotropies. The basic idea of the model was to introduce strong local uniaxial anisotropy in adjacent regions of the sample on a size scale so that the over-all anisotropy is reduced by the mechanism of exchange coupling of adjacent regions [66].

In the limit of strong exchange coupling between regions, three anisotropies along three different directions of [110], [100], and [111] would add to produce no dependence of the spin-orbit coupling energy on the direction of magnetization. As the

distance between regions with different anisotropy was increased, the exchange coupling weakens, the magnetization process becomes inhomogeneous, and shapes of magnetization curves are drastically altered. The regions of uniaxial anisotropy produce no torques in the limit of uniform magnetization, which can occur in both zero field and high field. These regions serve as “soft” pins of the magnetization, in that the direction of magnetization does rotate and reverse with field in the regions of the enhanced anisotropy. In the region of zero field, the magnetization can show small hysteresis because the magnetization pattern can be inhomogeneous depending of the strength of the local uniaxial anisotropy competing with the bulk cubic anisotropy of Fe. The curvature in the magnetization curve at higher field is explained by this model. The magnetic in-homogeneities shown in Fe/GaAs(110) are consistent with previous observations for ED Fe-Ni alloys on GaAs(001) samples, for which the magnetic hysteresis curves were explained via a similar model [44].

The FMR results indicate that the effective uniaxial anisotropy, $K_{\mu} = \frac{K_1}{2}$, whereas in the micromagnetic models, K_{μ}>> K_1 was necessary for the best fits to the hysteresis data. This is because the exchange coupling between the local regions in the model suppresses the net effect of the large local anisotropies. Local strong anisotropies serve to allow rotation of the magnetization through the hard [111] direction by magnetic “tunnelling”. The broadening of FMR line-widths that we observe is another signature of magnetic inhomogeneities. The line broadening occurs due to increased damping from spin pumping, or two magnon scattering [76-78]. Structural defects observed in the plan-view TEM images, including coalescence boundaries, mosaic tilt, and dislocations due to lattice mismatch, could be sources for two magnon scattering responsible for the extrinsic line width obtained from the FMR measurements.

There was evidence from atom probe tomography as well as the smaller bulk lattice constant of the ED Fe that oxygen impurities may be present within the Fe lattice and at the interface. This potential Fe oxide phase must be ferromagnetic since the hysteresis curves were symmetric around zero field. An anti-ferromagnet, for example, would cause shifts towards one direction.

Experimental detection of spin-dependant transport from one Fe contact to another Fe contact situated within a spin diffusion length relies on the fact that the

magnetization of one contact will switch sooner than the other. Switching of magnetization from parallel to antiparallel alignments in ED Fe patterned bars which were designed for spin measurements was confirmed via MOKE images. The simultaneous hysteresis loop indicated that the magnetic switching fields for a pair of bars were 53 G and -80 G, for the forward and reverse field sweeping directions, respectively. The hysteresis loop also showed multiple switching which originates, we believe, most likely from magnetic multi-domains due to the quasi single-crystalline structure of the films.

5. Transport properties

This chapter describes the theory of the electron and spin transport properties. The results from electrical transport analysis via current density-voltage (*J-V)* measurements, and spin transport via spin valve and Hanle measurements are also presented.

5.1. Electron transport: thermionic and tunneling theories

The basic electronic transport properties of Fe/*n*-GaAs contacts were measured as *J-V* characteristics. In general, a metal-semiconductor interface forms a Schottky barrier which is rectifying or ohmic depending on the barrier height and the doping concentration of the semiconductor. If the work function of the metal is larger than that of the semiconductor, equilibrium is reached by electrons flowing from the semiconductor into the metal, forming a space charge region within the semiconductor called the depletion region. The ions within the depletion region generate a built in electric field that eventually prevents the further flow of the electrons. The width of the depletion region decreases with increasing dopant concentration.

Ideally, the height of the barrier between the metal and the semiconductor depletion region is determined by differences in the work function of the metal and the electron affinity of the semiconductor, which is known as Schottky Mott theory [79, 80]. In the case of Fe/GaAs, the work function, φ_m of Fe is 4.5 eV and the electron affinity of GaAs is 4.1 eV [81]. Therefore, the barrier height should be 0.4 eV. But from the experimental results, it was found to be 0.8 eV, and not dependent on the work function of the metal [23, 81]. The discrepancy in the barrier height occurs due to the pinning of the Fermi level towards the valence band by the surface states in the covalently bonded semiconductors. Surface states are formed due to the dangling bonds at these semiconductor surfaces [80, 81]. The barrier height limits the flow of current in the

reverse bias direction. For heavily doped degenerate semiconductors (where the Fermi energy, E_F is greater than the conduction band energy E_C) the FM/SM contact behaves as an ohmic contact because the width of the depletion region is sufficiently thin that electron tunneling is highly probable and the tunneling current is large. For efficient spin injection, we require tunnelling through a barrier of optimal height and width [48, 82]. The FM/SM interface is an example of such a tunnel barrier when the GaAs is heavily doped (~10^{18} cm^{-3}).

According to thermionic emission theory when a voltage is applied to a rectifying FM/SM interface, the barrier height (ϕ_B) of the contact, can be evaluated from the *J-V* relationship as follows [81],

$$J = A^{**}T^2 e^{-\frac{q\varphi_B}{kT}}\left[e^{\frac{qV}{n_1 kT}} - 1\right], \tag{5.1}$$

where A^{**} is the Richardson constant, T is the absolute temperature, k is the Boltzmann constant, and n_1 is the ideality factor.

The depletion width (W_D) of the FM/SM contact as a function of uniform doping concentration (n) of the semiconductor and at zero applied bias, can be theoretically predicted from [81],

$$W_D = \left[\frac{2\epsilon_r \epsilon_0 \varphi_B}{qn}\right]^{\frac{1}{2}}, \tag{5.2}$$

where ε_r is the relative dielectric permittivity of the semiconductor and ε_o is the permittivity in the vacuum. Fig. 5.1 shows a plot of W_D versus n for a Fe/GaAs contact, calculated using equation 5.2 and $\varphi_B = 0.8$ eV. The values of W_D are 16 and 25 nm for carrier concentrations of 5×10^{18} /cm^3 and 2×10^{18} /cm^3, respectively.

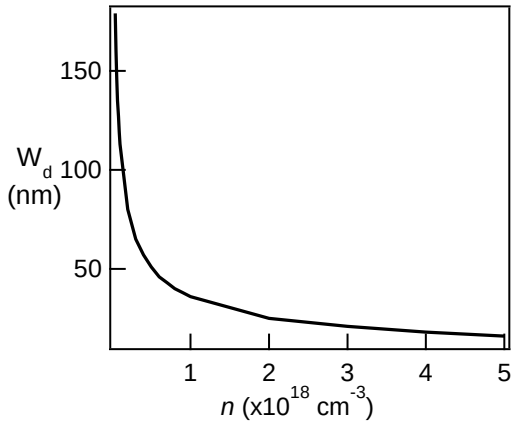

Fig. 5.1. Plot of the theoretically predicted depletion width, W_D using equation 5.2 for zero applied voltage as a function of a uniform doping concentration of GaAs. The barrier height $\boldsymbol{\varphi_B}$ was assumed to be 0.8 eV.

The conduction band profile near the interface provides information about the shape and height of the barrier as well as the position of the GaAs conduction band with respect to the Fermi level. This was calculated by solving Poisson's and Schrödinger's equations using 'Nextnano' simulator software [83]. Such a plot at zero applied voltage for Fe/epitaxial GaAs as a function of GaAs doping concentration 2×10^{18} /cm^3 (black) and 5×10^{18} /cm^3 (blue) is shown in Fig. 5.2. The calculation assumed the GaAs Si-dopant concentration has the profile shown by the dotted red line (right axis) as a function of depth into the GaAs. The maximum concentration was either 2 or 5×10^{18} /cm^3, but only the higher concentration profile is shown. The calculation also assumed a Fe/GaAs barrier height of 0.8 eV independent of the surface doping. Arrows (purple) show the depletion width of 18 nm and 22 nm for 5×10^{18} /cm^3 and 2×10^{18} /cm^3 respectively, based on the depth at which the conduction band (E_C) in the GaAs shows minimum energy. These are similar to the values for W_D when a uniform doping concentration was assumed. In both cases, the widths are confined to within the nominal heavily-doped GaAs region (maximum thickness 30 nm).

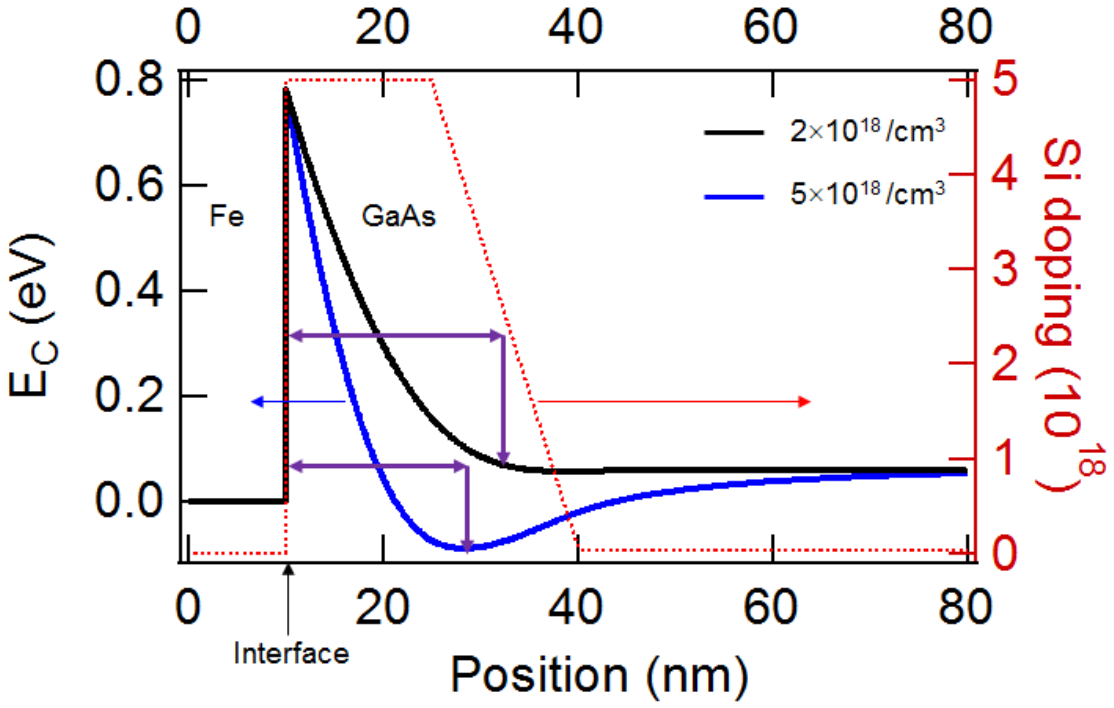

Fig. 5.2. Calculated conduction band (E_C) profiles using 'Nextnano' simulator software as a function of distance for epitaxial GaAs with 2×10^{18} /cm^3 (black) and 5×10^{18} /cm^3 (blue), doped surface layers. The Si dopant concentration profile is indicated by the red dotted line and shown only for the higher doping case. Arrows (purple) indicate the depletion width.

The contact resistivity (ρ_C) at zero bias for the FM/SM contact from a *J-V* plot can be evaluated as follows [81],

$$\rho_C = \left(\frac{dJ}{dV}\right)^{-1}_{V=0} = A_C R_C \ , \tag{5.3}$$

where R_C is the contact resistance and A_C is the contact area. From equation 5.1 and 5.3 one can derive the expression for R_C in the thermionic emission region as [81]

$$R_C = \frac{k}{qA^{**}A_C T}\left[e^{\frac{q\varphi_B}{kT}}\right] \ , \tag{5.4}$$

which is independent of the semiconductor dopant concentration depending only on ϕ_B. Once tunneling dominates the transport, equation 5.4 no longer applies. The ρ_C of FM/SM contacts with a heavily-doped semiconductor can be estimated from Fowler-Nordhiem tunneling theory [84] as follows:

$$\rho_c = \left[\frac{A^{**}T\pi q}{k\sin(\pi pkT)} e^{\frac{-q\varphi_B}{E_{oo}}} - \frac{A^{**}q}{pk^2}\left(e^{\left(\frac{-q\varphi_B}{E_{oo}}\right)-pE_F}\right)\right]^{-1} , \quad (5.5)$$

where

$$p = \frac{1}{2E_{oo}} \ln \frac{4q\varphi_B}{E_F} \quad (5.6)$$

and

$$E_{oo} = \frac{qh}{4\pi}\sqrt{\frac{n}{\epsilon_r m^*_{tun}}} , \quad (5.7)$$

and m^*_{tun} is the tunneling effective mass. E_{oo} is called the characteristic energy related to the tunneling probablity and depends on the electron concentration.

Electrical measurements, current-density versus voltage (*J-V*) were carried out at room temperature (RT) using a computer-controlled (Cascade Microtech 150) probe station capable of measuring ± 100 mA with an applied voltage of up to ± 20 V with a resolution of 5 mV. Two types of diode contacts were measured consisting of ED Fe/bulk-GaAs (0.8 mm diameter) and back-to-back Fe/epi-GaAs spin contacts (8 µm × 50 µm). Hall measurements were carried out on selected GaAs samples to confirm the n-type carrier concentration. The Hall samples (van der Pauw) were made using a standard procedure, consisting of In-alloyed contacts on 4 corners of an area of 5 x 5 mm^2 of GaAs sample.

5.1.1. J-V characteristics

Hall measurements of the MOCVD-grown tunnel structure (2x10^{18} cm^{-3}, sample E1) found a net n-type carrier concentration in the channel of 3.9×10^{16} cm^{-3} within the expected range, (2 – 4) ×10^{16} cm^{-3}. Other epitaxial samples were not checked.

Fig. 5.3 shows *J-V* characteristics as a function of dopant concentration in the semiconductor for tunnel junction contacts electrodeposited onto bulk GaAs (red) or epitaxially-grown MOCVD (blue) or MBE (green) GaAs samples for 0.8 mm diameter diodes measured at room temperature (sample nos: B2-1, B3-1, E1-7, and E2-1). The electrodeposited interfaces follow a rectifying behavior typical of Fermi-level pinned metal-GaAs contacts with barrier heights of 0.8 eV, calculated based on the thermionic emission theory (equation 5.1) for a diode of 0.8 mm diameter of Fe on bulk-GaAs, 3×10^{17} cm^{-3}. By increasing the dopant concentration the semiconductor depletion region narrows and tunneling increases dominating the transport, as is true for vacuum-deposited Fe/GaAs contacts [85-89]. As expected, higher doping concentrations give larger reverse currents relative to the forward current implying greater electron tunnelling.

The *J-V* characteristics of back to back spin contacts of 8 μm × 50 μm Fe bars on epitaxial-GaAs (sample nos: E1-8 and E2-2) are shown in Fig. 5.4. These plots illustrate the effect of the surface doping concentration ($2 \times 10^{18}/cm^3$ or $5 \times 10^{18}/cm^3$) for different pairs of contacts for each type of sample.

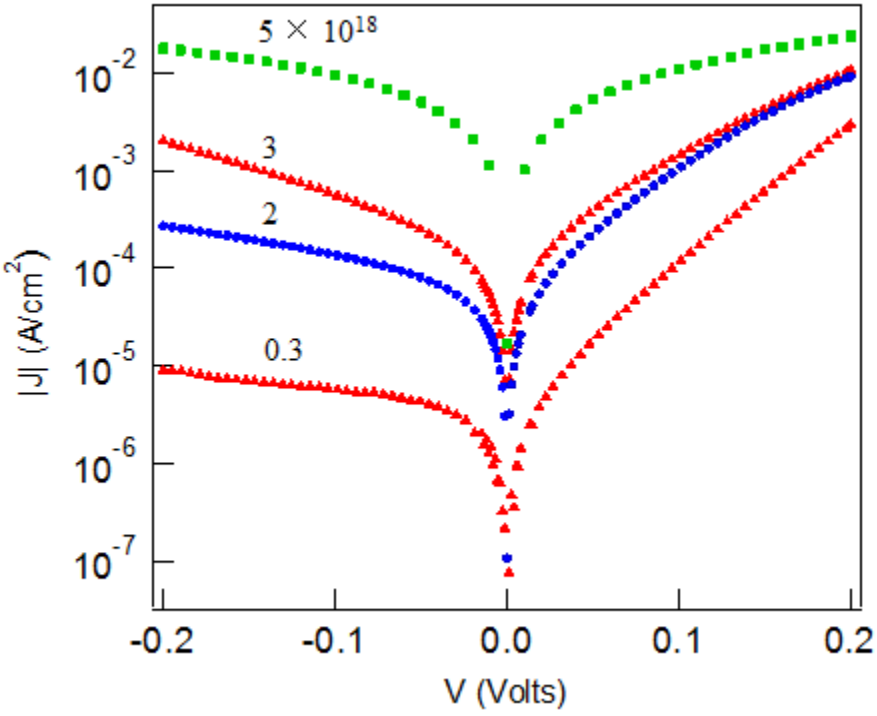

Fig. 5.3. Results from current-density versus voltage characteristics of Fe/GaAs diodes as a function of sample (GaAs) doping concentration, n, and sample type. Fe grown on bulk samples (B2-1 and B3-1) are in red and on epi-GaAs sample (E2-1, E1-7) are in green and blue, respectively, for large area diodes (0.8 mm of diameter).

The schematic of a spin structure is shown in the inset in Fig. 5.4. As expected, a larger forward and reverse current, implying more electron tunnelling across the interface, is obtained for higher doped samples (5×10^{18} /cm^3 open squares, 2×10^{18}/cm^3 solid squares). *J-V* behavior is asymmetric in forward and reverse bias meaning individual Fe contacts are not identical to each other. Resistance at zero bias and at the applied current of 0.1 mA for spin measurements has been calculated for these two samples for contacts 2 and 1 and plotted in Fig. 5.5.

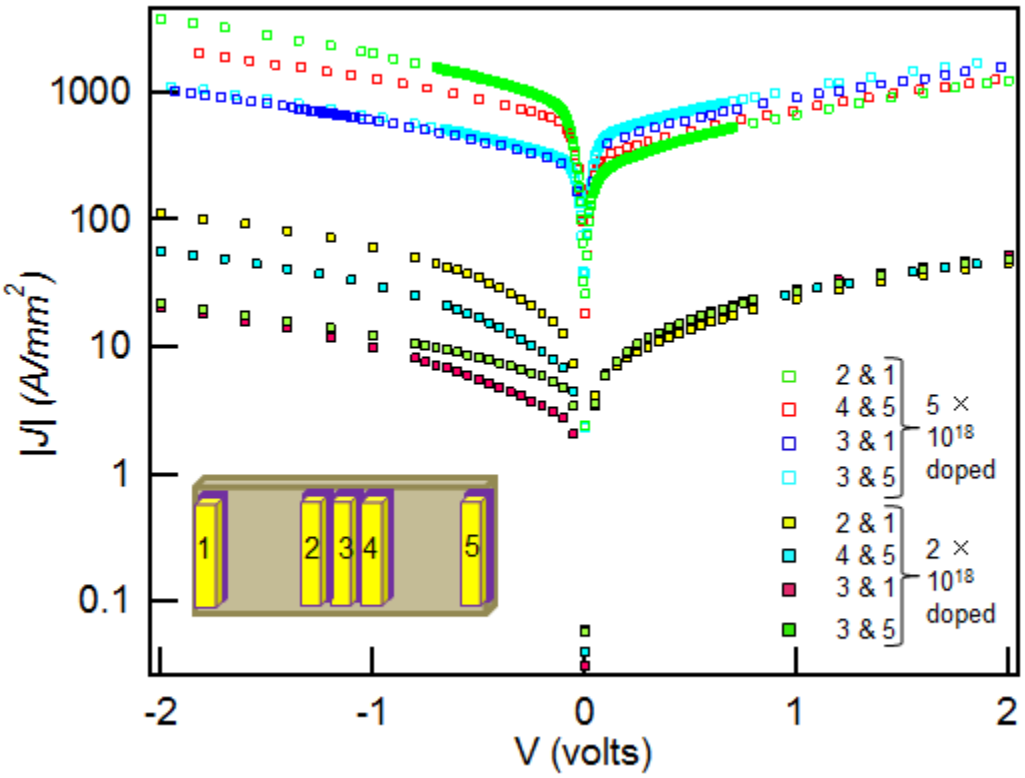

Fig. 5.4. J-V characteristics for back-to-back Fe contacts as a function of sample (GaAs) n-type doping concentration for different contact pairs as shown in the schematic of the spin structure in the inset. (5.0×10^{18}/cm^3, open squares, 2.0×10^{18}/cm^3 solid squares, E1-8 and E2-2, respectively). The larger forward and reverse current indicates that more electrons are tunnelling through the Fe/epi-GaAs(100) interface in the higher doped sample. Plots are asymmetric with respect to zero bias, meaning individual contacts are not identical.

Fig. 5.5 compares the room temperature contact resistance area product RA_o (log scale) at zero bias as a function of doping concentration for large area diodes (triangles) back-to-back spin contacts (circles), with literature data for MBE-grown Fe/epi-GaAs contacts (diamond) measured at 10 K [48]. For the bulk diode sample (3 x10^{17}/cm^3) the RA product was 7600 Ωcm^2, which is smaller than the value 4.6 MΩcm^2 predicted from thermionic emission transport using equation 5.4. This theory assumes no tunneling nor other transport mechanisms including recombination currents.

Recombination at low bias is a commonly reported reason for non-ideal behavior in Schottky contacts. This process would reduce the resistance as we observed.

The *RA* product at the applied current (0.1 mA) during spin measurements for back-to-back contacts is also shown (squares) in Fig. 5.5. For the $2x10^{18}/cm^3$ and $5x10^{18}/cm^3$ epitaxial samples (large area diodes) *RA* at zero bias is 422 Ωcm^2 and 10 Ωcm^2, respectively. We have not directly measured the *J-V* for the corresponding small area spin contacts but the back-to-back contact characteristics show *RA* (zero bias) values of 101 and 0.9 Ωcm^2, respectively. The inset in Fig. 5.5 showing d*I*/d*V* with applied voltage (10 mV to -150 mV) is calculated from Fig. 5.3 data for the $2 \times 10^{18}/cm^3$ doped sample. This conductance shows a parabolic behaviour and the minimum is shifted from zero confirming tunneling [90, 91].

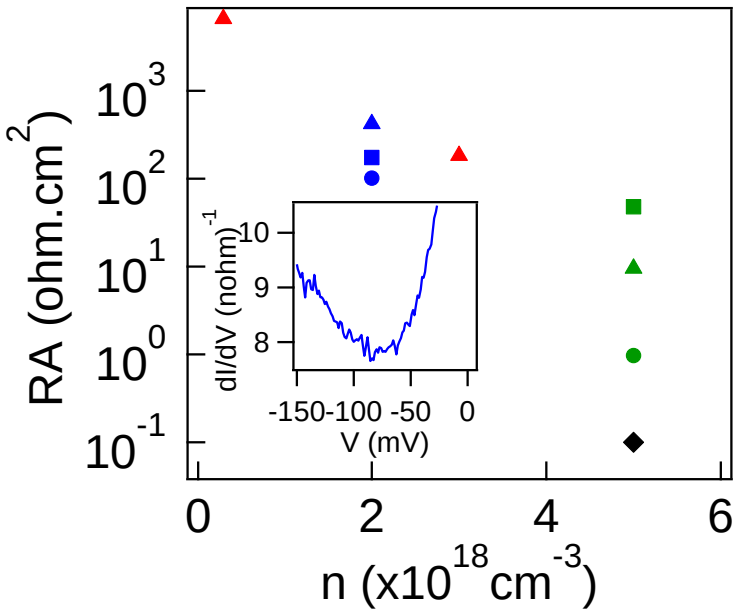

Fig. 5.5. Log plot of contact resistance at zero bias times area, versus *n*, large area diodes (0.8 mm diameter) (triangles); epitaxial back to back spin contacts (8×50 μm^2) (circles) and literature vales for *in situ* MBE Fe/GaAs (diamonds). Also plotted is the RA product at the applied current (0.1 mA) for spin valve measurements of back-to-back spin contacts (squares). The inset is a plot of d*I*/d*V* from the MOCVD epitaxial $2x10^{18}/cm^3$ data in Fig. 5.3.

5.1.2. Summary of results for electron transport

Spin structures of the higher-doped Schottky contacts ($5\times10^{18}/cm^3$) had a 100 times smaller zero-bias resistance compared to the lower doped ($2\times10^{18}/cm^3$) shown in Fig. 5.5 with circles, 0.9 Ωcm^2 versus 101 Ωcm^2 confirming expectations of larger tunnelling currents through the higher-doped samples. However, ED contact resistances for similar doping concentration ($5x10^{18}/cm^3$) are at least 10 times larger than those reported for MBE-grown Fe/GaAs contacts (0.9 versus 0.1 Ωcm^2) even with ours measured at room temperature while their's were at 10 K [48]. This indicates that either the depletion region (22 nm and 18 nm for 2×10^{18} cm^{-3} and 5×10^{18} cm^{-3}, respectively) extended into the channel or that there is a presence of an insulating interfacial layer in the ED contacts.

The exposure of the epi-GaAs surfaces to atmosphere prior to metal deposition meant that a native oxide regrew reducing the thickness of the nominal heavily-doped surface layers by 0.3 – 3 nm, depending on the time and dopant concentration [92]. This would have increased the overall width of the depletion region and hence increased the interfacial resistance. The surface of our GaAs sample was prepared using a native-oxide etch in ammonium hydroxide prior to ED. This process is also known to leave a residual Ga suboxide with excess As whose thickness decreases with increasing substrate doping concentration [93, 94]. Thus, there is also a strong probability that there was a surface oxide layer when the substrate reached the electrolyte. This layer would have reacted with the Fe during ED forming an interfacial oxide layer but nevertheless, could not entirely have inhibited the epitaxial formation of Fe films [23]. A similar phenomenon has been reported for MBE-grown Fe on intentionally-oxidized GaAs [95]. Consistent with the conclusion that there may be an interfacial oxide was data from atom probe tomography that detected 4% oxygen within 8 nm from our Fe on bulk GaAs interfaces [96]. If concentrated at the interface this would represent a 0.5 nm thick layer of a Fe oxide phase such as FeO, a sufficient thickness to contribute a tunnel barrier. However, an interfacial layer greater than 0.2 nm was not detected via cross-section TEM of bulk interfaces. No sulfur was detected by the same atom probe tomography scans although S is present in the electrolyte and is known to adsorb onto GaAs surfaces preventing As interdiffusion [97].

5.2. Spin Transport Theory

In lateral spin transport measurements the spin structures typically consist of several FM/SM tunnel contacts positioned laterally across the substrate, as depicted in Fig. 5.6. In this structure, 5 FM tunnel contacts are connected via a low-doped semiconductor channel. Similar to charge carrier scattering, spin scattering within a semiconductor increases with both dopant or other impurity concentration and temperature. The design of the epi-GaAs structure for spin devices was based on a heavily-doped (> 10^{18} cm^{-3}) surface layer made as thin as possible to reduce spin flipping during tunneling transport between the FM and SM [11, 19]. The magnetic field is applied either in-plane or out-of-plane depending upon whether a spin valve measurement or Hanle measurement is required. Both of these measurements depend on spin diffusion and spin relaxation in the semiconductor channel and crucially on the relative orientation of magnetization of the injector and detector contacts. In addition, Hanle measurements depend on the rate of precession of spins in the semiconductor channel.

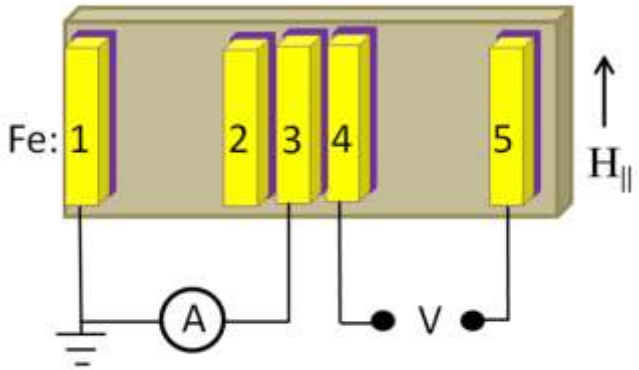

Fig. 5.6. Schematic diagram of a spin structure with 5 lateral Fe/GaAs tunnel contacts (yellow is Fe, purple is n^+-GaAs) patterned onto a lower-doped (10^{16} cm^{-3}) GaAs channel (grey areas).

In a spin valve measurement (field applied in-plane), a change in the non-local spin resistance when the magnetic polarization of one of the contacts is reversed, is a signature of lateral spin transport between FM/SM contacts. Upon application of a bias at one pair of contacts, the other pair develops a potential difference that depends on the spin transport and therefore is expected to change when the in-plane magnetization of a pair of contacts are switched from parallel to antiparallel. Relative magnetic alignment, parallel or antiparallel of a pair of contacts results in a lower or higher resistance, respectively, for a spin polarized electron flow between them. The magnetic alignment, parallel or anti-parallel, of the small contacts is controlled by scanning the applied magnetic field and relies on the fact that one contact will switch prior to the others. In Fig. 5.6, contacts 3 and 4 are used as the injector and detector, respectively. A schematic plot of the expected spin voltage signal measured between contacts 4 and 5 versus forward and reverse sweeps of the magnetic field is shown in Fig. 5.7. Changes in the voltage occur when there is a relative change in the magnetization directions (spin orientation) of the contacts 3 and 4 from parallel to anti parallel.

In a lateral spin valve measurement, a constant DC current is applied between two lateral contacts, one called the injector and the other a remote contact spaced a distance that is larger than the spin diffusion length in the semiconductor, λ_D, for example, contacts 3 and 1, Fig. 5.6, respectively. The current is considered to be positive when the electrons move from the metal into the semiconductor at the injector contact, and vice versa for negative. An in-plane magnetic field sweeps in reverse and forward directions while the voltage between the detector contact 4 and a second remote contact 5 is measured. The detector contact is spaced less than λ_D, from the injector.

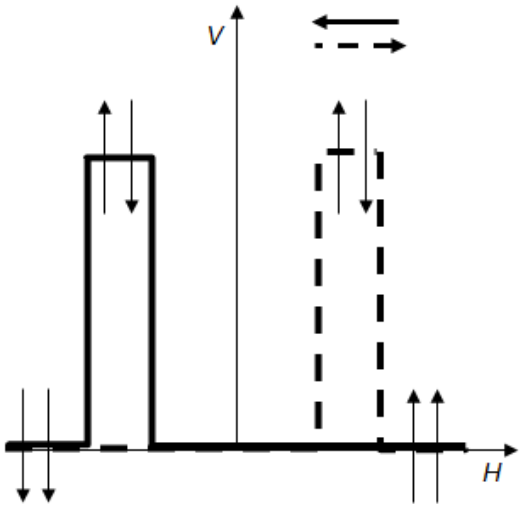

Fig. 5.7. A schematic diagram of the expected voltage signal detected between contacts 4 and 5 (in Fig. 5.6) as a function of forward and reverse sweep directions of the magnetic field, H. Arrows on the plot represents the spin orientation of the injector and detector (↑↑ parallel and ↑↓ antiparallel). The horizontal arrows indicate the sweep direction of the magnetic field.

If a spin polarized current is injected at the injector, there is little chance that any polarized electrons will reach the remote contacts without spin relaxation. The applied current flows in only one direction, whereas, polarized electrons diffuse in all directions, including away from the applied current, at the point of injection at the FM/SM interface, following the diffusion equation [98]:

$$\nabla^2 \delta P = \frac{\delta P}{\lambda_D{}^2}\,, \tag{5.8}$$

where δP is the spin accumulation in the semiconductor channel underneath the Fe/GaAs tunnel barrier. λ_D is related to the spin diffusion constant (D) and average spin life time (τ_S, or average spin scattering time) by

$$\lambda_D = \sqrt{D\tau_S}\,. \tag{5.9}$$

The spin polarization in the GaAs, P_{GaAs}, can be defined as [11]

$$P_{GaAs} = \frac{n_\uparrow - n_\downarrow}{n_\uparrow + n_\downarrow}, \tag{5.10}$$

where $n_\uparrow$ and $n_\downarrow$ are the densities of spin-up and spin-down electrons, respectively. Depending upon the relative magnetization of the injector and detector FM contacts, a voltage appears as a difference in the electrochemical potential, $\Delta\mu$, at the detector with respect to a remote reference contact expressed as [48]:

$$\Delta\mu = \frac{n_\uparrow - n_\downarrow}{\left(\frac{\partial n}{\partial E}\right)}, \tag{5.11}$$

where E is the energy, n is the channel doping concentration and assuming Δn is very small so that $\Delta\mu/e$ is small compared to the Fermi energy of the semiconductor channel. $\frac{\partial E}{\partial n}$ can be calculated from the Fermi energy, E_F, of the GaAs based on the free electron gas model, expressed as [48, 99],

$$E_F = \frac{\hbar^2}{2m^*}(3\pi^2 n)^{\frac{2}{3}}, \tag{5.12}$$

where m^* is the effective mass and $\hbar$ is the reduced Planck's constant. E_F of GaAs ($n = 4 \times 10^{16}$ cm^{-3}) is 10 mV. For parallel magnetic alignment of injector and detector contacts, there will be a lower spin resistance path as compared to the anti-parallel alignment. The detected voltage depends on the spin polarization at the detector contact, a phenomenon called spin magneto-resistance. The net voltage difference (ΔV) at the detector is proportional to the change in chemical potential ($\Delta\mu$) which can be calculated from equations, (5.11) and (5.12) as [48],

$$\Delta V = \frac{\Delta\mu e^{-L/\lambda_D}}{e} = \frac{2}{3}\frac{\hbar^2}{2em^*}(3\pi^2 n)^{\frac{2}{3}} P_{GaAs} e^{-L/\lambda_D}, \tag{5.13}$$

where L is the distance between the injector and detector contact. With L = 2 μm, λ_D = 10 μm, if we assume that only one kind of spin polarity (up or down) exists then the maximum theoretical ΔV detectable for Fe/GaAs is 10 mV at 10 K.

For further verification of spin transport at the detector, one needs to conduct a Hanle measurement. Here, application of an out-of-plane magnetic field induces spin precession and eventually destroys the in-plane spin orientation. The measurement

condition is otherwise the same as for the spin valve measurement. The polarized spins start to precess around the out-of-plane magnetic field, and eventually with increasing field, the spin polarization decays completely. The spin polarization at the detector as a function of the applied field, H, and x_1 and x_2, the widths of the injector and detector contacts, respectively, can be expressed as [11]:

$$P_{Spin}(H, x_1 x_2) = \left(\frac{P_{inj}\, P_{det}}{2}\right)\left(\frac{2D\rho}{A}\right) I \int_{w_1}^{w_2}\int_{w_3}^{w_4}\int_0^{\infty} \frac{e^{-(x_2 - x_1 + v_d t)^2/4Dt}}{\sqrt{4\pi D t}} \times e^{-t/\tau_s} \times \cos\left(\frac{g\mu_B Ht}{\hbar}\right) dx_1 dx_2 dt \ , \quad (5.14)$$

where P_{inj} and P_{det} are the spin polarizations at the injector and detector, respectively, A is the channel cross-sectional area, ρ is the resistivity of the GaAs channel, g is the electron g-factor in GaAs, and v_d is the spin drift velocity. The first term in the integral arises from the diffusion of spin-polarized electrons at the interface and in the semiconductor channel. The second term is the spin relaxation due to scattering and the third describes the spin precession around the applied field. In the absence of perturbations in the applied field, from local magnetic fields at the interface, the width of the Hanle signal is directly proportional to the spin lifetime. A local magnetostatic field can develop due to magnetic impurities or the finite roughness of the ferromagnetic contact. This local field interferes with the spin precession rate and broadens the Hanle signal. As mentioned in the introduction (Chapter 1) several groups have reported this impurity and finite roughness effect [33, 35].

So far we have been discussing four terminal (4-T) measurements, spin valve and Hanle. Measurements are often also carried out using only three terminal contacts (3-T). The above theory is unchanged. The 3-T Hanle measurements reveal the spin accumulation at any individual spin contact. To perform 3-T Hanle measurements, three FM/SC contacts are placed at large distances ($\gg \lambda_{D,}$ spin diffusion length) from each other, such as contacts 1, 3, and 5 in Fig. 5.6 redrawn in Fig. 5.8. Now, the centre contact (contact 3) acts as both the spin injector and detector while the other two are reference contacts [30-35]. Under a positive applied current between contacts 1 and 3, spin polarized electrons flow from the metal contact into the semiconductor through the interface at contact 3. Simultaneously, an out-of-plane magnetic field is swept in the forward and reverse directions. A measurement of the voltage difference, $\Delta V,$ between

the contact 3 and the contact 5, as a function of an applied perpendicular magnetic field, $H_{\perp}$ will reveal any spin accumulation in the semiconductor just below the injection contact. Spin accumulation is a maximum at zero applied field. As the applied field increases, the spins of the polarized electrons start to precess around it at the interface and de-phase completely at a certain field magnitude. The behavior follows a Lorentzian line shape – called the Hanle effect [31],

$$\Delta V(H) = \frac{\Delta V(0)}{1+ (\omega_L \tau_S)^2} \ , \tag{5.15}$$

where ω_L is the Larmor frequency. The width of this Lorentzian line is inversely proportional to τ_S [33]. The shape of the 3-T Hanle signal (like the 4-T Hanle) is very sensitive to any inhomogeneous local magnetic fields at the interface perhaps due to magnetic impurities and/or roughness at both the surface and interfaces of the FM contacts [35]. Magnetic impurities and inhomogeneities can be detected from a comparison of τ_S extracted from 3-T and 4-T Hanle plots fit using equations 5.14 and 5.15 [31].

The spin resistance area $(RA)_{spin}$, or amplitude of the voltage signal divided by applied current multiplied by the contact area, calculated from Hanle plots can be compared with theoretically expected values. Theoretical calculations for a free electron gas model in the diffusive regime in the degenerate semiconductor give [19, 31, 100]:

$$J_S = \frac{e(n_\uparrow - n_\downarrow)}{\tau_S} \tag{5.16}$$

$$r = \gamma^2 \frac{\Delta\mu}{eJ_S} \tag{5.17}$$

$$D = \frac{\mu_e n}{e\frac{\partial n}{\partial E_F}} \tag{5.18}$$

$$\frac{1}{\rho} = ne\mu_e \quad , \tag{5.19}$$

where r is the spin resistance density, J_S is the applied current density, ρ is the resistivity of the semiconductor channel, γ is the tunneling spin polarization, and μ_e is the electron mobility.

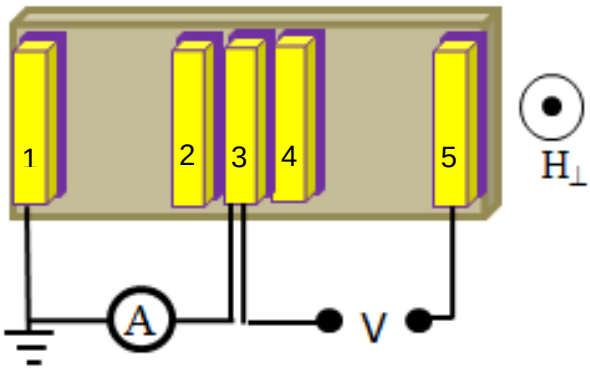

Fig. 5.8. A schematic diagram of a 3-T Hanle measurement showing the electrical connections. Spin accumulation occurs at the Fe contact 3.

From equations 5.11, and 5.16 - 5.19, (with similar assumptions applied as for the case of lateral spin valve theory, that is, the value of the spin polarization is small) the magnitude of the resistance area product, *RA,* can be derived as follows:

$$RA = \frac{\rho(\gamma \lambda_D)^2}{s}, \tag{5.20}$$

where λ_D is the spin diffusion length, and *s* is the thickness of the channel assuming *s* is smaller than λ_D. Comparison of these theoretical and experimental values test whether the spin injection is happening directly into the semiconductor channel for a particular FM/SM contact or via some other parallel process such as localized interface states [18, 19, 31].

Inverted Hanle data for individual contacts further distinguishes the potential effects of magnetic in-homogeneities from impurities at the interface or the surface of the ferromagnetic bar. Techniques for inverted Hanle are very similar to 3-T Hanle, except the sweeping magnetic field is in-plane instead of perpendicular to the ferromagnetic contacts. Under reverse bias, spin polarized electrons start to diffuse at the interface from the FM into the semiconductor in all directions. Just like 3-T Hanle, this method measures the spin accumulation in terms of a voltage difference between the injector

contact and the reference [35, 101]. One should expect a voltage minimum (but not the zero or maximum voltage) at zero field because there is a net magnetic field arising due to the magnetic inhomogeneities along the perpendicular direction to the contact plane. These inhomogeneities may play a dominant role in spin precession under zero applied field. Increasing the in-plane magnetic field reduces the effect of any out-of-plane local magnetostatic fields by rotating the magnetization along the length of the bar. Very large in-plane fields align the magnetization along the length of the bar, and as a result spin precession due to local magnetic fields falls to zero and the accumulation of spin-polarized electrons in the semiconductor underneath the injector contact will be a maximum. The measured spin signal is opposite to that of the 3-T Hanle. Inverted Hanle is observed only for spin contacts with magnetic in-homogeneities.

5.2.1. Spin Valve and Hanle Measurement Techniques

Two types of spin measurements were performed: non-local lateral spin valve (NLSV) and Hanle. In each case, the fabricated sample was glued with epoxy and wire bonded onto an electronic dual in line package (DIP), which was then attached to a quartz piece using high-vacuum glue. The whole assembly was mounted onto a special sample holder (90 cm) which was inserted vertically into a liquid He-cryostat placed in the middle of an electromagnet. Fig. 5.9 shows a schematic diagram of the cryostat [102]. The sample could be rotated inside the cryostat to obtain the desired direction of the field (in-plane or out-of-plane) by rotating the sample mounting rod clockwise or anti-clockwise. As mentioned, the 16 pin connector attached to the sample holder was used to connect the power supply and the nano-voltmeter to the spin device structure. The cryostat consists of concentric chambers (containing: sample, liquid He, liquid nitrogen, and an outer vacuum jacket) and could be used with either liquid He (down to 4 K) or liquid nitrogen (down to 77 K). There was a valve between the He and the sample chamber to flow liquid He to the sample compartment. The evacuation valve was used to evacuate the outer chamber of the cryostat to reduce heat loss. Isolation tubes and the radiation shield were also used to control heat loss during measurements using liquid He. An 8 pin connector between the heater and the GaAlAs diode temperature sensor and the temperature controller, was attached to the sample holder.

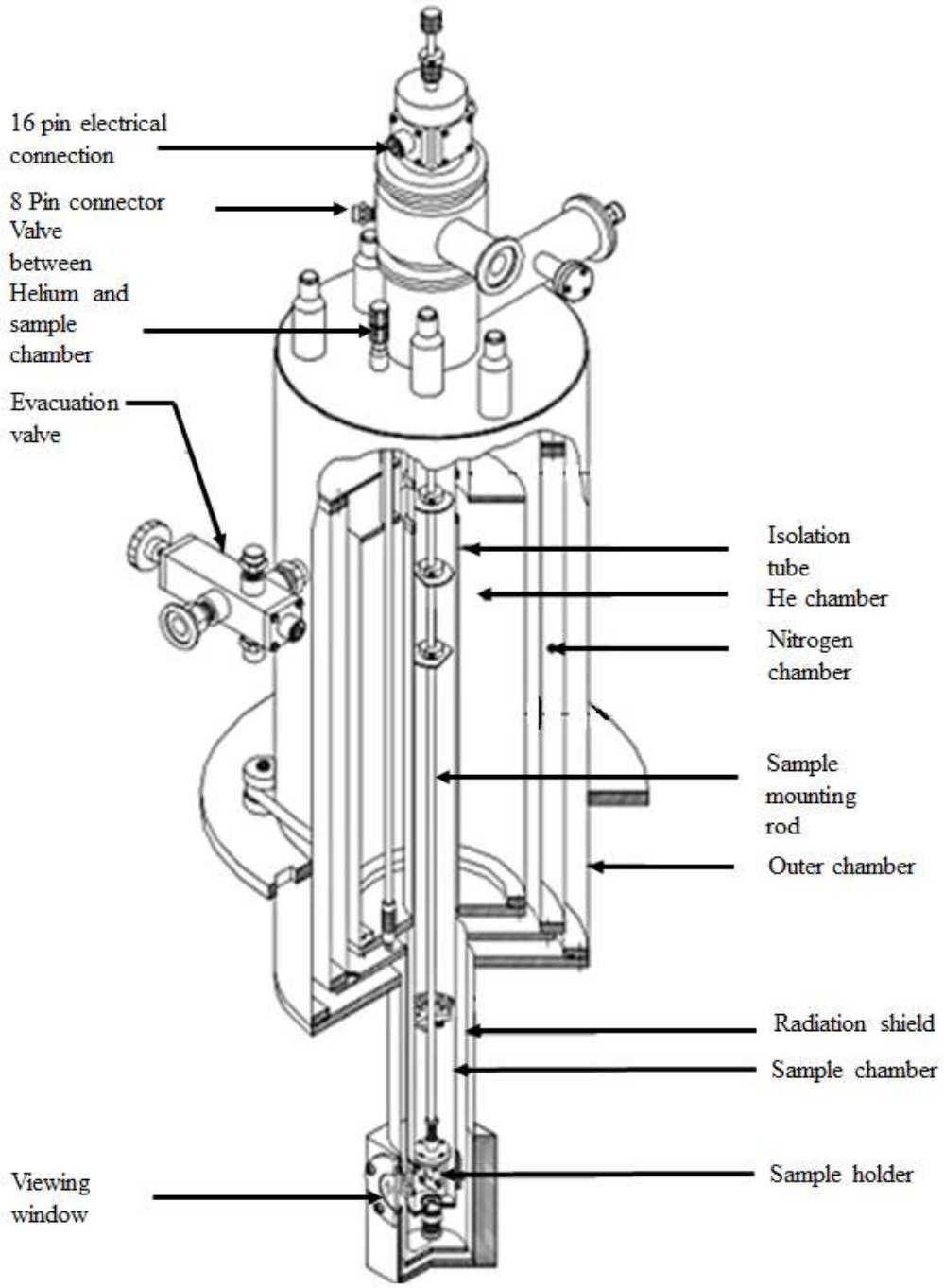

Fig. 5.9. Diagram of the He cryostat used for the spin valve and Hanle measurements [102].

A temperature equal to that of liquid N_2 at atmospheric pressure (77 K) was maintained by continuously filling fresh liquid nitrogen into the He chamber and pumping out the outer vacuum jacket of the cryostat. For cooling with liquid He, the He, sample and outer vacuum chambers were first evacuated to prevent the development of an ice blockage between He and the sample chambers at the valve at low temperature (4 K). The outer vacuum jacket provides heat insulation from the outside environment. The cryostat was then cooled to 140 K by first filling liquid N_2 into the liquid N_2 chamber. This reduced the rate of subsequent He evaporation. Then the He chamber was filled with liquid He. Liquid He was introduced into the sample chamber by opening the valve indicated at the top in Fig. 5.9. The sample temperature was maintained at the required point by heating the sample inside the cryostat while very slowly pumping or venting the evaporated He gas. A fixed temperature to within $\pm$ 0.5 K was feasible. Spin transport measurements were carried out at temperatures ranging from 10 K to 140 K in He gas. Some measurements were also carried out using liquid N_2 at 77 K due to its simpler arrangement.

Fig. 5.10 shows a photograph of the bottom part of the 90 cm long sample holder (a) and the electronic chip assembly of the sample (b). There are a total of 16 pins on the holder but only 4 pins were necessary (two from each side) to connect the power supply and the nano-voltmeter to 4 Fe contact bars. Fe bars were connected to the electronic chip via gold wire bonding. The pins mate to the 16 pin connector on the cryostat (Fig. 5.9). A constant current supply (Keithley 220) (capable of producing 1 nA to 100 mA with a resolution of 2 pA to 50 μA) was used as a power source. A nano-voltmeter (Keithley 182) with an impedance of 10 GΩ, resolution 10 nV, range 30 mV was used to detect spin voltage. A heater (output of 50 Watt with 1 A and 50 V for 50 Ω) and a GaAlAs resistive temperature sensor (resolution of 0.01 K when < 30 K and 0.09 when > 30 K) was attached to the sample holder next to the sample. These were used in conjunction with a proportional integral derivative (PID) temperature controller to maintain the sample at a fixed temperature inside the cryostat.

The in-plane or out-of-plane magnetic field was generated by an electro-magnet (Bruker controller) which could produce variable-fields between 0 and 2.3 Tesla with a resolution of 50 mGauss. The field controller attached to the electromagnet did not provide an exact zero field during reverse field sweeping. There was also a provision to use an additional permanent magnet (10 Gauss to 100 Gauss) to apply in-plane and out-

of-plane fields together by placing it perpendicular to the existing electromagnet pole pieces.

All these instruments, except the temperature controller, were automated via a GPIB interface to a computer. The power supply and nano-voltmeter were connected electrically via triax cable to the sample. Fig. 5.11 shows a schematic of the electrical and GPIB connections between the sample and the computer to the different instruments described. A LabView program was designed specifically for automation of the Keithley power supply, nano-voltmeter and magnetic field controller. The sample temperature was recorded manually from the front panel of the temperature controller.

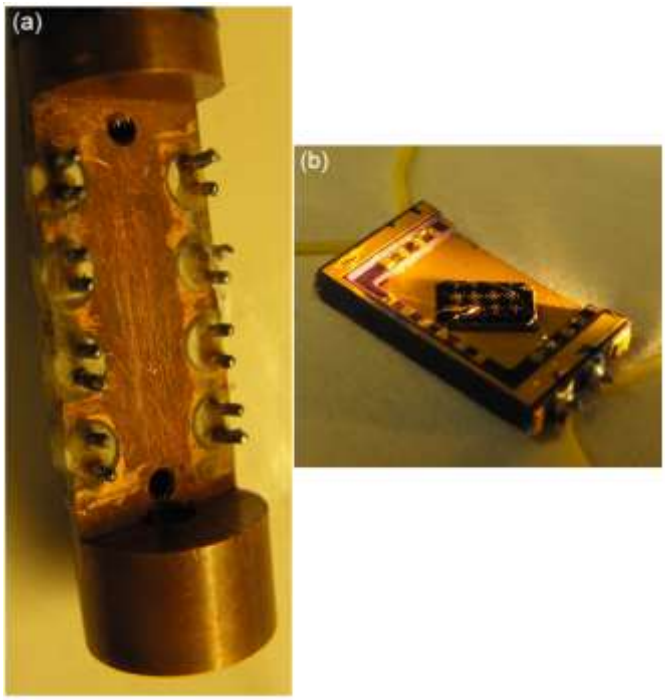

Fig. 5.10. Picture of (a) the sample holder (length: 4.5 cm, diameter: 1.5 cm) for the cryostat with (b) a sample chip (0.8 cm $\times$ 1.2 cm) assembly connected to 4 pins on the holder. This sample holder was attached to a rod (90 cm).

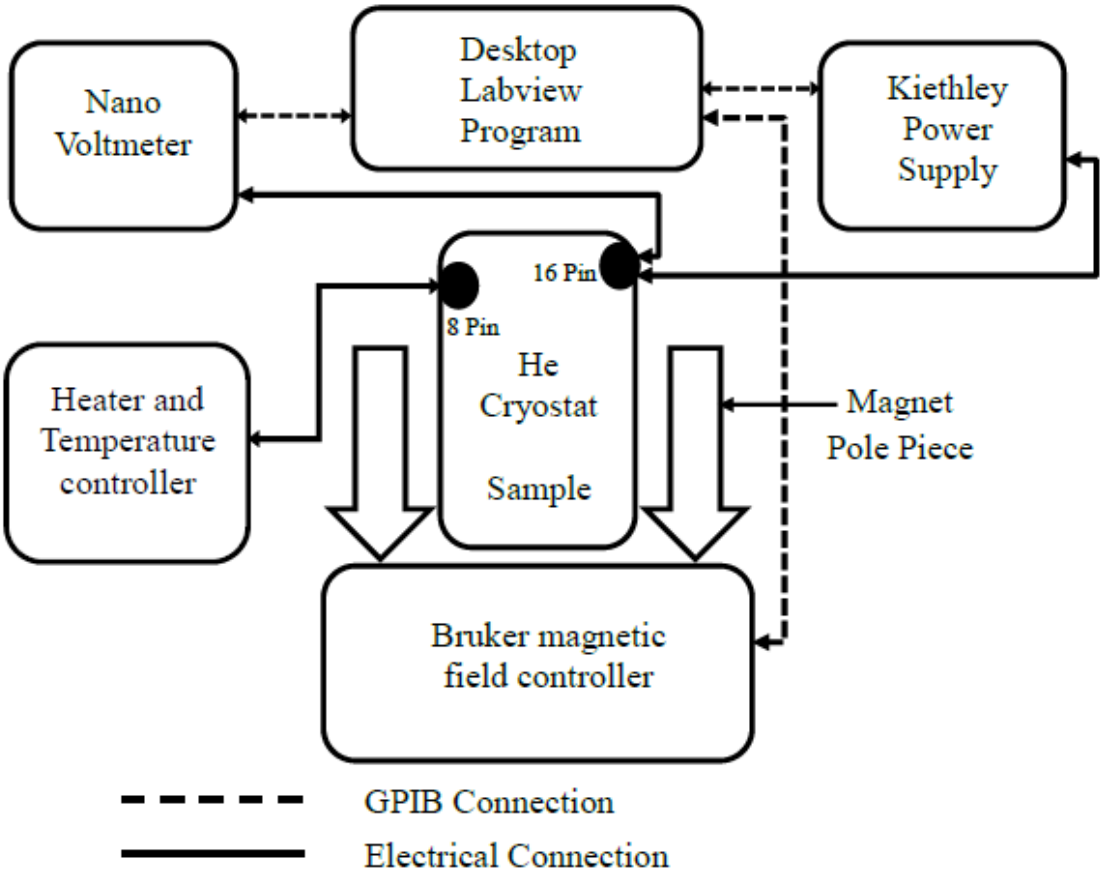

Fig. 5.11. Block diagram of the experimental set up for spin measurements consisting of a sample holder inserted in a He-cryostat placed in the middle of the electromagnet pole pieces. The temperature is recorded manually using a proportional integral derivative (PID) temperature controller via a GaAlAs diode sensor attached to the sample holder. A heater is electrically connected to the sample holder. A Keithley 220 and 182, power supply and nano voltmeter, respectively, are connected to the sample holder. The magnetic field controller, power supply and nano voltmeter are automated through a GPIB interface to a computer via a LabView program.

The spin valve and Hanle measurements were performed using the same device structure but with different electrical configurations as shown in Fig. 5.12. For both spin valve and Hanle measurements, polarized electrons flow from the Fe into the GaAs at the injector bar (positive current) while a magnetic field is swept between forward and reverse direction starting from zero.

Fig. 5.12 shows the connections used for spin valve measurements (a) 4-T and for Hanle measurements (b) 3-T and (c) 4-T. The detection points for voltage measurements vary for the different configurations. The nonlocal 4-T measurements were performed with four contacts. For all configurations the Fe bar attached to the negative current terminal is called the spin injector. The spin detector is the bar adjacent to the injector connected to a voltage terminal, except for the case of the 3-T Hanle configuration where both injector and detector use the same bar at the center.

For 4-T (Fig. 5.12 (a)), the voltage and current paths are completely separated; so, the voltage peak is not directly impaired by any spurious effects in the current path, but a background voltage may also result from the channel resistance.

For a 3-T Hanle measurement, current is applied between one contact in the center (used for both injector and detector) and one outer contact, and voltage is measured between the injector and the other outer contact (Fig. 5.12 (b)). The current and voltage paths are not completely separate from each other leading to a background signal from the applied current. For 4T Hanle (Fig. 5.12 (e)) current and voltage terminals are connected in the same manner as 4T NLSV but the applied magnetic field is perpendicular to the plane of the substrate.

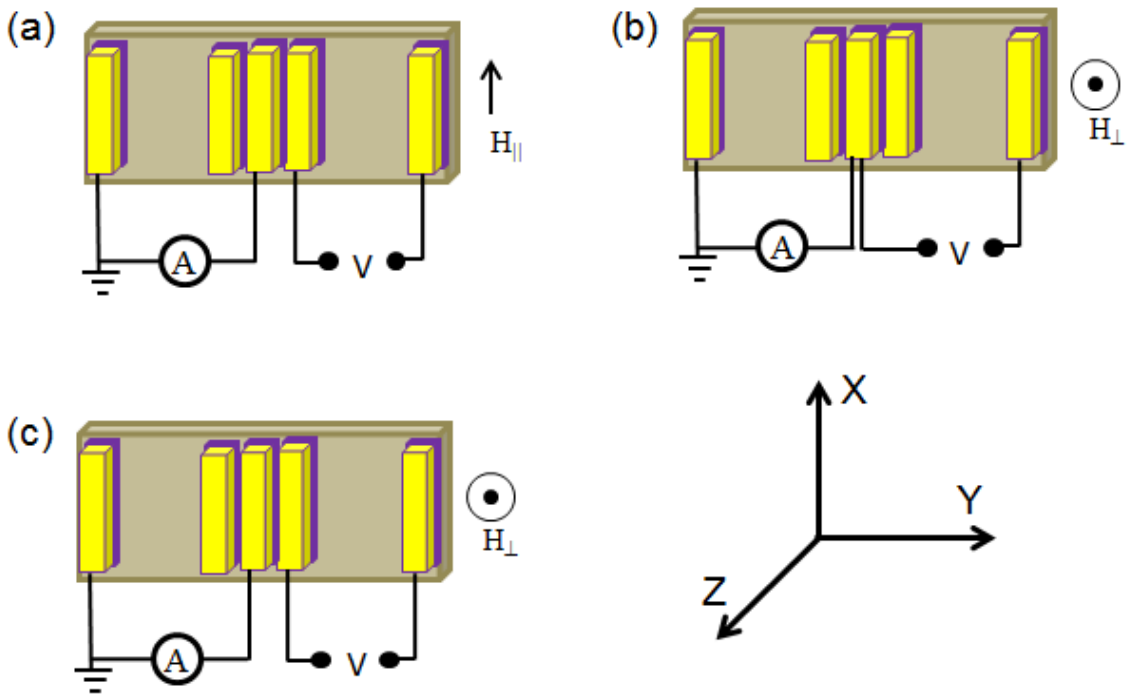

Fig. 5.12. Sample connections used for spin transport measurements for spin valves using (a) four terminals (4-T) and for Hanle with (b) 3-T and (c) 4-T. The direction of the magnetic field with respect to the plane of the sample is indicated.

5.2.2. Results from spin measurements

In the following sections, the lateral non-local spin valve (NLSV) and Hanle transport measurements using ED Fe/epi-GaAs(001) contacts are described for two tunnel-barrier doping concentrations.

5.2.2.1. Lower doped sample (Fe on sample E1) (2×10^{18} /cm^3)

5.2.2.1.1. NLSV

Sample E1-8 consisting of several spin structures, has been used for all NLSV measurements for the lower doped case. Fig. 5.13 is a plot of the voltage at the detector contact using the 4-T NLSV configuration (Fig. 5.9 (a)) and sample E1-8(structure 1) versus the in-plane magnetic field, *H* applied along the length of the Fe bar, (± 160 G along the X axis, an in-plane <100> easy axis) with an applied current 100 μA (electrons flow from Fe into GaAs) at RT. A linear background of 0.3 mV and a quadratic

background were subtracted from the raw data. No peak was found with forward (blue) and reverse (red) field sweep at room temperature. Overall voltage fluctuation is on the order of ± 1μV.

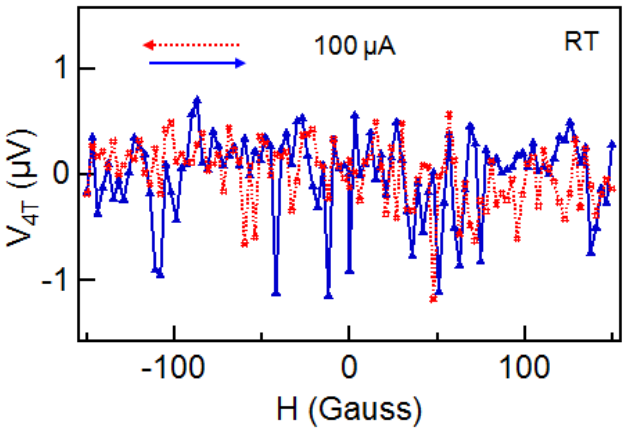

Fig. 5.13. Voltage versus in-plane magnetic field, H, from a single sweep, applied along the length of the Fe bar, with an applied current 100 μA (electrons flowing from Fe into GaAs) at RT using sample E1-8(structure 1). Forward and reverse direction of H-field changes are indicated by blue and red lines, respectively.

Fig. 5.14 is a plot of the voltage versus the in-plane magnetic field, *H,* as a function of current (a) 100 μA and (b) -100 μA at 77 K using sample E1-8(structure 1). The forward and reverse directions of field are indicated by blue and red lines, respectively. Data was taken from only a single sweep with a total sweep time of 2 - 4 hours, depending on the value of the maximum field. The dwell time at each field value was 500 ms. A linear background voltage due to overall resistance fluctuations at low temperature of 18 mV has been subtracted from the raw data. This background varies with the resistance of the sample and contact wires. A quadratic background voltage subtraction has also been performed from all raw data for spin valve and Hanle measurements. These background voltages occur due to non-uniform charge distribution in the GaAs channel in the applied magnetic field [48, 103].

For the positive current direction (electrons flowing from Fe into the GaAs at the injector contact) a spin voltage of 0.8 ± 0.1 mV (peak 1) is detected in the forward field

sweep direction, and a small peak near -150 Gauss, 0.1 ± 0.1 mV (peak 2) in the reverse direction. The data in reverse field direction was offset by 0.2 mV for clarity. In (b) for a negative applied current (polarized electrons moving from GaAs into Fe at the injector contact), the spin voltage is larger with multiple peaks, from 2 to 4 mV in amplitude for forward (peak 1) or reverse sweep (peak 2). The peak positions are asymmetric with respect to the nominal zero field position. There are possibly two reasons for this. Our electromagnet has trouble switching direction and is often not actually at zero field with zero current applied. This implies a relaxation time that varies with the cycle. Such asymmetries observed in the spin valve voltages as a function both of the current direction and magnetic field sweep direction are commonly reported by others [104-106]. Reference measurements using non-magnetic contacts have not been performed.

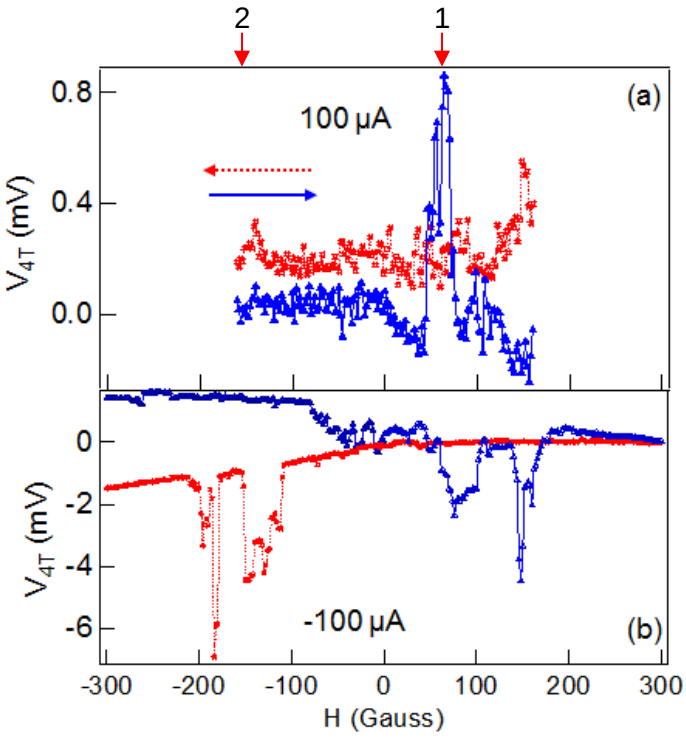

Fig. 5.14. Voltage versus in-plane magnetic field, *H*, from a single sweep, as a function of current direction (a) 100 μA (electrons flowing from Fe into GaAs) and (b) -100 μA at 77 K using sample E1-8(structure 1). Forward and reverse direction of *H*-field changes are indicated by blue and red lines, respectively.

Fig. 5.15 shows another example of spin voltage from the sample E1-7 (linear background voltage of 4.5 mV subtracted) with an applied current of +100 μA at 77 K and a sweeping field applied (a) parallel to the width and (b) along the length of the Fe bars. In (a) two peaks are detected one in the forward and reverse directions, with values of 8.0 and 2.5 ± 0.5 mV, respectively. The data for reverse field sweep is offset by 2 mV for the clarity. Fig. 5.15 (b) shows peaks of values of 4 ± 0.5 mV and 2.5 ± 0.5 mV, for forward and reverse fields, respectively. Overall, there is a small fluctuation in the voltage signal in both (a) and (b).

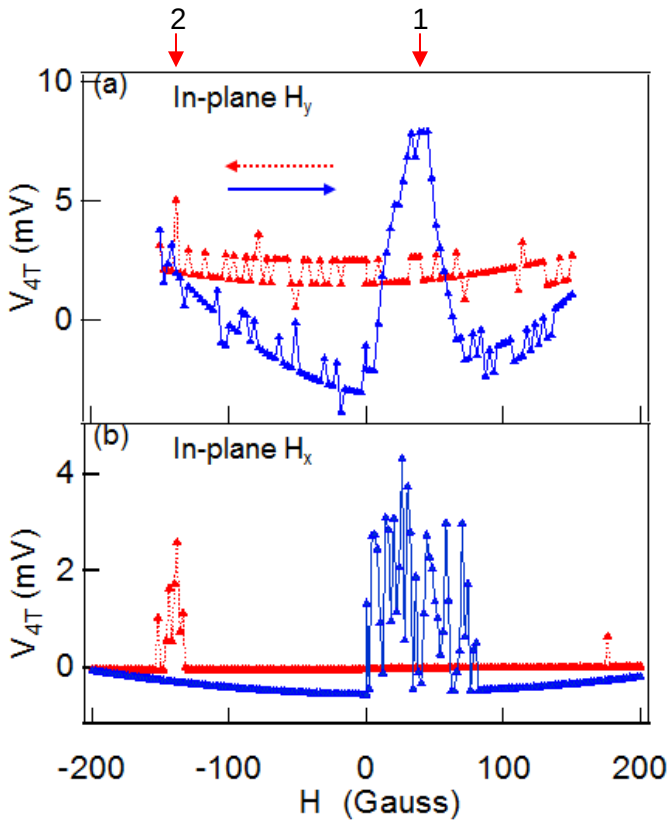

Fig. 5.15. Voltage versus magnetic field from a 4-T NLSV measurement using sample E1-7 with a positive current of 100 μA at 77 K for an applied in-plane field along (a) the width of the Fe bar and (b) the length of the Fe bar. The peak amplitudes at 50 G and -150 G in the forward and reverse field directions respectively are similar in value.

Fig. 5.16 shows plots of voltage versus applied magnetic field measured at temperatures (a) 30 K and (b) 40 K using sample E1-8(structure 1). Voltage peaks are indicated by arrows and labelled for forward and reverse field as 1 and 2, respectively. A linear background voltage of 18 mV has been subtracted from the raw data. The signal to noise ratio is decreasing with decreasing temperature. Fig. 5.16 (c) displays a plot of peak voltage (peak 1) as a function of temperature. The voltage signal decreases with increasing temperature as expected.

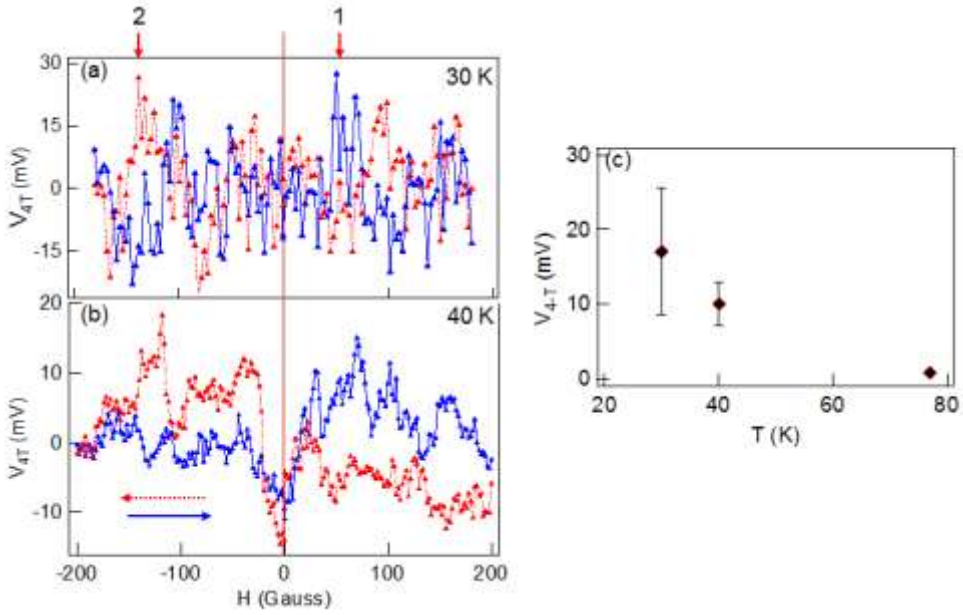

Fig. 5.16. Plot of voltage versus applied in-plane magnetic field, H, measured at a temperature of (a) 30 K and (b) 40 K using sample E1-8(structure 1). A current of 100 μA was applied. Forward and reverse directions of H-field sweeps are indicated by solid blue and red dotted lines, respectively. Voltage peaks are labelled for forward and reverse field as 1 and 2 respectively. Fig. 5.16 (c) shows a plot of amplitude of the voltage signal (peak 1) as a function of temperature displaying a decrease with increasing temperature. The error bars are calculated from the standard deviation of the noise from the signal.

5.2.2.1.2. Hanle measurements

All 3-T Hanle measurements for the lower doped case have been done using sample E1-8(structure 2). Fig. 5.17 shows plots of voltage versus applied out-of-plane magnetic field (a) different applied currents at 65 K and (b) different temperatures with

an applied current of 100 μA using a 3-T Hanle configuration without applying any in-plane magnetic field. All data are offset for clarity. A background voltage was subtracted from each plot which depends quadratically on the applied magnetic field. This voltage is proportional to magneto resistance that occurs due to the non-uniform current density in the semiconductor channel within the applied field [48, 103]. The applied current is defined to be positive when electrons flowed from Fe into GaAs at the injector contact. Peaks that depend on the direction of applied current are observed at zero field. The data collected with a positive (negative) applied current, resulted in a positive (negative) voltage peak.

The amplitude of the voltage peaks are plotted in Fig. 5.17 versus (c) applied current and (d) temperature. These plots show that the voltage signal decreases with increasing temperature and it is almost constant with increasing current in the positive direction. The τ_s, found from fits to the Hanle plots using equation 5.15, ranged between 8.5 ± 0.4 ns to 1.8 ± 0.4 ns, for 20 K to 148 K, decreasing with temperature increase. One such fitting example is shown in Fig. 5.18 (a) for a measurement at 65 K with an applied current of 100 μA. $(1/\tau_s)^2$ has been plotted with temperature in Fig. 5.18 (b) giving a slope of 0.0018 ± 0.0005 $ns^{-2}K^{-1}$.

Fig. 5.19 (a) shows plots of voltage versus applied out-of-plane magnetic field for temperatures of 20 K, 80 K, 90 K and 150 K obtained using the 3-T Hanle configuration and sample E1-8(structure 2). An additional in-plane magnetic field of 30 Gauss was applied along the length of the Fe bars. This modified the net magnitude and the direction of the magnetic field. Fig. 5.19 (b) is a plot of voltage peak amplitude from Fig. 5.19 (a) versus temperature. The peak voltages decreases from 10 mV to 3 mV over the temperature range 20 K to 150 K. The FWHM of the Hanle plots increases from 25.4 Gauss to 96.8 Gauss at 20 K due to an applied in-plane magnetic field of 30 Gauss. This is the expected behavior and is a further indication of the existence of effects of local magnetic fields from a multiple domain structure [106].

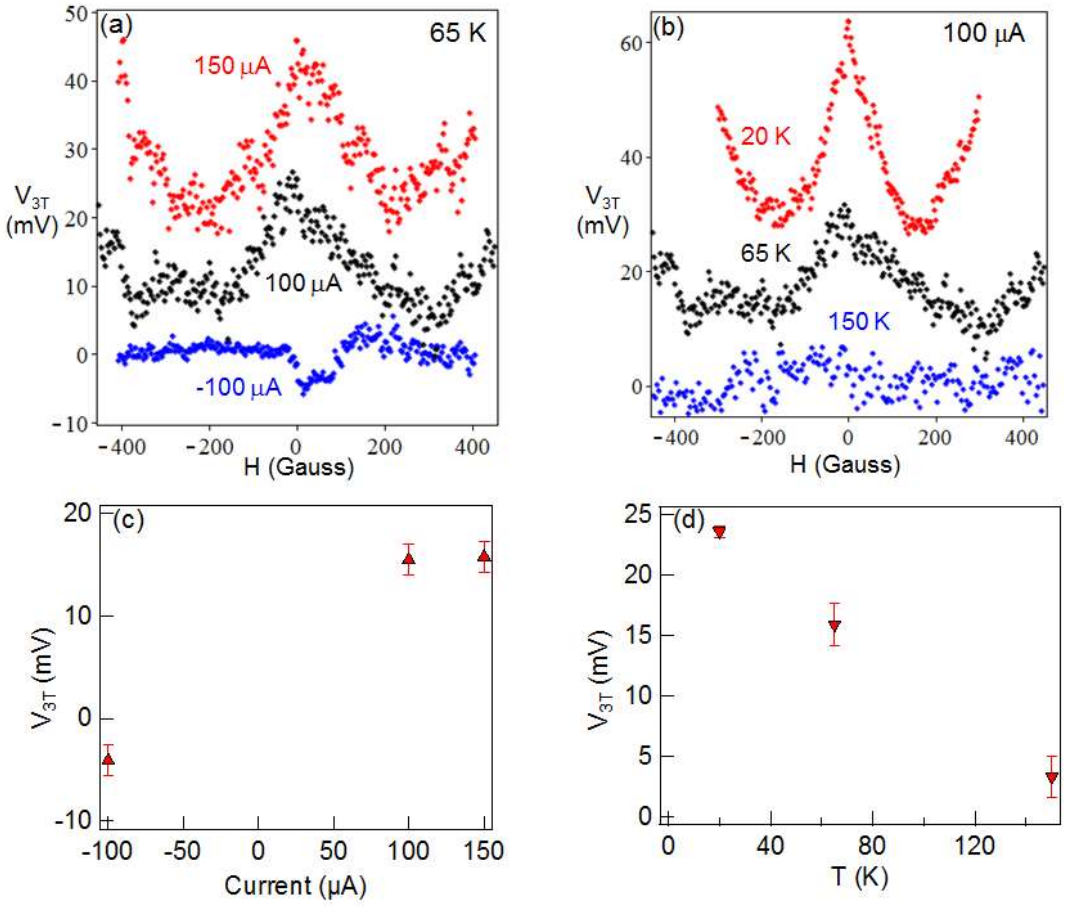

Fig. 5.17. Detected voltage versus applied out-of-plane magnetic field as a function of (a) applied current at 65 K and (b) temperature with an applied current of 100 μA using E1-8(structure 2). Corrected for a quadratic background voltage signal dependent on the applied magnetic field. The plots in (a) are offset by 10 mV (black), and 30 mV (red), to increase the clarity. The plots in (b) are offset by 15 mV (black) and 40 mV (red). The peak amplitudes in (a) and (b) have been plotted with respect to (c) applied current and (d) temperature. Error bars are calculated from the Lorentzian fit to the Hanle peak.

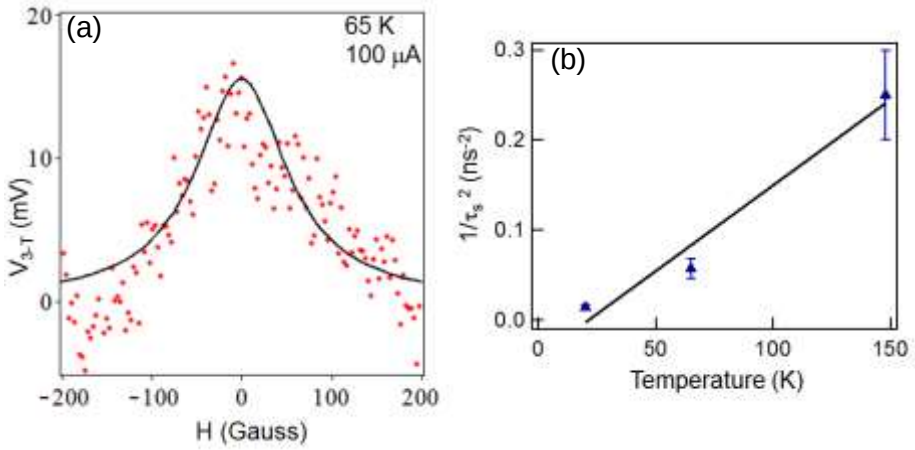

Fig. 5.18. (a) Plot of the detected voltage (diamonds) versus applied field for an applied current of 100 μA at 65 K with a Lorentzian simulation using equation 5.15 (black solid line). (b) Plot of $(1/\tau_s)^2$ with respect to temperature using sample E1-8(structure 2). The solid line is a least squared fit (slope = 0.0018 ± 0.0005 ns^{-2}K^{-1}). Error bars are from the range of τ_s obtained from fits.

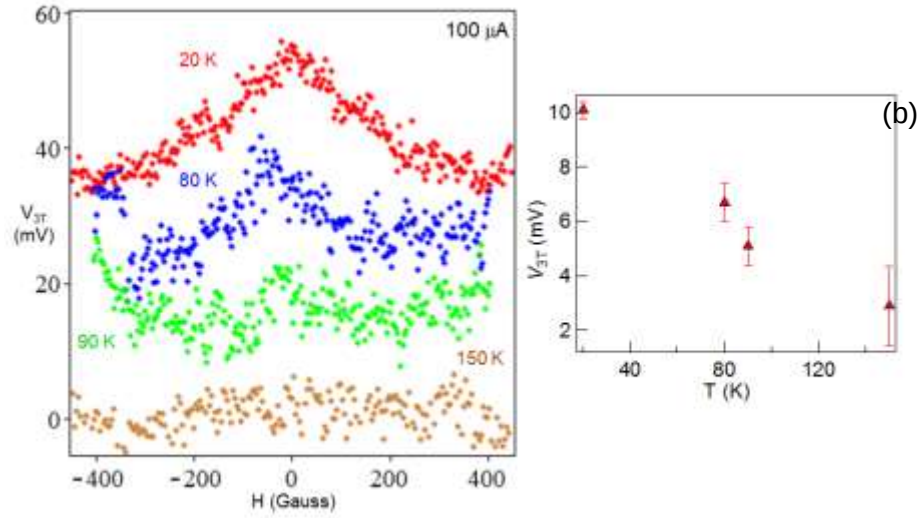

Fig. 5.19. (a) Plots of voltage versus temperature obtained using the 3-T Hanle configuration (Fig.5. (b)) with an additional in-plane magnetic field applied along the length of Fe contacts; and (b) plot of the voltage peak amplitude (from Lorentzian fit to the data) in (a) versus temperature using sample E1-8(structure 2). Plots are offset by 15 mV, 30 mV and 45 mV for 90 K, 80 K and 20 K respectively, with 150 K at the base.

Non-local (4-T) Hanle plots obtained at temperatures ranging from 25 K to 77 K are shown in Fig. 5.20 (a) using sample E1-8(structure 1). The data shows a peak in each Hanle curve at zero field, that decays for positive and negative *H*. The solid lines are simulation to each curve using equation 5.14 that assumed diffusive transport with zero drift velocity. The τ_s found from these fits ranged from 7.8 ± 0.4 ns to 3.2 ± 0.4 ns, 25 K to 77K. Errors are from the range of τ_s obtained in fits. These are consistent with the value obtained from 3-T Hanle fits (8.5 ± 0.4 ns to 1.8 ± 0.4 ns, 20 K to 148 K). $1/(\tau_s)^2$ has been plotted in Fig. 5.20 (b) as a function of temperature and compared with results from the literature for MBE Fe/GaAs(001) [48]. The slopes are similar (0.0015 ± 0.0005 $ns^{-2}K^{-1}$) and closer to the value obtained from 3-T Hanle measurements (0.0018 ± 0.0005 $ns^{-2}K^{-1}$) consistent with a spin-orbit scattering mechanism (Elliot-Yafet) [107] but the intercept is higher (τ_s is smaller) in our case. The spin diffusion lengths (using τ_s from 4-T Hanle measurements and equation 5.9) are varying from 7 μm to 4 μm for the temperature range of 25 K to 77 K.

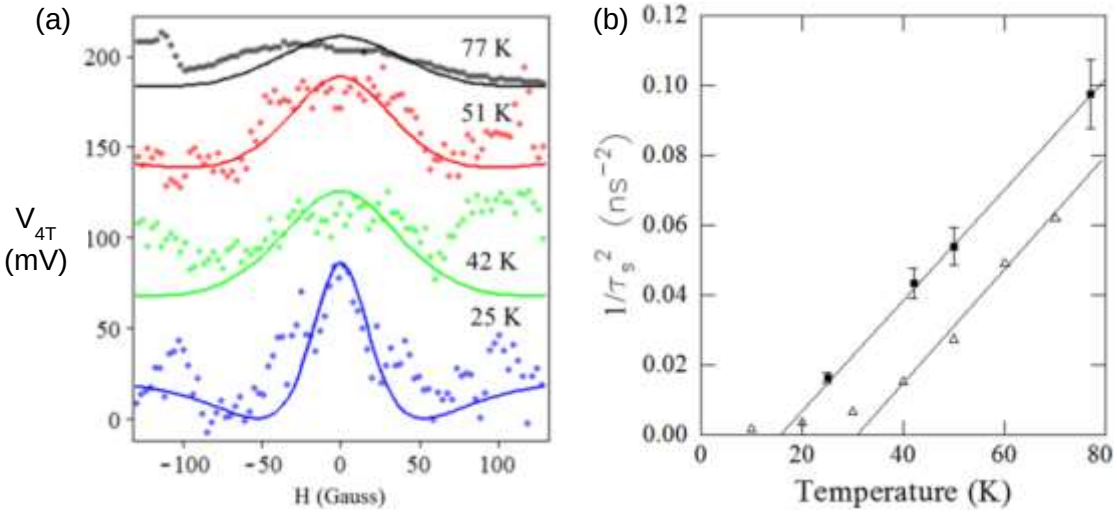

Fig. 5.20. Results from (a) Nonlocal 4-T Hanle measurements, applying an out-of-plane magnetic field, H, as a function of temperature using sample E1-8(structure 1). Solid lines are the simulations using the diffusion equation 5.14. Vertical offsets of 60 mV (in steps) have been added to the plots for clarity. (b) Plot of $1/(\tau_s)^2$ extracted from the best guess fits to the data in (a) versus temperature for ED (squares) and MBE (from literature [48]) (triangles) Fe/GaAs (001) spin contacts.

5.2.2.2. Higher doped sample (Fe on sample E2) (5×10^{18} /cm^{-3})

5.2.2.2.1. Hanle Measurements

Sample E2-2 has been used for these Hanle measurements. Fig. 5.21 shows plots of voltage versus applied out-of-plane magnetic field using the 3-T Hanle configuration (Fig. 5.9 (b)) for a Fe/GaAs (5×10^{18} doped) sample as a function of (a) current ranging from 30 μA to 150 μA at 40 K and (b) temperature ranging from 10 K to 100 K with an applied current of 100 μA. The voltage peaks occur at zero field for all temperatures. Fig. 5.21 (c) is a plot of the voltage peak amplitude as a function of applied current and (d) temperature. All the data are offset in steps by 55 mV for clarity. Also a quadratic voltage correction similar to other Hanle and spin valve data has been performed on these Hanle plots. The behavior of the peak voltages extracted from these Hanle measurements with applied current and the temperature showed similar changes as those of lower doped sample, although the voltages are three orders of magnitude smaller for the higher doped sample than for the lower doped sample.

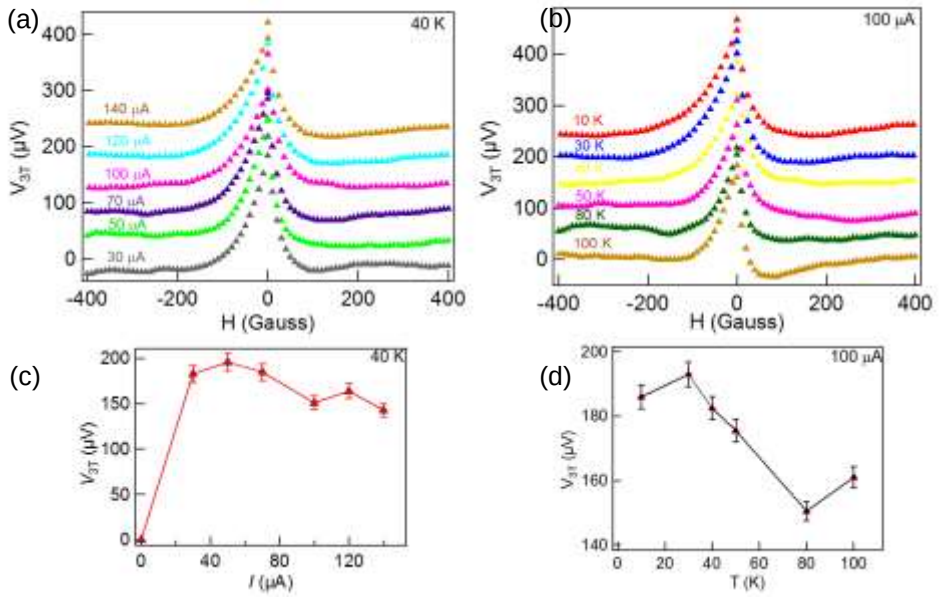

Fig. 5.21. 3-T Results from Hanle measurements showing plots of voltage versus applied out-of-plane magnetic field for Fe/GaAs (5×10^{18}/cm^3) as a function of (a) applied current at 40 K and (b) temperature with an applied current of 100 μA using sample E2-2. Plots are offset in 55 μV steps for clarity. The amplitude of the voltage peaks in (a) and (b) are plotted in (c) versus current and in (d) versus temperature.

5.2.3. Summary of results from spin transport measurements

4-T NLSV measurements at RT showed no sign of a spin voltage peak, as expected. The spin diffusion length in the GaAs channel at RT is less than 1 μm [108], which is much shorter than the distance between the injector and detector contacts (~ 4 μm). Thus, a spin voltage should not be detectable at room temperature since any spin accumulation would have dissipated at the detector contact. Note that the magnitude of the noise signal at RT was micro-volts much smaller than was observed at the lower temperatures. However, it is unusual to note that the net spin voltage obtained in our NLSV measurements (4-T) for $2\times10^{18}/cm^3$ ED Fe/GaAs samples (0.8 mV to 4 mV, 100 μA and -100 μA at 77 K) for positive applied current was much larger than for the reported MBE sample grown in UHV (16 μV at 50K) [11], despite a 10 times reduction in applied current in our case. If this voltage was due to spin diffusion then it should be observed in both sweep directions but not always with equal magnitudes [109]. For negative applied current the detected voltage was negative, as expected. For negative current, electrons flow from the GaAs into the Fe and at a Schottky barrier a specific type of spin-polarized electrons diffuse through the interface. Due to this fact minority (reverse polarity electrons with respect to positive current) spin electrons will diffuse to the detector through the GaAs channel producing the reverse voltage signal observed.

The magnitude of the NLSV voltage peaks increased with decreasing temperature, the expected behavior if these are due to spin transport. Also, noise in our spin voltage signals was higher at lower temperatures, consistent with inhomogeneous magnetic properties – correlated with the multi-domain structure within the Fe films due to the presence of impurities [66, 110-112]. The spontaneous formation of an interfacial magnetic oxide between Fe and GaAs is also highly likely to have contributed magnetic noise from domain switching processes. We attribute the complex switching behavior of our NLSV signals with changing magnetic field (Fig. 5.14 (b)), to the successive switching of multiple magnetic domains in each iron electrode, supported by the MOKE data. This exists possibly in combination with the switching of multiple magnetic domains in the proposed interfacial magnetic iron oxide tunnel barriers that within the model (to be discussed in the next section) are also responsible for the very large size of our spin voltage signals relative to those observed in systems with non-magnetic barriers.

Nonlocal 4-T Hanle measurements showed evidence of spin precession, relaxation and diffusion in the semiconductor channel as expected. The spin lifetime, τ_s is directly related to the width of the peaks. From the theoretical fits (Fig. 5.20b) using equation 5.14 to our Hanle plots, the spin lifetimes, τ_s, varied from 7.8 ± 0.4 ns to 3.2 ± 0.4 ns, at temperatures from 25 K to 77K. These values are comparable to the values reported for ultrathin MBE grown Fe/GaAs contacts from 24 ns to 4 ns, at temperatures from 10K to 70 K [11].

The spin diffusion time equation 5.14 normally contains only one averaged spin diffusion time (considering ideal abrupt Schottky interfaces) while there is likely more than one component contributing to the broadening of the peak. For example, spin flip scattering due to impurities has been shown to lower τ_s in permalloy/Ag wires [21]. Modification to spin precession rates and therefore, Hanle peak broadening correlated with smaller spin life times, has also been attributed to local magnetostatic fields originating from the finite roughness of FM film surfaces and at the interface [33, 35]. Our Fe films have a surface roughness of 20 nm which likely contribute to the reductions in τ_s.

The significant effect of local magnetostatic fields was shown via NLSV measurements while sweeping in-plane magnetic field oriented along the width of the bars. Voltage peak amplitudes comparable to peaks from conventional NLSV measurements were observed. The effect of local magnetic fields due to magnetic impurities at the interface was also indicated via the 3-T Hanle measurements with an additional in-plane magnetic field. Voltage peaks were obtained as usual at zero magnetic field, presumably due to spin accumulation in the GaAs, but the Hanle plots were broadened when an additional in-plane magnetic field was applied. This indicated an additional spin precession due to a component of the extra magnetic field, resultant of out-of-plane and in-plane acting along with the local magnetostatic field effects from the magnetic impurities. Also, the peak amplitude was reduced compared to its counterpart without an additional in-plane magnetic field. We can explain this by the in-plane magnetic field coupling with the local magnetic field modifying the orientation of diffused electron spin polarization at the interface [33, 106]. Surprisingly, these magnetic

impurities enhanced the tunneling probability of the spin accumulation at these ED Fe/epi-GaAs contacts but reduced the spin life time.

3-T Hanle measurements provide information regarding accumulation of spin polarized electrons diffused at the interface from the ferromagnetic metal in the semiconductor channel underneath a contact (either injector or detector). The spin life time found from the theoretical fit to the Lorentzian line shape (equation 5.15) of the 3-T Hanle varied from 8.5 ± 0.4 ns to 1.8 ± 0.4 ns, for the temperature ranges from 20 K to 150K for the $2\times10^{18}/cm^3$ doped Fe/GaAs sample. These values are consistent with the values obtained from the 4-T Hanle measurements, 7.8 ± 0.2 ns to 3.2 ± 0.2 ns, 25 K to 77 K similar to the results of others [113].

3-T Hanle peak amplitudes for lower and higher doped samples (2×10^{18} and 5×10^{18} $/cm^{-3}$) decreased by a factor of 7 and a factor of 1.5 from Fig. 5.17 (d) and Fig. 5.21 (d), respectively in the temperature range from 20 K to 150 K. Theoretically, the Hanle voltage, V_{3T}, depends on the $\rho\lambda_D$ product of the semiconductor channel (see equation 5.20). The expected $\rho\lambda_D$ product can be calculated from literature values of λ_D and measured ρ for our GaAs channel doping concentration. Combined with the applied current, this has been plotted in Fig. 5.22 as a theoretical *RA* product. From this plot it is found that *RA* and $\rho\lambda_D$ varied with temperature by a factor of 6 in the range of temperature from 20 K to 100 K. V_{3T} also depends on the tunneling probability of the interface which is not included in the equation 5.20 [100]. The tunneling probability, P, varies with temperature as $(1-\alpha T^{3/2})$, where, α is Bloch's constant that depends on the ferromagnetic material [100, 114]. Assuming an α value of 3.5×10^{-5} $K^{-3/2}$ for Fe film, the combined temperature dependence of V_{3T} increases to a factor of 7 which is in good agreement with the experimental findings for the lower doped sample [115].

The amplitude of the Hanle peak for spin accumulation (positive current) increases slowly up to 40 μA and then saturates and again slowly decreases with increasing applied current for the higher doped sample ($5\times10^{18}/cm^3$), as found by many other researchers [31, 35, 100]. This behavior is not fully understood at this moment. Ideally, the spin accumulation at the injector increases with applied current, increasing as the tunneling of spin polarized electron is enhanced with increased bias (Reversed bias in *J-V*). The Hanle signal was reversed for negative current, like the results from

spin valve measurement (electron flowing from GaAs to Fe) also very similar to the result found by other groups for FM/oxide/SM contacts [30-35, 100].

5.2.4. Comparison between spin transport theory and experiment

The spin resistance area product *spin-RA* was calculated from the experimental data using the magnitude of the voltage peak at zero field, V_{3T} from 3-T Hanle measurements.

$$(RA)_{expt} = \frac{(\Delta V_{3T})A_{contact}}{I_{applied}}. \quad (5.22)$$

Fig. 5.22 shows plots of the experimental values of *spin-RA* overlaid with a calculation of the theoretical *spin-RA* from equation 5.20, described in the section 5.2, as a function of measurement temperature for higher (circles, 5×10^{18}/cm^3) and lower (triangles, 2×10^{18}/cm^3) doped samples. The calculated RA product relies on experimentally measured values for λ_D (limited to only a few temperatures in this range), ρ of the channel (better known), and assuming the value of γ 0.3 [48, 108].

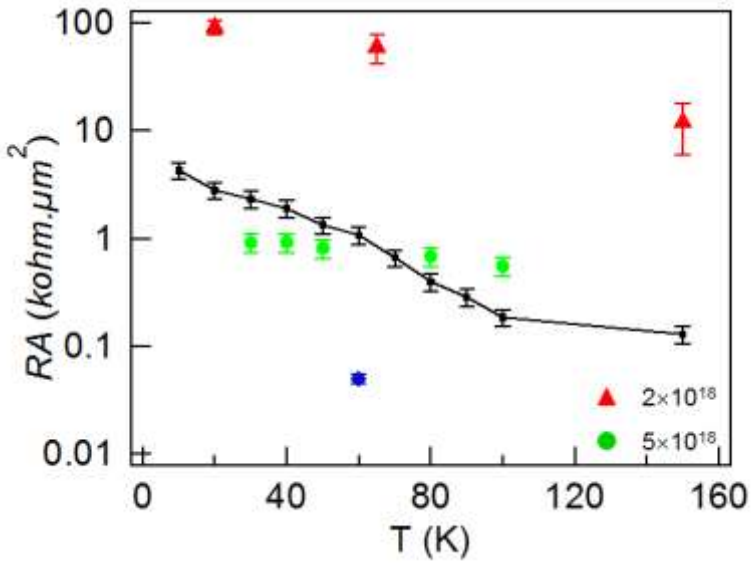

Fig. 5.22. Plots of *spin-RA* versus *T* for two doped samples (2×10^{18} and 5×10^{18} /cm^3). The solid line is based on spin diffusion theory (Equation 5.20). A literature value (blue circle) is from [113].

The *RA* product for the lower-doped sample is 20 times larger than the expected theory, whereas for the higher-doped sample it is comparable to the theoretical value but 10 times larger than the experimental value of their MBE counterpart (blue circle data point from the literature [113]). This follows the trend in the interface resistances for these samples.

Table 5.1 below shows the deviation in the *spin-RA* product extracted from 3-T Hanle measurements by other groups from the expected theoretical value.

Table 5.1. *Spin-RA* products observed by other groups with different oxide layers in FM/SM contacts

T K	FM	SC	Oxide	RA_{expt} $k\Omega.\mu m^2$	RA_{theory} $k\Omega.\mu m^2$	References
300	Co	GaAs	Al_2O_3	1000	1	Tran et. al. PRL 102, 036601 (2009)
10	Fe	Si	SiO_2	6	0.01	Jonker et. al. Nat. Comm. 1256, 1 (2011)
300	Ni-Fe	Si	Al_2O_3	6	0.01	Jensen et. al. PRB 84, 054410 (2011)
300	Co-Fe	Si	MgO	5	0.01	Jeon et. al. APL 98, 262102 (2011)
10	Co-Ni-Fe	Ge	Al_2O_3	1500	10	Jain et. al. APL 99, 162102 (2011)

These authors have speculated that these discrepancies may be the result of spin accumulation via two step tunneling at interfacial states and or to non-uniform tunnel junctions [30-35]. We have not ruled these models out. We will propose an additional mechanism below.

Table 5.2 shows a summary of the NLSV measurements listing the spin voltage, tunnel contact doping level, and experimental and theoretical *spin-RA* products. RA_{theory} is calculated using equation 5.13 and it varies with temperature as the resistivity and spin diffusion length changes with temperature. The *spin-RA* product from experiment for the lower-doped sample at lower temperatures (30 K and 40 K) are comparable to the theoretical values to within experimental error, however, the signal to noise of this data were poor. The better signal to noise of the 77 K data shows *RA* product two times less compared to the corresponding theoretical value and 400 times higher than the literature value for MBE grown Fe/GaAs contacts [11]. In the calculations carried out to estimate the theoretical values of *spin-RA* shown in Table 5.2, 100% spin polarization of the electrons injected into the GaAs was assumed. That the large theoretical values of *spin-RA* obtained in this way are comparable with my experimental *spin-RA* values suggests that the electrons injected into the GaAs in my experiment may be indeed highly spin polarized. This occurs perhaps due to an interface that is more abrupt in the Fe composition or that there is an additional interfacial spin tunnel barrier such as a magnetic oxide that adds a magnetic barrier. This is consistent with the fact that the experimental *spin-RA* values for MBE grown samples where an oxide interface was unlikely (Ref. 11, also shown in Table 5.2) are 3 orders of magnitude smaller than mine, although the maximal theoretical values of *spin-RA* estimated in the same way for the MBE grown samples are similar. However, other explanations should also be considered: 1) The actual area involved in the spin detection is much smaller than what is assumed for the calculation (*A*, area of the contact). 2) The assumptions of the drift diffusion theory that the band separation between spin up and spin down in the semiconductor channel is much smaller than the Fermi level energy is too simplified.

Table 5.2. Summary of the results from 4-T NLSV measurements (** from Ref. 11).

T K	Spin Voltage mV	GaAs Doping $\times 10^{18}$ cm^{-3}	RA_{expt} $k\Omega.\mu m^2$	RA_{theory} $k\Omega.\mu m^2$
77	0.8 ± 0.1	2	3.2 ± 0.4	7
40	10 ± 3	2	40 ± 12	23
30	17 ± 9	2	60 ± 30	28
50**	0.0168 ± 0.0002	5	0.0084 ± 0.0001	15

We propose that the larger spin voltages and contact resistances that we observe for our ED contacts are possibly due to an iron oxide interfacial layer that is magnetic and therefore has tunnel barrier heights that are different for majority and minority spin electrons. The thickness of this layer would likely increase for higher resistive, lower semiconductor tunnel doping concentrations [92-94]. For this reason, we hypothesize that ED contacts on lightly-doped GaAs tunnel junctions are more efficient spin filters than are ED contacts on heavily-doped GaAs. This is consistent with our experimental observation of larger Hanle voltages with ED contacts on more lightly-doped GaAs (23 mV for $2\times10^{18}/cm^3$) compared to the heavier-doped GaAs (190 μV for $5\times10^{18}/cm^3$). In the next section, quantum transport calculations by Dr. George Kirczenow are used to show that the spin filtering in contacts with spin-dependent tunnel barrier heights can be much more efficient (evident from much stronger spin voltage signals) than contacts with spin independent barrier heights; examples of the latter being abrupt Schottky barriers [11] or the non-magnetic MgO barriers [28]. The model is only a qualitative analysis to show possibilities.

5.2.5. Theoretical modelling for an enhanced spin signal

Quantum spin transport calculations were carried out on small, 4-terminal model structures (dimensions of several hundred Angstroms) with magnetic tunnel barriers (i.e., spin-dependent barrier heights) or non-magnetic tunnel barriers such as conventional Schottky (only) tunnel barriers of semiconductor-metal interfaces by Dr. George Kirczenow. The spin structures were modeled by a tight-binding Hamiltonian of the form:

$$H = \sum_{i\sigma} \varepsilon_{i\sigma} a_{i\sigma}^{+} a_{i\sigma} - \sum_{<i,j>\sigma} t_{ij} (a_{i\sigma}^{+} a_{j\sigma} + h.c.) , \qquad (6.2)$$

where $a_{i\sigma}^{+}$ is the creation operator for an electron with spin σ at site *i*. Spin-dependent tunnel barriers and spin scattering due to impurities are included in the model through the spin-dependent site energies, $\varepsilon_{i\sigma}$. Nearest neighbour electron hopping is described by the second summation on the right. A total of ~25000 lattice sites were included in the transport calculations. The inset in Fig. 5.23 shows the schematic of a device structure used for the modelling. It consists of two ferromagnetic electrodes 2 and 3 (dark blue) placed on the semiconductor (orange) with magnetic or Schottky (only) tunnel barriers (red). In the ferromagnetic contacts the majority spin carriers were assumed to have twice the density of states of the minority spin carriers at the Fermi level as in Lou's thesis [48]. For magnetic tunnel barriers the barrier height for minority carriers was chosen arbitrarily to be 3 times that for majority carriers. Another trial with 2 times was also performed, revealing similar results. Whereas for Schottky (only) the majority and minority spin barrier heights were assumed to be equal. Two non-magnetic electrodes 1 and 4 (pale blue) with non-magnetic tunnel barriers (pink) are included in the model. Phase breaking of the electronic quantum states and spin relaxation were included in the model by attaching 450 single-channel Büttiker leads [116] at random sites in the semiconductor. The inclusion of Büttiker leads allows the model to be used for diffusive transport. In order to evaluate the spin-transport coefficients of this model system in the linear response regime, the Lippmann-Schwinger (LS) equation is used to calculate the scattering amplitudes. This yielded the quantum transmission probabilities, $T^{\sigma}_{\alpha\beta}$ for electrons at the Fermi energy with spin σ between electrodes α and β (Fig. 5.23). This calculation was carried out for parallel and antiparallel magnetizations of electrodes

2 and 4. The Büttiker equations [117] for this system were solved numerically for the output resistance (non-local 4-terminal resistance of the system $R_{\uparrow\uparrow}$ or $R_{\uparrow\downarrow}$) using the scattering amplitudes obtained from the LS equation.

The results obtained for magnetic and Schottky (only) tunnel barriers, between ferromagnetic contacts 2 and 3 and the semiconductors are shown in Fig. 5.23 (a) and (b) respectively, as a function of the electron Fermi energy in the semiconductor. To make the resemblance with the experimental fact of spin diffusion length between injector and detector electrodes, the Büttiker leads were applied in such way that they coupled to the semiconductor between contacts 2 and 3 causing quantum phase breaking but not relaxation of the electron spin polarization, whereas, elsewhere, both phase breaking and spin relaxing were simulated. The calculated spin resistance $|R_{\uparrow\downarrow} - R_{\uparrow\uparrow}|$ (a measure of the spin voltage signal) is larger by a factor of approximately 20 – 50 for the case of magnetic tunnel barriers (Fig. 5.23 (a)) than for the case of Schottky tunnel barriers (Fig. 5.23 (b)) where the difference between $R_{\uparrow\uparrow}$ and $R_{\uparrow\downarrow}$ is solely due to the difference between the minority and majority spin densities of states at the Fermi level in the ferromagnets. While the details of the nonlocal resistance plots shown in Fig. 5.23 are sensitive to the microscopic details of the model, it is found that the difference in $R_{\downarrow}$ and $R_{\uparrow}$ are *consistently* much larger for magnetic tunnel barriers than for a Schottky (only) barriers. In principle, to account for the enhancement of the spin voltages reported in this thesis we conclude that more effective spin filtering occurs from magnetic tunnel barriers than conventional Schottky barriers. From this outcome we can infer that the difference in majority and minority energy bands in the semiconductor channel can be comparable to the Fermi level energy which may accommodate the enhanced accumulation in the semiconductor channel.

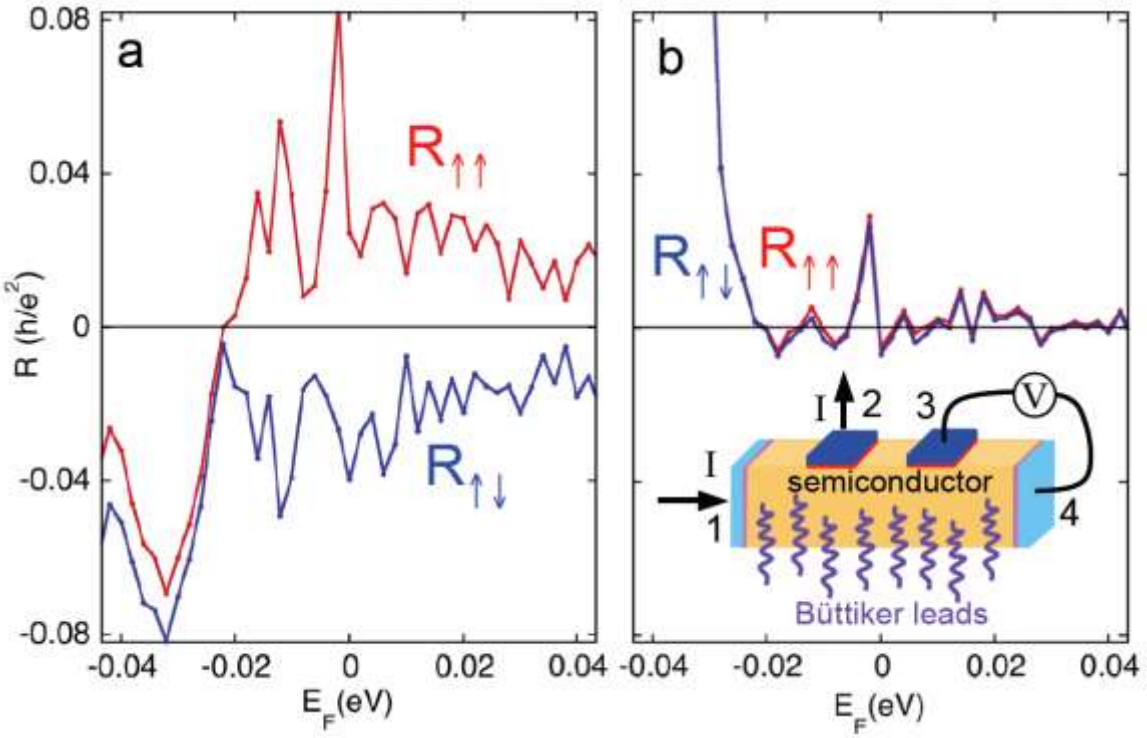

Fig. 5.23. Calculated non-local resistances $R_{\uparrow\uparrow}$ and $R_{\uparrow\downarrow}$ for parallel and antiparallel magnetization of the ferromagnetic contacts 2 and 3 (dark blue), respectively, vs. the semiconductor Fermi energy, E_F, for the model structure shown in the inset. Contacts 1 and 2 are the current leads while 3 and 4 are the voltage leads. Contacts 1 and 2 (pale blue) and the associated tunnel barriers (pink) are non-magnetic. The Büttiker leads (purple) carry no net current but break the phase of the electron wave functions throughout the semiconductor. They also induce electron spin relaxation except in the region of the semiconductor between contacts 2 and 3. In (a) the tunnel barriers (red) between the ferromagnetic contacts 2 and 3 and the semiconductor are magnetic, while in (b) They are non-magnetic.

6. Conclusion

In summary, we have demonstrated lateral spin injection and detection through electrodeposited Fe/GaAs interfaces experimentally. There is a large enhancement in the spin voltage signal compared to similar interfaces fabricated using UHV MBE methods. We have proposed that these higher spin signals may be related to a thin oxide layer that forms during electrodeposition or during contact fabrication, functioning as a magnetic tunnel barrier whose height differs for majority and minority spin electrons. We support these experimental results with quantum spin transport calculations that show a strong positive influence of a spin dependent magnetic tunnel barrier on spin transport efficiency for Fe/magnetic oxide/GaAs contacts.

Three major accomplishments were described in this thesis: first, the deposition of quasi single-crystalline Fe on an epi-GaAs sample; second, an understanding of the complex magnetization of ED Fe films (minor loops that lie outside the major loop); and third, the enhanced spin accumulation in the GaAs channel through these ED Fe/GaAs interface possibly due to a magnetic barrier at the interface.

The rate of nucleation and growth of ED Fe films on GaAs depends on the initial over-potential of the sample. The over potential varies along the semiconductor channel in proportion to the distance away from the ohmic contacts located at the perimeter. This prevented uniform growth of Fe over the epi-GaAs sample. We have successfully shown that the gradient in over-potential could be partially reduced by creating a uniform electrostatic field at the back of the sample; improving the coverage of the Fe film on epi-GaAs sample. Another important factor for the ED growth was the quality of the crystal structure of the film which was achieved by optimizing the applied current density. Our transport results can be better understood if there occurs a magnetic oxide barrier growth in between Fe and GaAs during ED process. In general, ED thin films of Fe on epi-GaAs sample are composed of quasi single-crystalline, mosaic nano-regions under

tensile strain and grain boundaries arising from the coalescence of separately nucleated epitaxial regions confirmed via high resolution XRD and TEM measurements.

The observation of magnetic hysteresis with minor loops extending outside the major loop is one of the interesting features of the ED films. The major hysteresis loops do not conform to models where uniform rotation plus domain wall motion occurs. A uniaxial anisotropy that was observed to prefer the [100] axes, does not explain the results unless it is added inhomogenously into the model. For (110) crystal structure, an inhomogeneous distribution of uniaxial anisotropy generates patterns of magnetization in which the directions of magnetization pass through the in-plane [111] magnetic hard axis when the field is applied along the intermediate in-plane [110] axis. This suppresses the large hysteresis that would accompany models in which there is uniform rotation of the magnetization through the [111] direction because of the confinement of the magnetization to the plane of the thin films. The results have been fit to analytic models and micromagnetic simulations [66]. We speculate that the multi-domain, magnetic structure and inhomogeneous magnetization that has been found in these ED films, arises from the boundaries that develop from island coalescence and magnetic impurities in the Fe. The structural and magnetic properties of Fe electrodeposited directly into patterned contacts were comparable to films electrodeposited on bulk GaAs sample.

We demonstrated that ED Fe contacts on epi-GaAs sample can be used for electrical lateral spin injection and detection. Results from Hanle and NLSV measurements give spin diffusion times (4 to 8 ns) that are a factor 2 lower than those of thinner MBE-grown Fe contacts [11], but with an enhancement in the spin voltage signal (0.8 mV versus 16 μV). Interestingly, it was found that the Hanle voltage signal increases with increased interfacial resistance (23 mV and 190 μV for 101 Ωcm^2 and 0.9 Ωcm^2, respectively). MOKE imaging supported our contention that magnetic switching of individual Fe contacts occurs at different field strengths during forward and reverse field sweeps, necessary for spin valve measurements.

We proposed that the larger spin voltages and contact resistances observed for our ED contacts may be due to an iron oxide interfacial layer that is magnetic and therefore has tunnel barrier heights that are different for majority and minority spin

electrons. The thickness of this layer increases for lower semiconductor doping concentrations [92-94] so the lightly-doped ED contacts on GaAs tunnel junctions are expected to be more efficient spin filters than on heavily-doped GaAs. Consistent with this, we experimentally observed larger Hanle voltages with ED contacts on more lightly-doped GaAs (23 mV for $2\times10^{18}/cm^3$) compared to those on more heavily-doped GaAs (190 μV for $5\times10^{18}/cm^3$). Quantum transport calculations support our experimental results that spin filtering in contacts with spin-dependent tunnel barrier heights can be much more efficient, as evidenced by much stronger spin voltage signals than in contacts where the barrier height does not depend on the spin. Examples of the latter are abrupt Schottky barriers [11] or the non-magnetic MgO or Al_2O_3 barriers [28].

The spontaneous formation of these interfacial magnetic oxides between Fe and GaAs at these ED interfaces contributed to magnetic noise presumably from domain switching processes at lower temperature in spin valve signals. We also observed at all temperatures, a complex switching behavior possibly due to successive switching of multiple magnetic domains in each iron electrode, likely in combination with the switching of multiple magnetic domains in the magnetic iron oxide tunnel barriers. This phenomenon was also evident in the MOKE imaging data.

The effect of magnetic in-homogeneities, due to likely magnetic oxide impurities at the interface and in the Fe film, was revealed via Hanle measurements which showed the presence of additional strong magnetostatic fields. We concluded that these fields influence the spin transport processes at the interface and are also responsible for the reduction in spin lifetime [32].

7. Future work

It is clear that higher growth temperatures produced better quality Fe films. The grain size, and epitaxy improves. All Fe spin contacts tested so far were produced from RT growth and it would therefore, be interesting to compare with higher growth temperature contacts. This thesis concentrated on (001) oriented GaAs and there is also great interest in comparing to (110) substrates to better understand the influence of the semiconductor orientation on spin injection. Modification to the interface preparation such as passivation with sulfur could be interesting. Variation in the spin structure dimensions such as the separation of the injector and detector contacts is also clearly a useful question for future investigations. Another important criterion to support spin transport is to test the experimental setup with nonmagnetic contacts so that it is clearer that whatever signal occurs from Fe/GaAs is due to spin only. If we believe that there is a finite magnetic oxide at electrodeposited Fe/GAas interfaces, then controlling its thickness would help to prove this correlation and its effects. The optimal thickness of this layer may be different for the different types of samples. Clearly, further spin valve and Hanle measurements with a wider range of parameters including bias, magnetic fields, temperature, are needed. All the data in this thesis for spin valve and Hanle measurements were obtained with a single sweep and often the signal to noise ratio was small. To improve the signal to noise ratio one can opt for multiple sweeps. We suspect that the origin of the noise at low temperature is Barkhausen noise which can be confirmed via SQUID hysteresis data at cryogenic temperature.

References

1. I. Žutić, J. Fabian and S. Das Sarma, *Rev. Mod. Phys.* **76,** 323 (2004).
2. S. Datta, S. and B. Das, *Appl. Phys. Lett.* **56**, 665 (1990).
3. H. J. Zhu, M. Ramsteiner, H. Kostial, M. Wassermeier, H. P. Schönherr, and K. H. Ploog, *Phys. Rev. Lett.* **87**, 016601 (2001).
4. A. T. Hanbicki, B. T. Jonker, G. Itskos, G. Kioseoglou, and A. Petrou, *Appl. Phys. Lett.* **80**, 1240 (2002).
5. A. T. Hanbicki, O. M. J. van't Erve, G. Kioseoglou, C. H. Li, B. T. Jonker, G. Itskos, R. Mallory, M.Yasar, and A. Petrou, *Appl. Phys. Lett*. **82**, 4092 (2003).
6. C. Adelmann, X. Lou, J. Strand, C. J. Palmstrøm, and P. A. Crowell, *Phys. Rev. B* **71**, 121301 (2005).
7. M. Johnson, & R. H. Silsbee, *Phys. Rev. Lett.* **55**, 1790 (1985).
8. M. Johnson, & R. H. Silsbee, *Phys. Rev. B* **37**, 5326 (1988).
9. F. J. Jedema, A. T. Filip, and B. J. vanWees, *Nature* **410**, 345 (2001).
10. O. M. van 't Erve, A. T. Hanbicki, M. Holub, C. H. Li, and C. Awo-Affouda, *Appl. Phys. Lett.* **91**, 212109 (2007).
11. X. Lou, C. Adelmann, A. S. Crooker, E. S. Garlidi, J. Zhang, K. S. Reddy, S. D. Flexner, C. J. Palmstrøm, and P. A. Crowell, *Nature Phys*. **3**, 197 (2007).
12. C. Awo-Affouda, O. M. J. van't Erve, G. Kioseoglou, A. T. Hanbicki, M. Holub, C. H. Li and B. T. Jonker, *Appl. Phys. Lett.* **94**, 102511 (2009).
13. T. Sasaki, T. Oikawa, M. Shiraishi, Y. Suzuki, and K. Noguchi, *Appl. Phys. Lett.* **98**, 012508 (2011).
14. T. Uemura, T. Akiho, M. Harada, K. Matsuda, and M. Yamamoto, *Appl. Phys. Lett.* **99**, 082108 (2011).
15. A. Fuhrer, S. F. Alvarado, G. Salis, and R. Allenspach, *Appl. Phys. Lett.* **98**, 202104 (2011).

16. Y. Zhou, W. Han, L. T. Chang, F. Xiu, M. Wang, M. Oehme, I. A. Fischer, J. Schulze, R. K. Kawakami, and K. L. Wang, *Phys. Rev. B* **84**, 125323 (2011).
17. M. Ciorga, A. Einwanger, U. Wurstbauer, D. Schuh, W. Wegscheider, and D. Weiss, *Phys. Rev. B* **79**, 165321 (2009).
18. G. Schmidt, D. Ferrand, L. W. Molenkamp, A. T. Filip, and B. J. vanWees, *Phys. Rev. B* **62**, R4790 (2000).
19. A. Fert, and H. Jaffre`s, *Phys. Rev. B* **64**, 184420 (2001).
20. A. Fert, J. M. George, H. Jaffrès, and R. Mattana, *IEEE. Trans. Elec. Dev.* **54**, 921 (2007).
21. G. Salis, A. Fuhrer, R. R. Schlittler, L. Gross, and S. F. Alvarado, *Phys. Rev. B* **81**, 205323 (2010).
22. B. D. Schultz, C. Adelmann, X. Y. Dong, S. McKernan, and C. J. Palmstrøm, *Appl. Phys. Lett.* **92**, 091914 (2008).
23. Zhi Liang Bao, PhD Thesis, Department of Physics, Simon Fraser University, Burnaby, 2006.
24. Z. L. Bao and K. L. Kavanagh, *J. Appl. Phys.* **98**, 066103 (2005).
25. B. D. Schultz, N. Marom, D. Naveh, X. Lou, C. Adelmann, J. Strand, P. A. Crowell, L. Kronik, and C. J. Palmstrøm, *Phys. Rev. B* **80**, 201309 (2009).
26. G. Salis, A. Fuhrer and S. F. Alvarado, *Phys. Rev. B* **80**, 115332 (2009).
27. M. K. Chan, Q. O. Hu, J. Zhang, T. Kondo, C. J. Palmstrøm, and P. A. Crowell, *Phys. Rev. B* **80**, 161206 (2009).
28. T. Akiho, T. Uemura M. Harada, K. Matsuda, and M. Yamamoto, *Jap. J. Appl. Phys.* **51**, 02BM01 (2012).
29. Sreenivasulu Vutukuri, PhD thesis, Dept. of Physics and Astronomy, University of Alabama, 2009.
30. S. P. Dash, S. Sharma, R. S. Patel, M. P. de Jong, and R. Jansen, *Nature* **462**, 491 (2009).
31. C. H. Li, O. M. J. van 't Erve , and B. T. Jonker, *Nature Comm.* **March**, 1 (2011).
32. M. Tran, H. Jaffrès, C. Deranlot, J. M. George, A. Fert, A. Miard, and A. Lemaître, *Phys. Rev. Lett.* **102**, 036601 (2009).
33. S. P. Dash, S. Sharma, J. C. Le Breton, J. Peiro, H. Jaffrès, J. M. George, A. Lemaître, and R. Jansen, *Phys. Rev. B* **84**, 054410 (2011).

34. K. R. Jeon, B. C. Min, J. Shin, C. Y. Park, H. S. Lee, Y. H. Jo and S. C. Shin, *New J. Phys.* **14**, 023014 (2012).
35. A. Jain, L. Louahadj, J. Peiro, J. C. Le Breton, C. Vergnaud, A. Barski, C. Beigne, L. Notin, A. Marty, V. Baltz, S. Auffret, E. Augendre, H. Jaffrès, J. M. George, and M. Jamet, *Appl. Phys. Lett.* **99**, 162102 (2011).
36. O. Eriksson, B. Johansson, R. C. Albers, and A. M. Boring, *Phys. Rev. B* **42**, 2707 (1990).
37. M. Gester, C. Daboo, R. J. Hicken, S. J. Gray, A. Ercole, and J. A. C Bland, *J. Appl. Phys.* **80**, 347 (1996).
38. G. Wastlbauer and J. A. C. Bland, *Adv. in Phys.* **54**, 137, (2005).
39. S. Majumder, B. Kardasz, G. Kirczenow, A. SpringThorpe, and K. L. Kavanagh, *Semicond. Sci. Technol.* **28**, 035003 (2013).
40. L. H. Jenkins, *J. Electrochem. Soc*. **117**, 630 (1970).
41. L. P. Bicelli, B. Bozzini, C. Mele, and L. D'Urzo, *Int. J. Electrochem. Sci.* **3**, 356 (2008).
42. C. Léger, J. Elezgaray, and F. Argoul, *Phys. Rev. E* **58,** 7700 (1998).
43. J. R. de Bruyn, *Phys. Rev. E* **56**, 3326 (1997).
44. Z. L. Bao, S. Majumder, A. A. Talin, A. S. Arrott, and K. L. Kavanagh, *J. Electrochem. Soc.* **155**, H841 (2008).
45. J. O'M. Bockris and A. K. N. Reddy, *Modern Electrochemistry* **1**, Chapter 4, Plenum, New York (1970).
46. A. SpringThorpe, National Research Council, 1200 Montreal Rd, Ottawa, ON K1A 0R6 Canada.
47. S. A. Crooker, M. Furis, X. Lou, C. Adelmann, D. L. Smith, C. J. Palmstrøm, and P. A. Crowell, *Science* **309**, 2191 (2005).
48. Xiaohua Lou, PhD. Thesis, University of Minnesota, 2007.
49. B. Tang, K. Sato, H. Tanaka and M. A. Gosalvez, *Proceedings of IEEE 2011 24th International Conference on Micro Electro Mechanical Systems,* 328, (2011).
50. M. Johnson, *IEEE Trans. Elect. Dev.* **54**, 1024 (2007).
51. B. E. Warren, *X-Ray Diffraction,* Dover Publications, New York, 253 (1968).
52. Rachel Goldman, PhD thesis, Department of Material Science, University of California, San Diego, 1995.

53. J. C. P. Chang, Jianhui Chen, J. M. Fernandez, H. H. Wieder, and K. L. Kavanagh, *Appl. Phys. Lett.* **60**, 1129 (1992).
54. C. R. Wie, H. M. Kim, and K. M. Lau, *Proc. SPIE* **877**, 41 (1988).
55. M. Winter, *http://www.webelements.com/iron/physics.html.* 2012.
56. A. W. Hull, *Phys. Rev.* **10**, 661 (1917).
57. T. Kebe, K. Zakeri, J. Lindner, M. Spasova, and M. Farle, *J. Phys Cond. Mat*. **18**, 8791 (2006).
58. B. Fultz, J. M. Howe, *Transmission Electron Microscopy and Diffractometry of Materials,* Springer, New York, 72 (2000).
59. D. B. Williams, and C. B. Carter, *Transmission Electron Microscopy,* Springer, New York, 444 (1996).
60. E. L. Hall, C. A. Germano, and H. M. Berg, *J. Electron. Mat.* **5**, 37 (1976).
61. E. B. Svedberg, J. J. Mallett, L. A. Bendersky, A. G. Roy, W. F. Egelhoff Jr., and T. P. Moffat, *J. Electrochem. Soc*. **153**, C807 (2006).
62. K. Thompson, D. Lawrence, D. J. Larson, J. D. Olson, T. F. Kelly, and B. Gorman, *Ultramicroscopy* **107**, 131 (2007).
63. S. Gadad and T. M. Harris, *J. Electrochem. Soc.* **145**, 3699 (1998).
64. Quantum Design, Operating manual for the MPMS, 1999.
65. J. Bland, PhD Thesis, Oliver Lodge Labs, Department of Physics, University of Liverpool, 2002.
66. S. Majumder, A. S. Arrott, and K. L. Kavanagh, *J. Appl. Phys.* **105**, 07D543 (2009).
67. S. Takahashi, L. Zhang and T. Ueda, *J. Phys. Cond. Mat.* **15**, 7997 (2003).
68. Y. B. Xu, E. T. M. Kernohan, M. Tselepi, J. A. C. Bland, and S. Holmes, *Appl. Phys. Lett.* **73**, 399 (1998).
69. M. Gester, C. Daboo, R. J. Hicken, S. J. Gray, A. Ercole, and J. A. C. Bland, *J. Appl. Phys*. **80**, 347 (1996).
70. B. Kardasz, E. A. Montoya, C. Eyrich, E. Girt, and B. Heinrich, *J. Appl. Phys.* **109**, 07D337 (2011).
71. B. Heinrich, J. A. C. Bland, *Ultrathin Magnetic Structures **II**,* Springer, New York, 196 (2005).
72. C. Kittel, *Phys. Rev.* **73**, 155 (1948).
73. G. Woltersdorf and B. Heinrich, *Phys. Rev. B* **69**, 184417 (2004).

74. H. Kronmüller, and S. Parkin, *The Handbook of Magnetism and Advanced Magnetic Materials* ***III,*** John Wiley & Sons, New Jercy, 1513 (2007).
75. B. Heinrich, and J. A. C. Bland, *Ultrathin Magnetic Structures* ***IV,*** Springer, New York, 101 (2005).
76. B. Heinrich, J. F. Cochran, and R. Hasegawa, *J. Appl. Phys.* **57**, 3690 (1985).
77. M. J. Hurben and C. E. Patton, *J. Appl. Phys.* **83**, 4344 (1998).
78. B. Heinrich, and J. A. C. Bland, *Ultrathin Magnetic Structures* ***III,*** Springer, New York, 144 (2005).
79. J. Tersoff, *Phys. Rev. B* **30**, 4874 (1984).
80. J. Tersoff, *Phys. Rev. Lett.* **52**, 465 (1984).
81. E. H. Rhoderick, *Metal-Semiconductor Contacts,* Oxford University Press, Oxford, 72 (1978).
82. E. I. Rashba, *Phys. Rev. B* **62**, R16267 (2000).
83. *http://www.nextnano.com/index.php* 2011.
84. A. Y. C. Yu, *Solid-State Electron.* **13**, 239 (1970).
85. B. T. Jonker, G. Kioseoglou, A. T. Hanbicki, C. H. Li and P. E. Thompson, *Nature Phys.* **3**, 542 (2007).
86. G. Kioseoglou, A. T. Hanbicki, R. Goswami, O. M. J. van 't Erve, C. H. Li, G. Spanos, P. E. Thompson and B. T. Jonker, *Appl. Phys. Lett.* **94**, 122106 (2009).
87. C. Adelmann, J. Q. Xie, and C. J. Palmstrøm, J. Strand, X. Lou, J. Wang, and P. A. Crowell, *J. Vac. Sci. Technol. B* **23**, 1747 (2005).
88. T. Saito, N. Tezuka, and S. Sugimoto, *IEEE Trans. Magnet.* **47**, 2447 (2011).
89. Q. O. Hu, E. S. Garlid, P. A. Crowell, and C. J. Palmstrøm, *Phys. Rev. B* **84**, 085306 (2011).
90. W. F. Brinkman, R. C. Dynes, and J. M. Rowell, *J. App. Phys.* **41**, 1915 (1970).
91. B. J. Jonsson-Akerman, R. Escudero, C. Leighton, S. Kim, I. K. Schuller, and D. A. Rabson, *Appl. Phys. Lett.* **77**, 1870 (2000).
92. I. Sakoi, M. Hirose, and Y. Osaka, *J. Electrochem. Soc.* **127**, 714 (1980).
93. M. V. Lebedev, D. Ensling, R. Hunger, T. Mayer, and W. Jaegermann, *App. Sur. Sci.* **229,** 226 (2004).
94. B. K. Tanner , D. A. Allwood , N. J. Mason, *Mat. Sci. Eng. B* **80**, 99 (2001).
95. A. Filipe and A. Schuhl, *J. Appl. Phys.* **81**, 4359 **(**1997).

96. F. P. Zhang, P. S. Xu, E. D. Lu, H. Z. Guo, F. Q. Xu, and X. Y. Zhang, *J. Appl. Phys.* **86**, 1621 (1999).
97. G. W. Anderson, M. C. Hanf, X. R. Qin, P. R. Norton, K. Myrtle, and B. Heinrich, *J. Appl. Phys.* **79**, 5641 (1996).
98. Y. Ji, A. Hoffmann, J. S. Jiang, J. E. Pearson and S. D. Bader, *J. Phys. D: Appl. Phys*. **40**, 1280 (2007).
99. A. Fert and S. F. Lee, *Phys. Rev. B* **53**, 6554 (1996).
100. R. Jansen, S. P. Dash, S. Sharma, and B. C. Min, *Semicond. Sci. Technol.* **27**, 083001 (2012).
101. Y. Aoki, M. Kameno, Y. Ando, E. Shikoh, Y. Suzuki, T. Shinjo, M. Shiraishi, T. Sasaki, T. Oikawa, and T. Suzuki, *Phys. Rev. B* **86**, 081201 (2012).
102. http://www.janis.com/Products/productsoverview/SuperVariTempReservoirCryostatSystems/SVT-200OpticalReservoirCryostat.aspx# 2012.
103. H. van Houten, C. W. J. Beenakker, M. E. l. Broekaart, M. G.H.J. Heijman, B. J. van Wees, H. E. Mooij, and J. P. Andre, *Acta. Electron.* **28**, 27 (1988).
104. Y. Zhou, W. Han, L. T. Chang, F. Xiu, M. Wang, M. Oehme, I. A. Fischer, J. Schulze, R. K. Kawakami, and K. L. Wang, *Phys. Rev. B* **84**, 125323 (2011).
105. T. H. Lee, H. C. Koo, H. J. Kim, J. Chang, S. H. Han, J. Hong, and S. H. Lim, *J. Mag. Mag. Mat.* **321**, 3795 (2009).
106. C. Awo-Affouda, O. M. J. van 't Erve, G. Kioseoglou, A. T. Hanbicki, M. Holub, *Appl. Phys. Lett.* **94**, 102511 (2009).
107. J. M. Kikkawa and D. D. Awschalom, *Phys. Rev. Lett.* **80**, 4313 (1998).
108. http://arxiv.org/ftp/arxiv/papers/1007/1007.0833.pdf 2013.
109. O. M. J. van 't Erve, C. Awo-Affouda, A. T. Hanbicki, C. H. Li, P. E. Thompson, and B. T. Jonker, *IEEE Trans. Electron Dev.* **56**, 2343 (2009).
110. C. W. J. Beenakker, and H. van Houten, *Solid State Phys.* **44**, 1 (1991).
111. D. Spasojević, S. Bukvić, S. Milošević, and H. E. Stanley, *Phys. Rev. E* **54**, 2531 (1996).
112. R.M. Bozorth, *Ferromagnetism,* IEEE Press, New York, Chapter 2 (1951).
113. Eric Scott Garlid, PhD. Thesis, University of Minnesota, 2010.
114. C. H. Shang, J. Nowak, R. Jansen, J. S. Moodera, *Phys. Rev. B* **58**, R2917 (1998).
115. Thomas Kebe, PhD. Thesis, der Universität Duisburg-Essen, 2006.
116. M. Büttiker, *Phys. Rev. B* **33**, 3020 (1986).

117. M. Büttiker, *Phys. Rev. Lett.* **57**, 1761 (1986).